



ALMA MATER STUDIORUM
UNIVERSITÀ DI BOLOGNA

DEPARTMENT OF INDUSTRIAL ENGINEERING - DIN

SECOND CYCLE MASTER'S DEGREE in
AEROSPACE ENGINEERING
Class LM-20

VTOL Directional Noise Reduction via Rotor Phase Synchronization: A Numerical Trim Procedure and Flight Mechanics Investigation

Graduation Thesis in Unmanned Systems

Supervisor

Prof. Emanuele Luigi de Angelis

Candidate

Diego Donnini

Co-Supervisor

Dr.-Ing. Thorsten Schwarz

Examiner

Prof. Jan Delfs

Graduation Session / March / 2025
Academic Year 2023/2024

In collaboration with:



DLR - German Aerospace Center

Institute of Aerodynamics and Flow Technology - Helicopter Department

Braunschweig, Germany 2024

Acknowledgements

I would like to express my gratitude to those who have guided me during this journey.

A special thanks to Dr. Thorsten Schwarz, who has been a true mentor during this research. From the very beginning, he believed in our project and gave us this incredible opportunity. His expertise, guidance, and constant availability have been priceless. He has been there every step of the way to offer support and insightful advice. What I have learnt from him has been essential for my academic and professional growth, and I am truly grateful.

I am also very grateful to Prof. Emanuele Luigi de Angelis, who has always been available to help with any issues or requests. His course inspired my passion for the subject, which has been a significant source of fuel for this project.

A warm thank you to the Helicopter Department at DLR for welcoming us as part of the team and always providing support. Their help and collaboration made this experience even more valuable.

A special mention goes to my friends and colleagues Aldo Chella and Francesco Sessini, who have been by my side during this adventure. We shared challenges, fatigue, and, of course, well-deserved German beers. Their friendship and support made this journey not only productive but also unforgettable.

Finally, my heartfelt thanks to everyone who, in one way or another, contributed to this work.

Abstract

This thesis presents a study on noise reduction strategies for multirotor vertical take-off and landing (VTOL) vehicles, conducted at the German Aerospace Center (DLR) in Braunschweig, under the Helicopter Department of the Institute of Aerodynamics and Flow Technology. The research specifically focuses on the implementation and evaluation of a numerical framework for analyzing rotor phase synchronization and its impact on noise directivity.

This study required the development and validation of a simulation toolchain for variable-pitch propellers and semi-rigid rotors with swashplate control, enabling detailed flight mechanics, aerodynamic, and aeroacoustic analyses. Using this toolchain, the study investigates rotor synchronization strategies and their effectiveness in reducing noise in different realistic operational scenarios. Significant achievements have been made, including the numerical demonstration of Sound Pressure Level (SPL) reductions of up to 10 dB in a ground target area 25 m below the aircraft. This represents an optimal result compared to the 70 dB baseline of an unsynchronized manned-sized hexa-rotor configuration.

This thesis specifically focuses on innovative tools for trimming multirotor configurations with synchronized rotors, relying on the coupling between a flight mechanic script and the Unsteady free-wake Panel Method (UPM) from DLR. This has proven to be a robust and reliable methodology for variable-pitch and semi-articulated rotors trim, unlocking new possibilities for multirotor VTOL flight mechanics and performance analysis.

In this research, a series of parametric studies are presented. The results highlight the potential of phase synchronization to improve noise directivity control in urban and military applications, achieving significant acoustic benefits with minimal hardware modifications and aerodynamic losses.

This work represents a significant step towards the development of quieter VTOL systems, addressing societal and regulatory demands for sustainable Urban Air Mobility (UAM).

Contents

Nomenclature and Conventions	VI
1 Introduction	1
1.1 Project Introduction	1
1.2 State of the Art	3
1.2.1 Variable Pitch Propeller	5
1.2.2 Double Articulated Rotors	6
1.2.3 Working Group and Workflow Description	7
1.2.4 Thesis Structure	9
2 Software / Hardware Tools Description	11
2.1 Introduction	11
2.2 UPM: Unsteady Panel Method	11
2.3 APSIM	14
2.4 Tecplot 360	14
2.5 MATLAB	15
2.6 Python	15
2.7 CARA: Computer for Advanced Research in Aerospace	16
3 Variable Pitch Propeller Multirotor Design Procedure	17
3.1 Introduction to Design Philosophy and Parametric Study	17
3.2 Blade Design	17
3.3 Design Requirements	19
3.4 HALO: HexAcopter for Low-noise Operations	20
3.5 Simplified Fuselage Drag Model	22
3.6 Simplified Inertia Model	23
3.7 Parametric Configurations	24
4 UPM Trim Script	25
4.1 Introduction	25
4.2 Reference Frames Description	26
4.3 Mathematical Trim Structure	27
4.4 Criteria of Success	28
4.5 Trade-offs in Script Design and Methodology	30
4.5.1 Operative Pitch Range Definition	30
4.5.2 Pseudo Steady State Condition	31
4.5.3 First Preliminary Script Implementation	33
4.5.4 Second Preliminary Script Implementation	33
4.5.5 Comparison and Final Script Implementation	35

4.6	3DoF Trim Results	38
4.6.1	Hover	40
4.6.2	Level Forward Flight	42
5	Phase Synchronization Effects on Flight Mechanics	47
5.1	Thrust Variation due to Phase Synchronization	47
5.1.1	Hover	47
5.1.2	Forward Flight	50
5.2	6DoF UPM Trim Script	53
5.2.1	Introduction	53
5.2.2	Test and Results Comparison with 3DoF	54
6	NOISE-Chain	59
6.1	Introduction	59
6.2	Hover Optimization	60
6.3	Results	62
7	Nonlinear Flight Dynamics Model	69
7.1	Introduction and Tuning	69
7.2	Power Analysis	70
7.3	Power Comparison	73
8	DUALO	75
8.1	Introduction and Sizing	75
8.2	Trim Script	77
8.3	Flight Mechanics Analysis	79
8.4	Aeroacoustic Parametric Study	81
8.4.1	Hover	81
8.4.2	Level Forward Flight	83
9	Conclusions	85
A	3DoF Trim Results	91
B	Phase Shift Effect on Trim Results	99
C	NOISE-Chain Results	105
D	DUALO Results	123

List of Figures

1	Azimuth convention description.	VIII
2	Phase convention description.	IX
1.1	Phase shifting concept.	4
1.2	Workflow scheme.	9
2.1	UPM lifting surface model.	12
3.1	Reference blade geometry KDE-CF125-DP.	18
3.2	Clockwise blade geometry visualization and mashing.	18
3.3	Volocopter 2X side view.	19
3.4	HALO front view.	20
3.5	HALO upper view.	21
3.6	Reference fuselage drag model for the cockpit.	22
3.7	Arms drag model.	22
3.8	Inertia model visualization.	23
4.1	Trim conventions.	26
4.2	Thrust vs θ_0 plot for a single rotor.	30
4.3	Wake development and aging in UPM time-steps.	31
4.4	Thrust and error behaviour as a function of the number of revolutions.	32
4.5	Second preliminary script simplified structure.	34
4.6	Different Trim implementation results and comparison.	35
4.7	4 rotors configuration visualization.	40
4.8	6 rotors configuration visualization.	40
4.9	8 rotors configuration visualization.	40
4.10	Simulation behaviour at low speed.	42
4.11	Simulation behaviour at high speed.	43
4.12	Trim results for different advancing speeds.	43
4.13	Inflow distribution.	44
4.14	Helicopter power estimation and different contributions.	45
5.1	Single rotor thrust distribution in the rotor disc.	47
5.2	Spatial thrust distribution in the 6 rotor case.	48
5.3	Thrust comparison for different configurations.	49
5.4	Thrust distribution comparison in forward flight condition.	51
5.5	Thrust history comparison in forward flight.	52
5.6	First hover trim comparison.	55
5.7	Second hover trim comparison.	55
5.8	Acoustic comparison for different trim procedure, $\chi = [0 -45 0 -45]$	56
5.9	Acoustic comparison for different trim procedure, $\chi = [0 90 0 90]$	56

6.1	NOISE-Chain simplified structure.	59
6.2	NOISE-Chain computational domain description.	61
6.3	Optimization scenarios.	62
6.4	Hemisphere optimization results.	62
6.5	Ground optimization results.	63
6.6	SPL [dB] distribution in the domain for the HALO configuration, Ground optimization.	65
6.7	Unsynchronized ground SPL [dB].	66
7.1	Thrust versus collective pitch (θ_0) comparison.	69
7.2	Required power versus forward speed for the HALO configuration.	72
7.3	Required power for fixed and variable pitch actuators.	73
8.1	DUALO geometry and sizing.	75
8.2	Trim results for different advancing speeds.	79
8.3	Acoustic footprint within the hemisphere and the ground, $\chi = [0,0]$	81
8.4	Acoustic footprint within the hemisphere and the ground, $\chi = [0,45]$	81
8.5	Acoustic footprint within the hemisphere and the ground, $\chi = [0,90]$	82
8.6	Level forward flight 150m above sea level, unsynchronized rotors.	83
8.7	Forward flight 150m above sea level, synchronized rotors, $\chi = [0,90]$	83
C.1	Unsynchronized noise emission for the 4 rotor configuration.	105
C.2	NR4 Hemisphere SPL [dB] at -45 deg elevation.	106
C.3	NR4 Ground SPL [dB] 25m below the configuration.	107
C.4	NR4 Hemisphere SPL [dB] at -45 deg elevation.	108
C.5	NR4 Ground SPL [dB] 25m below the configuration.	109
C.6	Unsynchronized noise emission for the HALO configuration.	110
C.7	NR6 Hemisphere SPL [dB] at -45 deg elevation.	111
C.8	NR6 Ground SPL [dB] 25m below the configuration.	112
C.9	NR6 Hemisphere SPL [dB] at -45 deg elevation.	113
C.10	NR6 Ground SPL [dB] 25m below the configuration.	114
C.11	Unsynchronized noise emission for the 8 rotor configuration.	115
C.12	NR8 Hemisphere SPL [dB] at -45 deg elevation.	116
C.13	NR8 Ground SPL [dB] 25m below the configuration.	117
C.14	NR8 Hemisphere SPL [dB] at -45 deg elevation.	118
C.15	NR8 Ground SPL [dB] 25m below the configuration.	119
C.16	NR8b Hemisphere SPL [dB] at -45 deg elevation.	121
C.17	NR8b Ground SPL [dB] 25m below the configuration.	122
D.1	Hover flight	126
D.2	Level forward flight at TAS = 18 m/s	127
D.3	Level forward flight at TAS = 28 m/s	128

List of Tables

3.1	Blade parameters.	18
3.2	Volocopter parameters.	19
3.3	Scaled blade parameters.	20
3.4	Rotors direction of rotation.	21
3.5	Inertia contribution data.	23
4.1	Volocopter criteria of success.	29
4.2	Hover condition.	38
4.3	Level Forward Flight condition, TAS = 28.33 <i>m/s</i>	38
5.1	Rotors thrust averaged in a single rotation.	49
5.2	Hover Condition 3DoF.	54
5.3	Hover Condition 6DoF.	54
6.1	SPL [dB] ground results.	66
C.1	NR4 phase (χ) optimization results.	105
C.2	NR6 phase (χ) optimization results.	110
C.3	NR8 phase (χ) optimization results.	115
C.4	NR8b phase (χ) optimization results.	120
C.5	NR8b rotors direction of rotation definition.	120

Nomenclature and Conventions

Acronyms

VTOL	Vertical Take-Off and Landing
UAM	Urban Air Mobility
UPM	Unsteady Panel Method
APSIM	Aeroacoustic Prediction System based on Integral Methods
DoF	Degrees of Freedom
SPL	Sound Pressure Level
BPF	Blade Passing Frequency
FW-H	Ffowcs-Williams/Hawkings
HALO	Hexacopter for Advanced Low-noise Operations
DUALO	DUAl rotor for Advanced Low-noise Operations
NOISE	Numerical Optimization of In-flight Sound Emissions
MTOW	Maximum Take-Off Weight
CCW	Counter-ClockWise sense of rotation
CW	ClockWise sense of rotation
NR2	2 rotors configuration
NR4	4 rotors configuration
NR6	6 rotors configuration
NR8	8 rotors configuration

Aerodynamics parameters

<i>ROTOR</i>	Rotor radius
<i>CHORD</i>	Blade aerodynamic mean chord
σ	Rotor solidity
<i>BLADES</i>	Number of blades
<i>Nrot</i>	Number of rotors within the configuration
<i>Re</i>	Reynolds number

Environmental parameters

ρ	Air density
<i>h</i>	Altitude
<i>dyn_viscosity</i>	Dynamic viscosity

Kinematics parameters

<i>TAS</i>	True Air Speed: intended as configuration velocity
<i>V</i>	Flow velocity
Ω	Rotor rotational speed
V_i	Rotor induced speed

Angles

θ_0	Collective pitch angle
θ_c	Cosine pitch first harmonic coefficient
θ_s	Sine pitch first harmonic coefficient
θ_{tw}	Blade linear twist pitch
β_0	Coning angle
β_c	Cosine flapping first harmonic coefficient
β_s	Sine flapping first harmonic coefficient
α	Flow incidence angle
Θ	Pitch attitude angle
Φ	Roll attitude angle
Ψ	Yaw attitude angle
ψ	Azimuthal coordinate \number of revolutions
ϕ	Azimuthal coordinate with respect the aeroacoustic FoR
χ	Phase shift vector

Aerodynamic coefficients

C_l	2D lift coefficient
$C_{l\alpha}$	2D polar lift slope coefficient
C_T	Thrust coefficient
C_D	Drag coefficient
μ	Advance ratio
λ	Inflow ratio
$\overline{C_d}$	Equivalent profile drag coefficient
$\overline{C_l}$	Equivalent profile lift coefficient
Cd_0	Parasite drag coefficient
Cf	friction coefficient

Subscripts

<i>hub</i>	hub frame of reference
<i>body</i>	body frame of reference
<i>UPM</i>	UPM motion frame of reference
<i>trim</i>	trim frame of reference
75	Percentage of the radius position

Azimuthal Angle Conventions

In regard to the definition of the azimuthal angle, two distinct definitions are presented, according to the context of usage.

- "**psi**" or (ψ) is the azimuthal angle with respect to the rotors hub.
This angle always has a value of zero in the y-direction (the direction of standard blade positioning without phase shift). Furthermore, it spans the entire circumference in the same direction as the rotational direction of the reference rotor. This angle is employed as a reference variable for rotor load plots, such as those depicted in Figures 5.3 and 5.2 due to its double nature.

This coordinate angle has also been employed for the description of the flapping and feathering motion (Chapter 8)

It should be noted that "**psi**" does not only represent the azimuthal spatial coordinate (Fig.5.2); it also reflects the time-varying rotor motion. In the latter case, "**psi**" is expressed as a decimal of the number of revolutions and it is independent from the rotor direction of rotation starting, like the former, always with zero in the y-direction (Fig.5.3).

In this latter case the coordinate is said to be fixed with the rotor hub frame of reference and so the subscript "*hub*" will be present.

- "**phi**" or (ϕ) is the azimuthal angle with respect to configuration centre.
It has value zero in the global x-direction (direction of motion in the forward flight case), and it spans the entire circumference always with a counterclockwise rotation. This angle has been used predominantly for the aeroacoustic simulation describing the azimuth of the reference hemisphere constructed all around the configuration. An illustrative example can be found in Figure 5.8.

An intuitive representation of the angles above mentioned is reported in Figure 1.

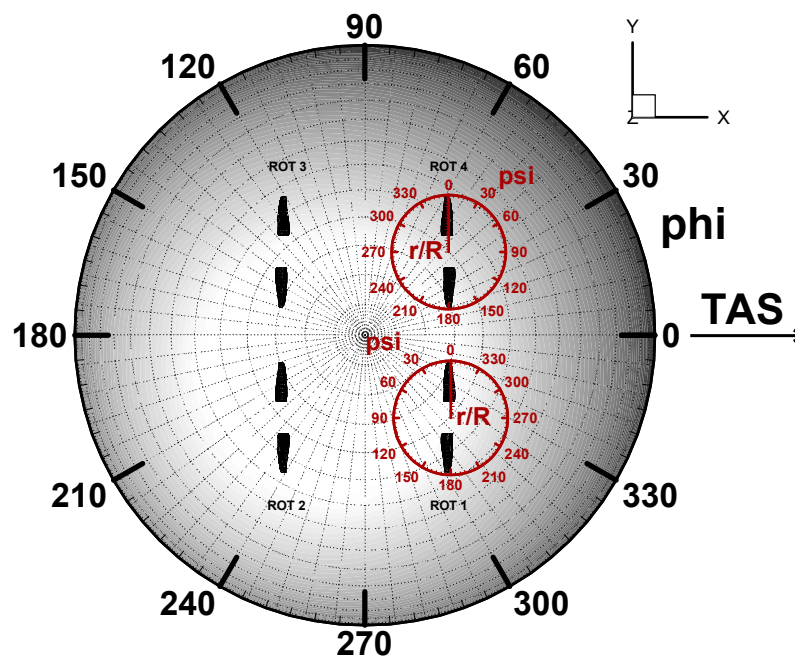


Figure 1: Azimuth convention description.

It should be noted that, as will be discussed subsequently, in Fig.1 the odd rotors are counterclockwise while the even ones are clockwise.

Phase Shift angle Convention

The phase shift between the rotors represents a crucial element of this study. Therefore, it is essential to provide a precise convention definition to prevent any potential ambiguities.

The **phase vector** or (χ) is the vector containing all rotors phases (χ_i) of the configuration. In order to reduce the number of potential combinations during the study, all the phases are written with respect the first rotor which is always at zero phase and it is used as a reference.

Zero phase means that the rotor is aligned with the y-axis like in Figure 1 above. Starting from this reference, a positive phase shift of the rotor i of an angle χ means that the blades are shifted of χ degrees in the direction of rotation of the i -th rotor. In the opposite way, a negative phase shift means that the blades are shifted of χ in the opposite of the direction of rotation of the i -th rotor.

The following figure (Fig.2) provides an intuitive description of the aforementioned definitions for the 4 rotors case.

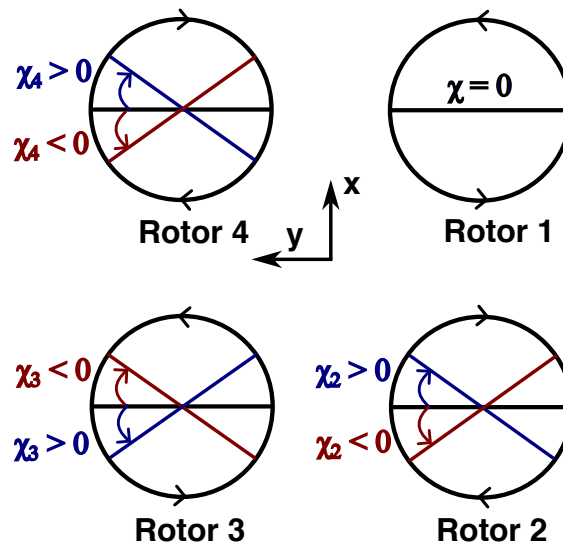


Figure 2: Phase convention description.

It should be noted that the decision to impose the first rotor with a zero phase angle is not a limiting factor. Should this be required, it is possible to achieve the desired rotor phase value by summing the latter to all the χ_i of the system.

Chapter 1

Introduction

The work presented in this thesis was conducted at the German Aerospace Center (DLR) in Braunschweig under the supervision of the Helicopter Department of the Institute of Aerodynamics and Flow Technology.

The primary objective of this project was to evaluate the capability of a numerical framework to assess noise-canceling strategies across various multicopter configurations. Specifically, the study focused on investigating the effect of phase shifts on noise directivity. To address this challenge, a research group comprising three master's students from the University of Bologna was created.

1.1 Project Introduction

Urban Air Mobility (UAM) represents one of the most significant and rapidly evolving areas of research in the aerospace industry. It is expected that advanced vertical take-off and landing (VTOL) vehicles will become a fundamental component of future transportation systems, offering solutions to congestion issues in urban environments and facilitating greater accessibility to remote areas. However, one of the most significant challenges in the design and deployment of these vehicles is the reduction of noise emissions [1, 2]. This is fundamental given that VTOL vehicles will operate in close proximity to populated areas, where public acceptance is a crucial factor in determining their feasibility and success.

Noise Reduction and Public Acceptance

A substantial number of studies, including research conducted by NASA [2], have identified noise as a significant impediment to the commercialization of UAM aircraft. The public's concerns regarding the disruptive effects of aircraft noise in densely populated urban settings have highlighted the necessity for quieter designs. Addressing these challenges is not only a matter of improving comfort but also a prerequisite for the successful integration of VTOL vehicles into urban environments. By prioritizing noise reduction during the design and development phases, the aerospace industry can ensure that VTOL technologies meet the expectations of urban transportation while respecting the needs of the community and the environment [3].

Noise Reduction in Military Applications

In addition to civilian applications, noise reduction is also a significant concern in the military domain. Recent conflicts have highlighted the growing reliance on sophisticated acoustic sensors for reconnaissance and targeting. In this context, the development of low-noise drone configurations for tactical operations has become a crucial research area [4, 5]. Reconnaissance and rescue missions, in particular, would greatly benefit from quieter designs, as these would minimize the risk of detection and enhance operational effectiveness [3].

Research Context and Objectives

The objective of this project is to address the aforementioned challenges by investigating an innovative noise-reduction strategy that has been specifically designed for multirotor VTOL configurations. At the core of this approach, a key solution is represented by rotor phase synchronization, a technique that has been demonstrated to achieve significant noise attenuation at specific target locations. The research aims to highlight the potential of this method to improve both public and military applications.

In recent times, researchers have investigated the potential of noise control techniques to mitigate the acoustic impact of VTOL vehicles. Among these, rotor blade phase synchronization has emerged as a promising technique. By adjusting the relative phase angles of the rotors, it is possible to induce destructive sound waves interference in targeted directions, effectively reducing noise in specific regions. This method has been successfully applied in distributed propulsion systems and offers the potential to minimize the acoustic impact of multirotor configurations without requiring significant modifications to rotor design and total weight [6].

A large amount of previous research have focused on fixed pitch propellers. However, in the case of eVTOLs, which are governed by variable RPM, the implementation of phase control becomes impractical. This study aims to address this issue by exploring noise cancellation techniques employing variable pitch propellers and articulated rotors.

The technical objective of this research is to develop a numerical simulation environment for the purpose of testing and optimizing the noise directivity through rotor phase shifting. Such a framework could be fundamental as a design tool for the future development of new advanced low-noise technologies.

As mentioned at the beginning of the chapter, the research was divided into three sub-projects, each assigned to a different team member. Aldo Chella [7] was responsible for developing an analytical model for noise prediction, while Francesco Sessini [8] focused on validating the numerical tool and conducting aerodynamic and aeroacoustic studies in forward flight. The present thesis focuses on the flight mechanics aspects of the project. Further details regarding the research subdivision are reported in Section 1.2.3.

1.2 State of the Art

The following section explores recent innovations in noise attenuation techniques for multirotor VTOL vehicles, with a specific focus on rotor synchronization strategies, starting from a general overview of the physics behind noise cancellation.

Main Rotor Noise Sources

In a classical helicopter, the noise generated by the rotor is the result of a variety of aerodynamic interactions between the rotor blades and the surrounding air. These interactions cause several kinds of noise sources and each of these has a distinct physical mechanisms associated with it.

Key noise sources identified in the literature [9] are:

- **Loading Noise:** Caused by fluctuating aerodynamic forces acting on rotor blades. These forces fluctuate due to the rotational motion of the blades and variations in air speed, and blade angle of attack. It is usually modelled as a dipole source.
- **Thickness Noise:** Results from the displacement of air due to blade volume. As the blade rotates, this displacement generates a characteristic sound pattern dependent on blade speed and geometry. This noise radiates spherically and is modelled as a monopole source.
- **Broadband Noise:** Generated by turbulence in rotor wakes and boundary layers. It spans a wide frequency range and is caused by stochastic aerodynamic interactions,
- **Blade Vortex Interaction (BVI) Noise:** Arises when rotor blades pass through vortices from preceding blades.
- **High-Speed Interaction (HSI) Noise:** It occurs when parts of the rotor blade, particularly the tips, approach or exceed the speed of sound. This compressibility effect leads to the formation of shock waves. At high rotational speeds, the airflow around the blade becomes transonic or supersonic. This generates strong, localized pressure gradients and high-frequency noise emissions that are highly directional.

An understanding of these sources and their underlying physical mechanisms is beneficial in the development of effective noise reduction strategies for rotorcraft.

In this project, the most significant sound sources subjected to analysis are the loading and thickness noises. Of particular interest in this research are the frequencies near the blade passing frequency (BPF), as these are the frequencies that are most affected by rotor synchronization noise cancelling.

Fundamental quantities

In order to provide a clear definition of the main acoustic quantities used in this thesis, a brief overview from Delfs [10] is presented.

The human ear perceives sound due to the physical stimulation caused by the air pressure variation, which is referred to as the *unsteady sound pressure*, or *acoustic pressure fluctuation*:

$$p'(t) = p(t) - \bar{p}, \quad \bar{p} = \lim_{T \rightarrow \infty} \frac{1}{T} \int_{-T/2}^{T/2} p(t) dt, \quad \overline{p'(t)} = 0 \quad (1.1)$$

in which \bar{p} is the steady part obtained by temporal averaging and is not perceived as sound. An appropriate measure of the strength of acoustic signals is the root mean square or *rms* value of sound pressure:

$$p'_{rms} = \sqrt{p'^2} \quad (1.2)$$

The range of detectable pressure fluctuations is extremely large, going from the order of 10^{-5} Pa (threshold of hearing) up to 10^2 Pa (threshold of pain). For this reason, a logarithmic scale is commonly used when dealing with acoustic quantities. The most important variable introduced is the *Sound pressure level* or *SPL*:

$$SPL = 10 \log \left(\frac{p_{rms}}{p_0} \right)^2 = 20 \log \left(\frac{p_{rms}}{p_0} \right) \quad (1.3)$$

in which p_0 is the reference pressure, generally taken as the hearing threshold $2 \cdot 10^{-5}$ Pa, and the pressure is squared to obtain a measure proportional to the energy of the wave.

Aeroacoustic Fundamentals and Noise Cancelling Principles

Noise cancellation in multirotor systems primarily exploits principles of destructive interference. If the rotors are modelled as acoustic sources, it is possible to achieve cancellation at specific frequencies by adjusting the relative phase angles of rotor blades in two or more different rotors (Fig. 1.1). This is particularly effective for the blade passage frequency (BPF) harmonics, which often dominates noise emissions in hovering configurations. Techniques such as phase synchronization manipulate these angles to reduce the net radiated sound power without requiring substantial changes to the rotors' physical design.

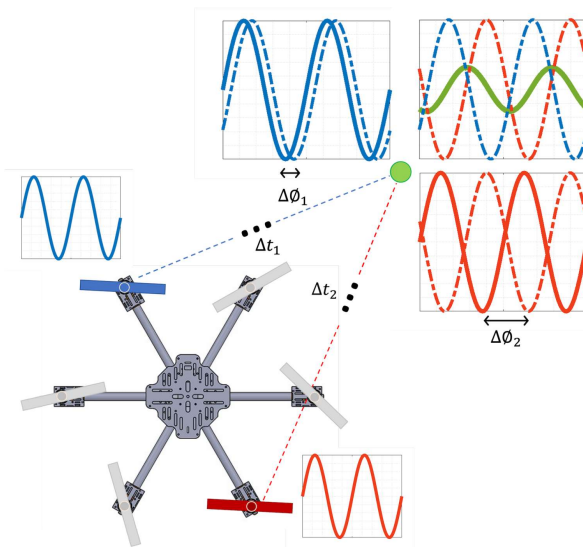


Figure 1.1: Phase shifting concept, from Valente [11]. The contribution of each rotor to the pressure fluctuation arrives at the target creating destructive sound wave interference.

The process of rotor synchronization is achieved through the matching of rotational speeds and the synchronization of azimuthal blade positions between paired rotors. This alignment results in the formation of regions of reduced sound intensity, making it an appro-

priate solution for applications in urban environments.

The study by Schiller et al. [6, 12] demonstrated that phase synchronization of paired rotors could achieve a reduction in the overall sound pressure levels at the blade passage frequency (BPF) of up to 5 dB, based on both experimental and numerical evaluations. Their work focused on both corotating and counterrotating rotor configurations, revealing that corotating pairs with a 90° phase offset provide an optimal overall noise attenuation. Furthermore, the study demonstrated that a greater noise reduction is possible in certain regions, thereby opening the way for the optimization of noise directivity.

Other researchers, such as Kukhwan Yu et al. [13], have investigated noise control in axial flight, demonstrating how active phase adjustments can mitigate rotor-rotor interactions. Guan's analysis of rotor-to-rotor interactions [14] further emphasized the critical role of phase synchronization in controlling the global acoustic radiation patterns, supporting the effectiveness of this strategy in forward flight condition.

Phase synchronization methods offer a significant advantage in that they can be readily adapted to existing rotor systems with minimal hardware modifications and no significant increase in weight or aerodynamic losses. For these reasons it is a valid solution for UAM and military applications.

1.2.1 Variable Pitch Propeller

In order to have synchronized rotors while ensuring full aircraft controllability, it is essential to adopt a non-classical actuation mechanism. One feasible solution is the use of variable pitch propellers.

These systems enable independent collective pitch control for each rotor, allowing thrust to be adjusted directly via blade angle modulation rather than relying uniquely on rotor speed (RPM) changes. This decoupling of RPM and thrust generation preserves the RPM channel for phase synchronization purposes, thereby unlocking new levels of flexibility and functionality in multirotor configurations.

The motivations behind the adoption of variable pitch propellers in this project are the following:

- **Advanced multirotor control:** While fixed-pitch systems are commonly used due to their mechanical simplicity, variable pitch systems offer superior performance. Variable pitch propellers provide rapid thrust adjustments, reduced control saturation, and the ability to reverse thrust efficiently. These features improve the overall control and manoeuvrability of the drone, making it more versatile and responsive in various scenarios [15].
- **Energy efficiency:** Variable pitch rotors are proven to be more power-efficient compared to fixed-pitch rotors under similar operating conditions. This efficiency translates into longer flight times and reduced operational costs, contributing to the overall sustainability and economic viability of such drone technology [16–18].
- **Adaptability to larger rotors:** As multirotors increase in size, traditional RPM control methods become less effective due to the higher inertia of larger motors. Variable pitch propellers are essential for stabilizing larger drones, as they provide the

necessary control to handle increased rotational inertia, ensuring reliable performance even with larger and heavier systems [19].

- **Simplification and performance:** Variable pitch rotors simplify the control mechanisms compared to traditional collective and cyclic controls. This reduction in complexity leads to enhanced performance and manoeuvrability, making the drones more effective for a wide range of applications, from urban mobility to specialized tasks [18, 19].

Of course, variable-pitch systems are more complex than fixed-pitch propellers, but fixed-pitch solutions are typically used in small drones that are not suitable for passenger transportation.

- **Autorotation for safe landing:** The ability of autorotation allows the drone to perform safe landings or at least reduce impact velocity in emergency situations. This safety feature is crucial for minimizing damage and ensuring reliable operation under various conditions [20].

Finally, the introduction of variable pitch propellers represents a consistent change in the field of propulsion design, moving away from the limitations of traditional fixed-pitch systems. Indeed, while fixed-pitch rotors are widely used due to their mechanical simplicity and ease of integration, they impose inherent limitations on responsiveness, energy efficiency, and scalability. Variable pitch mechanisms, by contrast, offer precise control, superior versatility, and the ability to optimize performance under a wide range of conditions. These advantages make variable pitch systems particularly well-suited to the requirements of advanced multirotor designs.

1.2.2 Double Articulated Rotors

An alternative method for maintaining aircraft control while ensuring synchronization of rotors is the use of articulated or semi-articulated rotors in combination with a swash-plate. This choice permits full controllability using both cyclic and collective, while simultaneously allowing the RPM channel to operate freely to maintain phase synchronization.

Despite the inherent difficulties associated with the implementation of this technology, the number of minimum rotors required for full controllability is reduced from four (for the classical variable pitch actuation) to two when this kind of actuation is employed.

This is significant because it reduces the complexity of noise distribution and optimization, as there are only two distinct sources.

As reported by Johnson et al. [21] a configuration with two side by side articulated rotors offer several key advantages, particularly in terms of lift capacity, and efficiency, making them suitable for heavy-lift operations, military missions, and UAM tasks. The counter-rotating rotor design eliminates the necessity for a tail rotor, thereby removing the corresponding high-frequency noise associated with it.

These features make dual rotor helicopters particularly well-suited for large payloads, in fact, nowadays, they are adopted in military transport (e.g. the CH-47 Chinook) and rescue operations.

1.2.3 Working Group and Workflow Description

The work presented in this thesis is based on a first conceptual phase carried out during the Rotorthon 2023 at the European Rotors in Madrid.

The Rotorthon 2023 challenge aimed to design an ultra-quiet VTOL aircraft capable of passenger transport while minimizing noise emissions to enhance public acceptance. Given the increasing concerns about rotorcraft noise in urban areas, the challenge required teams to propose innovative solutions that would significantly reduce noise compared to existing VTOLs. The approach developed during the competition led to the phase shift synchronization method, which later became the focus of the research conducted at DLR.

To address this challenge, a research group comprising the three master's students from the Rotorthon team was formed.

The research activities of the group were structured according to the following plan:

- Conducting an analytical review to gain a fundamental understanding of the problem.
- Setting up and validating a numerical simulation chain for fixed-pitch propellers.
- Developing a tool for trimming multirotor configurations with variable-pitch propellers.
- Analyzing noise emissions for different arrangements of variable-pitch propellers and varying operational conditions.
- Developing a simplified tool for trimming semi-rigid rotors equipped with a swashplate (as opposed to rigid propellers).
- Investigating noise control strategies for semi-rigid rotors.
- Developing an optimization chain for noise minimization and directivity control.

Aldo Chella [7] (block a in Fig. 1.2) focused on the physics of noise cancellation, developing an analytical model based on the rotating monopole theory to predict noise directivity and the effects of phase synchronization on noise reduction. His model was validated by comparing its predictions with NASA experimental data [6] on fixed-pitch propellers. He then conducted a parametric study to assess the impact of key factors such as rotor placement, phase angles, thrust variations, and blade number. His work provided a fundamental understanding of the physical mechanisms behind noise cancellation, forming the basis for the numerical and optimization studies carried out by the rest of the team.

Francesco Sessini [8] (block c in Fig. 1.2) was responsible for developing and refining the numerical tools needed to simulate noise cancellation effects in multirotor configurations. His first task was to set up and validate the UPM-APSIM simulation toolchain, ensuring it could accurately model the acoustic behaviour of phase-controlled rotors. To verify the reliability of the toolchain, he recomputed the NASA test cases [6], comparing results with existing experimental data. A crucial part of his research was investigating propeller-propeller aerodynamic interactions to determine if they significantly influenced total noise emissions. Francesco also conducted a parametric study on variable

pitch propellers in forward flight, evaluating how different rotor configurations and operational conditions affect noise levels.

This thesis (block b in Fig. 1.2) specifically focuses on the flight mechanics aspects of the project and is based on a number of working steps, which are described in the following:

1. Define a suitable multirotor configuration for the study, designed for people transportation.
2. Variable Pitch Propeller Analysis:
 - Develop and validate a simple flight mechanics (FM) tool for trimming a multirotor configuration with variable pitch propellers.
 - Set up a simulation chain with UPM (SubCh.2.2), where the results of the flight mechanics tool are used to prescribe the pitch of the variable pitch propeller. Add the acoustic post-processing with APSIM (SubCh.2.3).
 - Set up an automatic toolchain for the steps FM-UPM-APSIM, aiming to minimize user interactions.
 - Perform simulations for noise cancellation with variable pitch propellers to demonstrate that the simulation method can be applied for detailed parametric studies.
3. Semi-rigid Rotor Analysis:
 - Develop and validate a simple flight mechanics tool for computing the motion of semi-rigid rotors¹ and the complete configuration stability. This includes trimming collective and cyclic controls of the individual rotors to ensure the required total thrust and net-zero moments of the complete configuration, as well as computing the flapping motion of the rotor blades.
 - Set up an automatic toolchain for the FM-UPM-APSIM process to improve simulation efficiency.
 - Perform a parametric study on noise cancellation for articulated rotors in forward flight, evaluating different operational conditions.

The research workflow followed a structured approach, where each phase of the study was iteratively refined based on the findings of the different team members. The core process can be summarized as follows:

- **Analytical Modelling** Fig. 1.2a): The optimal rotor phase vector is computed for a target noise reduction zone based on theoretical noise directivity predictions.
- **Flight Mechanics** Fig. 1.2b): The computed phase settings are integrated into the trim procedure, ensuring that the configuration remains balanced.
- **Numerical Validation and Optimization** Fig. 1.2c): Once the trimmed configuration is established, detailed acoustic and aerodynamic analyses are performed to assess the effectiveness of the phase shift synchronization.

¹A semi-rigid rotor is a rotor in which only flapping and feathering motions are present. Flapping is enabled by a dedicated hinge, while lead-lag motion is constrained by the structural flexibility of the blades. Feathering motion is controlled via swashplate.

This step-by-step approach ensured that the noise reduction strategy was developed systematically, moving from theoretical feasibility to numerical implementation. However, the research was not a strictly linear process, as several iterations between team members were required to refine the methodology, overcome challenges and improve the overall effectiveness of the approach.

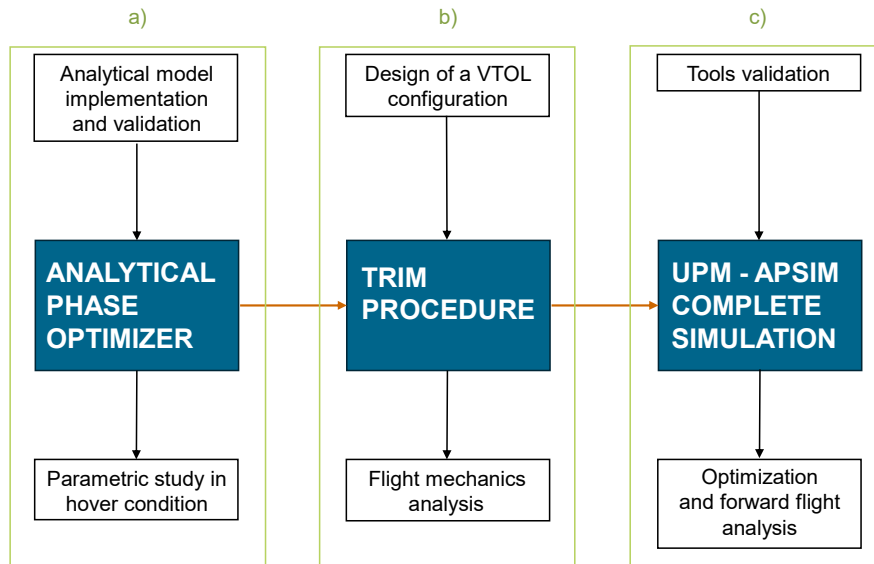


Figure 1.2: Workflow scheme.

1.2.4 Thesis Structure

The thesis is organized into several chapters. The structure is designed to guide the reader through the background, methodology, and key findings of the study.

The thesis begins with an **Introduction** where the project objectives are outlined. The second chapter focuses on the **Software and Hardware Tools Description**, detailing the computational tools and simulation environments used throughout the research, such as UPM and APSIM. Subsequently, the **Variable Pitch Propeller Multirotor Design Procedure** chapter describes the design philosophy and sizing. This includes blade design, aerodynamic models, and key design requirements. The fourth chapter is dedicated to the **UPM Trim Script**, where the mathematical structure of the trim algorithm is presented. The chapter covers the implementation details, methodology, and the results obtained from the trim analysis in both hover and forward flight conditions. Following this, the **Phase Synchronization Effects on Flight Mechanics** chapter investigates the impact of rotor phase synchronization on flight dynamics. It includes a detailed analysis of thrust variations and the comparison between different degrees of freedom in the trim models. The **NOISE-Chain** chapter presents the results of optimization studies conducted collaboratively with the team. The seventh chapter introduces a **Nonlinear Flight Dynamics Model** and a preliminary study of performance is presented. In the **DUALO** chapter instead, a preliminary study of a two semi-rigid rotors configuration is presented. This section evaluates the flight mechanics and aeroacoustic performance of the new design.

Finally, the thesis concludes with a summary of the main findings, contributions, and potential directions for future research in the **Conclusions** chapter.

Chapter 2

Software / Hardware Tools Description

2.1 Introduction

In the course of this thesis, several specialized software and hardware tools have been employed to perform simulations, data analysis, and visualization. The integration of these tools has enabled a structured workflow, ensuring the precision and efficiency required in the analysis.

This chapter provides a brief overview of the key software tools used. The description includes their main features, the specific role they played in the research, and the reasoning behind their selection.

2.2 UPM: Unsteady Panel Method

The *Unsteady Panel Method* (UPM) is a mid-fidelity simulation tool developed by the German Aerospace Center (DLR) for helicopter simulations, and is currently being modernized to support industrial helicopter development processes. UPM is designed to bridge the gap between low-fidelity and high-fidelity methods in the prediction of aerodynamic interactions, making it particularly valuable in identifying critical configurations like the presence of more than one single rotor as did in this research.

UPM has been validated against multiple test cases, including isolated rotors, wings, and complete helicopter configurations. A notable validation effort involved the GOAHEAD campaign, where experimental wind tunnel data was compared to UPM simulations, demonstrating good agreement between the two [22].

Nowadays it is frequently employed in conjunction with APSIM (SubCh.2.3) for the purpose of conducting aeroacoustic numerical simulations. Moreover, it has been subjected to experimental validation in the past, thus providing a degree of reliability for its utilization in this context.

The UPM code is a computational tool designed to simulate fluid flow around lifting and non-lifting bodies using a velocity-based potential flow formulation. The governing equation for the potential flow is the Laplace equation:

$$\nabla^2\Phi = 0 \quad (2.1)$$

where Φ represents the velocity potential. This equation is valid under the assumptions that the flow has to be **inviscid**, **incompressible**, and **irrotational**.

As a panel method, UPM employs the following boundary conditions to ensure the accurate simulation of the flow.

- **Neumann condition:** The velocity normal to the body surface is set to zero, ensuring impermeability:

$$\mathbf{v} \cdot \mathbf{n} = 0 \quad (2.2)$$

- **Kutta Condition:** At the trailing edge, UPM employs:
 - The *classical Kutta condition*, forces the flow to be tangential to the airfoil's camber line at the trailing edge, and is utilized in the simulation of finite wings.
 - An *unsteady pressure Kutta condition*, which constrains equal pressure on the upper and lower surfaces of the trailing edge panels, accounting for unsteady effects that are typical of rotorcraft simulations.
- **Far-Field Boundary:** At infinity, the flow velocity equals the free-stream velocity.

For unsteady simulations, UPM applies the unsteady Bernoulli equation to compute pressure coefficients.

In the case of lifting bodies, the surfaces are discretized using structured panel surfaces, consisting only of quadrilateral constant sink/source panels. To model lift generation, the source panels are superposed with a vortex lattice placed along the mean surface of the lifting bodies. At the trailing edge, a fullspan free wake vortex sheet consisting of constant strength vortex rings is emitted and transported through the flow-field in a force-free way, simulating the unsteady wake rollup (Figure 2.1).

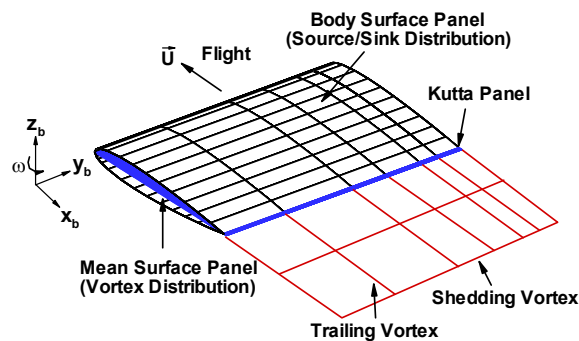


Figure 2.1: UPM lifting surface model [23].

UPM is an inherently unsteady method. At the first time step the simulation starts without wake panels. Then, each time step a new row of wake panels is shed from the Kutta panels of each lifting surface (e.g. rotor blade). Existing wake panels from previous time steps are convected with the flow. Therefore, a convergence assessment may be required to ensure that the initial roll-up of the starting vortex is sufficiently distant from the rotors.

Knowing that the wake panels evolve dynamically over time, their positions are updated

using explicit temporal integration schemes, like Adams-Bashforth Method or Predictor-Corrector Schemes. Consequently, the timestep size, which determines the selected integration method's operational precision, is a crucial parameter affecting the accuracy of the simulation.

To avoid singularities at the vortex core, UPM replaces the potential vortex with viscous models such as:

- **Rankine Core Model:** Used as the default to limit singularity strength.
- **Scully-Kaufmann Model:** Empirically adjusted for core growth under specific flow conditions.

The initial viscous vortex core radius (`r0_core`) is a crucial parameter that requires tuning during simulations. As a pure mathematical constraint in this type of code, it must be selected with precision to align with the desired physical behaviour. In contrast to conventional CFD codes, the dissipation of vorticity does not occur "naturally"; instead, an appropriate model must be selected.

For lifting surfaces (i.e. rotors, stabilizers, wings), stripwise boundary layer analysis using integral methods can be employed in order to calculate the chordwise and spanwise boundary layer properties. However, this option currently consists only of post-processing. The evaluation can be incorporated into UPM, enabling the command `ivisc`. This form of post-processing can be useful for providing an initial assessment of the flow state on the blade, accounting for the potential for stall correction and friction coefficient evaluation.

The input files required by UPM are `UPM.dat`, `motion.dat` and `geometry.dat`. The first file contains all the required simulation parameters, including the geometry file. The second file describes the motion of the object to be simulated using sums of motion nodes. The final file comprises the blade and/or fuselage structure, written in grid format. For lifting bodies, a special applicative called PANGEN [23] can be used to model the geometry and the sources/sinks distribution along the geometry itself.

In regard to the outputs, they are presented in Tecplot format, which facilitates more effective visualisation and comprehension. In this study, the most frequently utilized output files were the `thrust.tec` and `wake.tec`. The former records the total forces acting on the simulated body for each time step, whereas the latter provides a visual representation of the wake development. This was beneficial in assessing the qualitative aspects of the computational convergence. Finally, the `press_apsim-it-n.tec` represents the pressure fluctuation distribution in the blades and is formatted to be used as the standardized input for the APSIM computation.

Reference: See [23], [22] for more details.

2.3 APSIM

The *Aeroacoustic Prediction System based on Integral Methods* (APSIM) is a computational framework developed at the DLR Institute of Aerodynamics and Flow Technology for predicting rotor and propeller noise in the far-field.

It is based on the Ffowcs-Williams/Hawkings (FW-H) formulation, which is a well established method for modelling sound radiation from aerodynamic sources. APSIM assumes linear sound propagation and is particularly suited for simulating wave propagation over large distances in uniform flows.

This modular system is designed for flexibility and integration with existing aerodynamic solvers, enabling detailed numerical simulations of aeroacoustic phenomena. The framework supports noise prediction for various applications, with a primary focus on helicopter rotors and propellers.

APSIM is a sophisticated tool that has been developed for the purpose of advanced noise prediction. It is a valuable resource for the design of quieter and more efficient aerospace systems, and has been employed in the development of rotorcraft and propeller-driven aircraft with reduced environmental impact.

The efficacy of APSIM has been validated through a series of experimental tests [24].

In order for APSIM to work, it requires input data containing pressure data from CFD calculations. In this research, the input data are derived from the UPM computation. Additionally, the microphone array dispositions, which essentially delineate the domain in which the aeroacoustic results must be recorded, are another requisite input.

In this research project, APSIM has been utilized for all aeroacoustic computations due to its capacity to assess the thickness, loading, and quadrupole noise. The first two sound sources, in fact, are the ones primarily affected by the phase synchronization disruptive effect.

Reference: See [25],[24] for more details.

2.4 Tecplot 360

Tecplot 360 is an advanced software solution for computational fluid dynamics (CFD) visualization and analysis. It is widely recognized for its ability to handle complex multidimensional data, offering capabilities that allow the user to visualize and analyze simulation data in both two and three dimensions.

In this thesis, Tecplot 360 was employed for:

- **UPM Post-processing:** Tecplot 360 was used to visualize the results of the UPM fluid dynamics simulations output and of the APSIM aeroacoustic simulations. This included the creation of contour plots, 2D Cartesian plots, and 3D visualizations.
- **Data Integration:** Tecplot 360 facilitated the integration of simulation data from various sources and formats, enabling a coherent analysis process.

The selection of Tecplot 360 was motivated by its robust performance in handling large datasets and its compatibility with the output formats used in this research.

2.5 MATLAB

MATLAB is a high-level programming environment widely used for mathematical modelling, simulation, and data analysis. It provides an extensive range of toolboxes that support diverse engineering and scientific applications, making it an indispensable tool in research involving numerical computation.

For the purposes of this thesis, MATLAB was employed in the following tasks:

- **Mathematical Modelling and Simulation:** MATLAB was used to model and simulate the dynamics of the HALO configuration (Ch.7). The built-in functions for solving ordinary differential equations (ODEs) and the Simulink environment allowed for the accurate modelling of system behaviours.
- **Data Analysis and Visualization:** Numerical data from the Simulink Dynamic model and the Python trim script were processed and visualized using MATLAB.

The selection of MATLAB was predicated on its versatility and capacity for integration with other software, including Python.

The decision to utilise Simulink for the analytical tool was an evident one, given its inherent simplicity in dynamic modelling.

2.6 Python

Python is a general-purpose programming language that has become widely adopted in scientific computing due to its simplicity and the vast number of available libraries. Python's strengths lie in its flexibility and ability to integrate with other tools, making it ideal for data processing and automation tasks.

In this thesis, Python was primarily used for:

- **Automation and Scripting:** Python scripts were written to automate data processing tasks, particularly in conjunction with the UPM computations. This integration allowed for the processing of aerodynamic results within the trim script.
- **Data Analysis:** Python's libraries, including *NumPy* were utilized for handling large datasets. These libraries enabled the efficient manipulation of data and provided robust tools for numerical analysis and analytical computations.
- **Visualization:** The *Matplotlib* library was used for generating plots and visual representations of the data. This was particularly useful in creating fast visualizations of the script performances without the usage of more complex tools.

Python was selected due to its ease of use and its capacity to integrate effectively with other software utilized in this research.

The UPM trim script (Ch.4) and the NOISE-Chain (Ch.6), which constitute the primary components of this thesis, have been entirely developed in Python.

2.7 CARA: Computer for Advanced Research in Aerospace

The *CARA* (Computer for Advanced Research in Aerospace) high-performance computing cluster is an essential tool developed by the German Aerospace Center (DLR) to support large-scale numerical simulations. Installed at the Lehmann Data Centre at TU Dresden, *CARA* is equipped with 2,720 computing nodes powered by AMD EPYC processors and NVIDIA A100 GPUs, designed for handling highly complex simulations related to aerospace research. The system has a peak performance of 3.2 petaflops, enabling simulations in areas such as aerodynamic flows, turbulence, and structural optimization.

The cluster can simulate phenomena like wake vortices in aircraft, flow resistance in vehicles, and even environmental optimizations such as the optimal placement of wind turbines.

In this thesis, *CARA* was employed to run several mid-fidelity simulations that required great computational power. Despite the fact that UPM is considerably more rapid than other CFD programs, the nature of this research necessitated a substantial number of simulations that could have required several weeks to complete. So the usage of this cluster facilitated the assessment of a substantial number of test cases.

Reference: For more details, refer to [26].

Chapter 3

Variable Pitch Propeller Multirotor Design Procedure

3.1 Introduction to Design Philosophy and Parametric Study

In order to understand the physical processes underlying phase shift noise reduction, it is essential to conduct a parametric study. This will require the identification of a reference geometry, which will then be used as a starting point for other typologies of geometry that are simply modifications of the reference one.

In particular, the commonality between the geometries that will be studied in this work are the blade geometry, the rotor radius and the rotational speed, which are maintained in order to ensure that the rotor aerodynamics characteristics remain consistent throughout the study.

In the course of this research, variable pitch rotors will be employed in contrast to the conventional RPM-controlled rigid rotors. The rationale behind this decision is thoroughly outlined in SubCh. 1.2.1. However, the primary motivation is the necessity to maintain rotor synchronization and to control the system by adjusting the thrust of each rotor individually.

3.2 Blade Design

As previously stated, a variable pitch control method is required to maintain the stability of the system and the possibility of utilizing the active noise control method object of this study. To this end, a dedicated analysis of the optimal blade geometry should be conducted in order to ensure maximum efficiency in each flight configuration.

However, this kind of study is not within the scope of the project, so some assumptions have been made.

The blade geometry selected for the study is the KDE-CF125-DP Fig.3.1, with an appropriate scale factor that will be explained in SubCh. 3.3.

In Tab. 3.1 the parameter θ_{root} represents the nominal airfoil incidence angle at the blade root. In contrast, θ_{twist} defines the blade twist, which describes the variation in the blade's incidence angle from the root to the tip. Lastly, θ_0 refers to the collective angle of the rotor, evaluated as the incidence angle of the propeller at the root (hub of the rotor). ROTOR is the rotor radius length.

The same kind of geometry has been used by DLR, CIRA and ONERA in [27] for numerical and experimental data comparison.

It is important to note that this kind of propeller is also available on the market[28].



BLADE PARAMETERS	
θ_{root}	15 deg
θ_{twist}	6.25 deg
$CHORD_{75\%}$	0.024 m
ROTOR	$6.5 \cdot CHORD_{75\%}$
Root cut-out	$1.95 \cdot CHORD_{75\%}$

Figure 3.1: Reference blade geometry KDE-CF125-DP [6], [28].

Table 3.1: Blade parameters.

The motivation behind this decision can be attributed to the fact that NASA [6, 12] employed this specific geometry in its study, so it is possible to evaluate the goodness of the aerodynamic simulations through comparison with their own experimental results. This kind of analysis has been conducted by Sessini in [8] demonstrating an optimal agreement between the numerical simulations and the experimental data. This analysis was also essential for identifying the optimal simulation parameters that will be adopted and explained in detail throughout this dissertation.

Finally, the selection of this particular blade geometry is also justified by the fact that it is a common configuration for small- to medium-RPM controlled multirotors, making it an optimal starting point for this study.

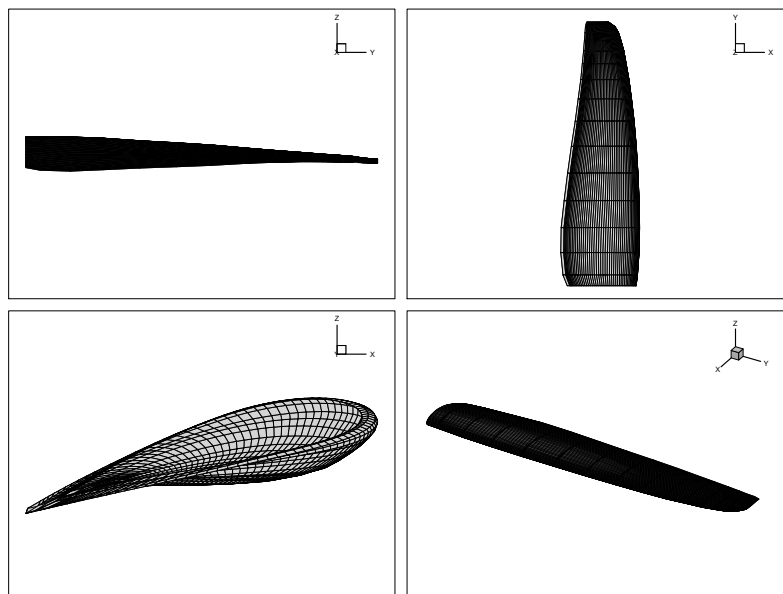


Figure 3.2: Clockwise blade geometry visualization and meshing.

3.3 Design Requirements

The preliminary stage of the sizing procedure consists to select a reference eVTOL, which serves as a starting point for subsequent calculations.

The Volocopter 2X (Fig.3.3) emerges as the optimal choice, given its successful flight test results and the inherent advantages of its simple design and low weight.



Figure 3.3: Volocopter 2X side view [29].

VOLOCOPTER 2X PARAMETERS	
MTOW	450 kg
Tip-to-tip distance	9.15 m
Fuselage length	3.15 m
Overall height	2.15 m
Cruise speed	102 km/h

Table 3.2: Volocopter parameters[30].

In order to achieve the desired thrust at the maximum take-off weight (MTOW), it has been determined that a six-propeller configuration is the optimal selection considering the potential parametric configurations. Once the number of rotors has been selected, an iterative procedure utilizing the principles of Blade Elements Momentum Theory eq. 3.1 from Leishman [31] has been employed:

$$\theta_0 = \frac{6C_{Treq}}{\sigma C_{l\alpha}} - \frac{3}{4}\theta_{twist} + \frac{3}{2}\sqrt{\frac{C_{Treq}}{2}} \quad (3.1)$$

$$C_{Treq} = \frac{MTOW}{N_{rot}} \cdot \frac{1}{\rho \cdot \pi ROTOR^2 \cdot (\Omega \cdot ROTOR)^2} \quad (3.2)$$

with:

- $C_{l\alpha} = 2\pi$: as a first assumption.
- $\Omega = 110rad/s$: fixed as reference velocity in order to have a comparable tip speed with respect to NASA case [6].
- $\sigma = \frac{BLADES \cdot ROTOR \cdot CHORD_{75}}{\pi \cdot ROTOR^2}$: rotor solidity, which contains the sizing parameters.

Using this iterative approach, it was possible to determine an appropriate scaling factor for the rotor radius (ROTOR) in order to meet the requirements while keeping θ_0 below a reasonable threshold of 20 degrees. The operative range of θ_0 will be discussed in more detail later in the study.

Following the radius scaling, the remaining geometrical parameters were determined, ensuring that the original blade proportions were preserved. The final scaled blade parameters are reported in tab. 3.3.

It is important to note that the root cut out distance is purely a geometrical assumption

needed for the numerical computation as reported in fig.3.2. The actual blade geometry will continue until it reaches the hub connection with the shaft, fig.3.1.

SCALED BLADE PARAMETERS	
$CHORD_{75\%}$	0.168 m
RADIUS	1.1 m
Root cut-out	0.3 m

Table 3.3: Scaled blade parameters.

3.4 HALO: HexAcopter for Low-noise Operations

In light of the preceding analysis, the reference configuration HALO will now be presented in accordance with the previously identified requirements.

First, the body frame of reference direction is the one indicated in Figures 3.4 and 3.5:

- x-direction: pointing to the nose
- y-direction: pointing to the left looking from the body perspective
- z-direction: pointing upwards

While the center position of the body-FoR is on the center of gravity (red-white dot in Fig. 3.4).

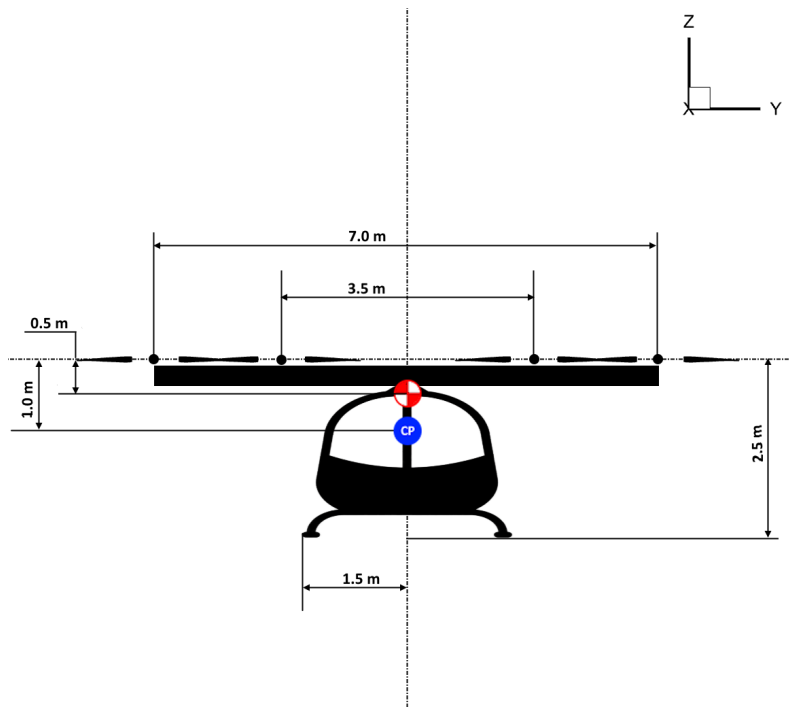


Figure 3.4: HALO front view.

This kind of frame convention has been selected in order to maintain the same axis direction of the UPM motion file (SubCh.2.2).

It is crucial to be noted that the UPM-frame is identical to the body-frame, with the exception of the fact that it is centred on a point with the same x,y coordinates as the CG, but in the plane described by the rotors (0.5 m above the centre of gravity). This point is called Geometric Center (GC) and it is reported in Figure 3.5 as a reference.

The center of pressure in which the aerodynamic drag vector of the fuselage is located, is indicated with a blue dot within the words "CP" in Figure 3.4. Moreover, the position of this point has been established as a preliminary assumption, and further studies will be required in order to more accurately characterize the configuration's geometry and drag model.

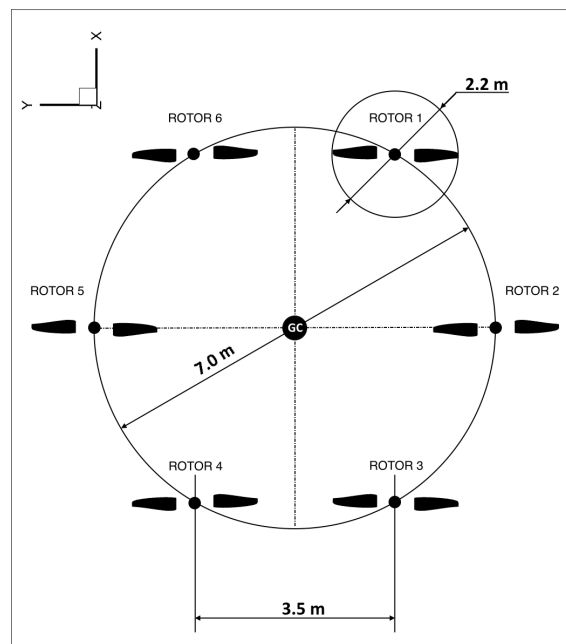


Figure 3.5: HALO upper view, flight direction coincident with x-direction.

It is important to note that, as a general rule, all rotors are named, starting with the first one in the top right-hand corner and continuing clockwise to the last one.

If not specified the direction of rotation of the rotors for all the configurations is defined as follows:

Rotors direction of rotation:	
ROTOR 1	counter-clockwise
ROTOR 2	clockwise
ROTOR 3	counter-clockwise
ROTOR 4	clockwise
ROTOR 5	counter-clockwise
ROTOR 6	clockwise

Table 3.4: Rotors direction of rotation.

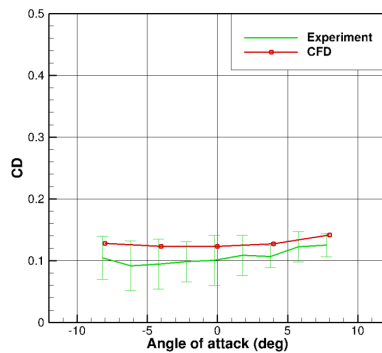
In general, if not specified, all odd rotors rotates in the counter-clockwise direction, whereas even rotors rotates in the clockwise direction.

3.5 Simplified Fuselage Drag Model

In order to assess the stability of the aircraft in forward flight, a drag model is required. Again, as modelling the fuselage is beyond the scope of this study, some realistic approximations have been made.

The drag of the rotors is taken into account in the aerodynamic simulations in UPM, while the drag of the fuselage requires appropriate modelling. In particular, the drag of the fuselage has been divided into two main components: the drag due to the cockpit and the drag due to the arms i.e. the structural connection between the hub of the motors and the central fuselage.

With regard to the first contribution, it has been modelled on the basis of a classic helicopter fuselage, with reference to Batrakov’s work in [32] for this purpose. This research provided experimental and numerical drag values for the AKTAY helicopter which has been used as reference cockpit in this study.



(a) Reference fuselage drag coefficient [32].

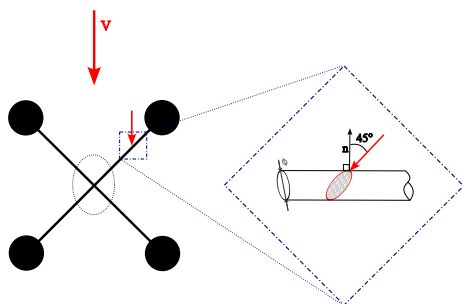


(b) Wind tunnel model of the AKTAY helicopter fuselage [32].

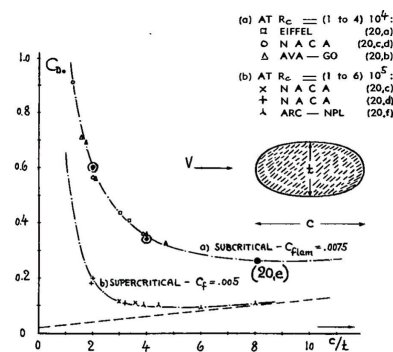
Figure 3.6: Reference fuselage drag model for the cockpit [32].

In order to model the drag of the arms, it is assumed that they are circular base cylinders with a diameter of 0.2 m .

In order to account for the angle of the flow received by each arm based on its orientation within the configuration, a geometric transformation was adopted. This transformation was necessary because the flow is not always directed towards the cylinder normal direction, and thus each arm’s sectional base must change to an ellipsoidal one.



(a) Geometric sectional transformation due to airspeed non-orthogonality.



(b) Drag coefficients of elliptical sections [33].

Figure 3.7: Arms drag model.

In figure 3.7a a brief representation of the geometric transformation for the easiest case of 4 rotors. In conclusion, the drag coefficients were derived from the book of Dr.-Ing Hoerner [33] for each sectional configuration (Fig.3.7b).

In light of the aforementioned considerations, some additional assumptions have been made:

- No fuselage lift contribution
- Constant drag with the pitch angle
- No contribution of the motors case
- Linear scaling of the fuselage dimension for each configuration

3.6 Simplified Inertia Model

One of the criteria for the success of the trim procedure that will be presented subsequently is the determination of the residual accelerations. This is done for two reasons: firstly, to facilitate an immediate physical evaluation of the trimming error; and secondly, in accordance with the Volocopter procedure [30], which employs the same criterion as a success measure.

In order to evaluate the residual rotational acceleration, it is necessary to assess an appropriate inertia model. To this end, the inertia contribution is split into two, in accordance with the approach previously employed for the drag model. The first contribution is that represented by the cockpit, which is modelled as an homogeneous sphere. The second contribution represents the rotor plane, which includes the arms and, presumably the batteries of the configuration, is modelled as a homogeneous disc fig.3.8.

As a final step, the total mass of the system is distributed in order to maintain the position of the center of gravity in accordance with the HALO model and the aforementioned geometry table 3.5.

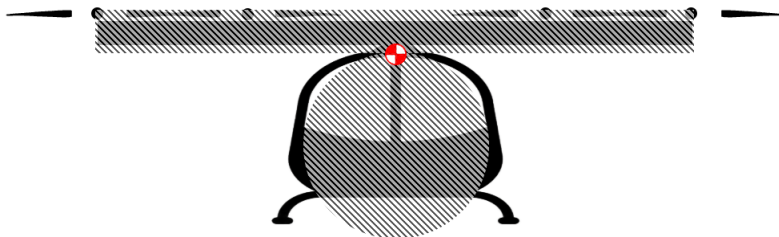


Figure 3.8: Inertia model visualization.

(a) Sphere Data		(b) Disc Data	
Radius	1 m	Radius	3.5 m
Mass	150 Kg	Height	0.5 m
Center	1.5 m from above	Mass	300 Kg
		Center	0.25 m from above

Table 3.5: Inertia contribution data.

In conclusion, the inertia matrix for the HALO configuration is presented for reference.

$$Inertia_{HALO} [Kg m^2] = \begin{pmatrix} 1210.0 & 0 & 0 \\ 0 & 1210.0 & 0 \\ 0 & 0 & 1897.5 \end{pmatrix}$$

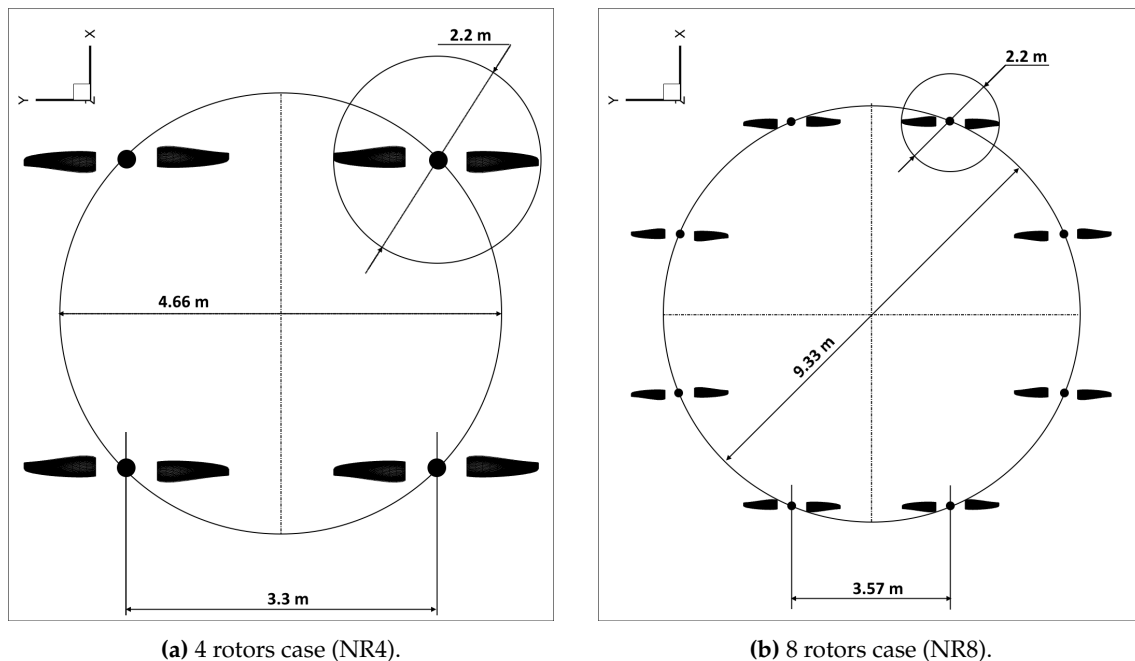
It should be noted that only steady flight is considered in this analysis. Therefore, the inertia matrix does not affect the flight state.

However, the matrix is used to compute the remaining rotational acceleration of the configuration in order to determine the convergence of the trim procedure, in accordance with the approach outlined in SubCh. 4.4.

3.7 Parametric Configurations

As previously indicated, the ability to parametrize the geometry is of fundamental importance to the study, as it allows for the investigation of the phase shift as a function of the number of rotors and the distance between two consecutive rotors.

To this end, two examples of parametric configuration are presented, which will be used in all subsequent analyses.



It should be noted that the drag and inertia models have been scaled in order to maintain the physical flight mechanics results, while the rotational velocity Ω is kept constant between the configurations in order to ensure aeroacoustic similarity.

In the end is worth noticing that for all the configurations, the blades geometry and sizing are kept constant within the configurations but the MTOW is scaled every time in order to have always the same disc loading for each rotor of each configuration.

Of course this is not the only way to conduct a parametric study and many other parameters variation can worth further investigations. For the sake of simplicity, all configurations are referred to as NR4, NR6, and NR8, depending on the number of rotors that are present.

Chapter 4

UPM Trim Script

4.1 Introduction

Once the geometric parameters of the configuration have been identified, it is necessary to ensure that the aircraft is in equilibrium before starting any type of simulation for aeroacoustic studies.

To achieve this, a trim procedure is required. The trim procedure aims to determine the necessary control inputs to maintain a steady flight condition.

Given the nature of the work, a numerical trim procedure supported by the UPM aerodynamic simulation code was chosen in order to take into account also the mutual aerodynamic interaction between the rotors.

A number of assumptions were made during the initial design phase, such as the possible flight conditions:

- Hover
- Forward flight
- Climb\Descent

Given the nature of the possible flight conditions, it has been decided to develop a trim procedure based on only 3 degrees of freedom (DoF) as a starting point. This assumption is validated by the fact that all the proposed geometries are symmetrical in the z-x and z-y planes, so there should be no problem when placed in a symmetrical flight condition. Numerical validation has been done during the study and the results are reported in SubCh.4.6 showing the goodness of this assumption with a certain error margin .

Nevertheless later in the study, the introduction of a phase shift between the rotors creates an asymmetry in the computational domain. In order to avoid instabilities due to this physical phenomenon, the degrees of freedom of the trim were subsequently extended to 6 DoF.

All the details of this correction will be explained in Ch.5, while in the following sections, for simplicity, all the results and procedures are reported for the 3 DoF trim.

4.2 Reference Frames Description

First of all, it is important to remember that the positions of the center of gravity of the entire configuration and the center of pressure of the fuselage are those defined in Fig. 3.4 and they are constant for all the configurations for simplicity.

Before starting with the trim explanation, it is important to define the frame of references that have been used during the analysis.

The "*body-frame*" is the one described in Figures 3.4 and 3.5 in Chapter 3, and this was decided to be consistent with the motion file input to UPM ("*UPM-frame*") except for the fact that the former is centered in the center of gravity, while the latter is centered in a point coincident with the gravity center but translated into the plane containing all the rotors. This point is called geometric center (see Fig. 3.5).

It is important to note that the "*hub-frame*" (green frame in fig.4.1) and "*body-frame*" (blue frame in fig.4.1) share the same orthogonal triad orientation and are body fixed according to the UPM output convention, while the trim forces and moments required to balance the external ones are calculated in an inertial frame centered on the center of gravity called "*trim frame*" (red frame in fig.4.1).

If not specified, the forces and moments are written in trim frame:

$$y_{trim} = \vec{y} = \begin{bmatrix} F_x \\ F_z \\ M_y \end{bmatrix} \quad (4.1)$$

Finally, it is important to note that, for the sake of clarity, the attitude angles convention has been retained as the standard one:

- Pitch angle (Θ): Positive if pitch up
- Roll angle (Φ): Positive if right side down
- Yaw angle (Ψ): Positive if heading to the right

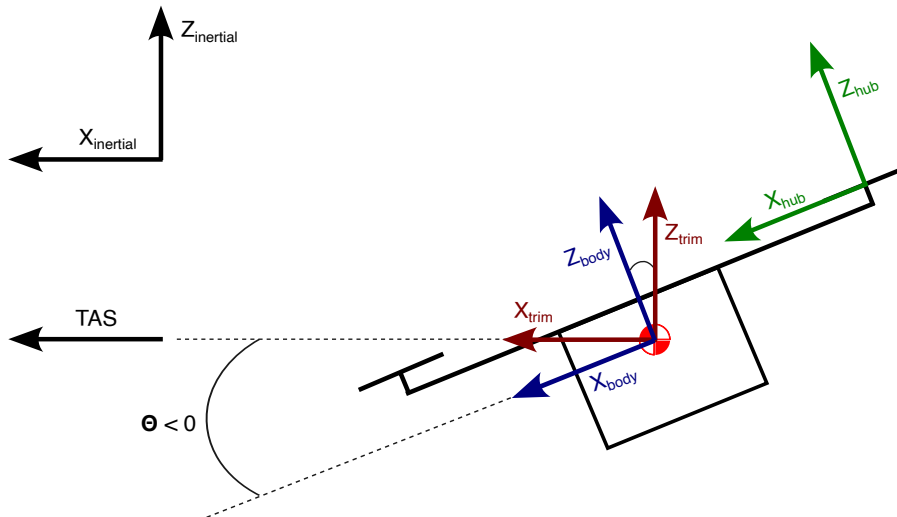


Figure 4.1: Trim conventions.

4.3 Mathematical Trim Structure

Once the trim frame of reference is outlined, it is necessary to define a trim vector containing the trim variables to be considered, having in mind the 3DoF assumption, only 3 variables are needed.

$$\vec{x} = \begin{bmatrix} x_1 \\ x_2 \\ x_3 \end{bmatrix} \quad (4.2)$$

As the system is a 3 DoF model, but with more control variables than necessary, known as an overdetermined system, it is essential to create a special mapping/mixer matrix. This matrix links the actual trim variables to all available system variables with a simple linear combination.

Of course, the type of mapping chosen may depend on many factors. For example, a combination that minimizes the average Sound Pressure Level (SPL) may be chosen, but this requires further study and is left as a suggestion for future research.

Matrix 4.3 in the following is the mapping matrix for the HALO configuration, reported as a reference, with descriptions for each row and column:

$$\text{MAPPING} = \begin{matrix} & x_1 & x_2 & x_3 & & \\ \begin{bmatrix} -1 & 1 & 0 \\ 0 & 1 & 0 \\ 1 & 1 & 0 \\ 1 & 1 & 0 \\ 0 & 1 & 0 \\ -1 & 1 & 0 \\ 0 & 0 & -1 \end{bmatrix} & & & & \begin{matrix} \theta_0^1 \\ \theta_0^2 \\ \theta_0^3 \\ \theta_0^4 \\ \theta_0^5 \\ \theta_0^6 \\ \Theta \end{matrix} \end{matrix} \quad (4.3)$$

Where $[\theta_0^1 \dots \theta_0^n]$ are the collective pitch of each rotor, used, together with the attitude pitch angle Θ , as the control variables for the variable pitch propeller configuration object of this study.

To initiate the trim procedure, the first step is to create a system model. This is achieved by linearizing the actual physics as a first first-order system through the computation of the Jacobian matrix.

The Jacobian matrix \mathbf{J} will be computed using the numerical results from UPM (see SubCh. 2.2) and will be thoroughly discussed later.

The linearized model is thus obtained in the discretized form:

$$\vec{y}^{n+1} = \vec{y}^n + \mathbf{J}|_{\vec{x}^n} \cdot \Delta \vec{x} \quad (4.4)$$

with:

$$\mathbf{J} = \frac{\partial \vec{y}}{\partial \vec{x}} = \begin{bmatrix} \frac{\partial y_1}{\partial x_1} & \frac{\partial y_1}{\partial x_2} & \frac{\partial y_1}{\partial x_3} \\ \frac{\partial y_2}{\partial x_1} & \frac{\partial y_2}{\partial x_2} & \frac{\partial y_2}{\partial x_3} \\ \frac{\partial y_3}{\partial x_1} & \frac{\partial y_3}{\partial x_2} & \frac{\partial y_3}{\partial x_3} \end{bmatrix} \quad (4.5)$$

$$\Delta \vec{x} = \vec{x}^{n+1} - \vec{x}^n \quad (4.6)$$

Having as trim forces:

$$\vec{y} = \begin{bmatrix} y1 \\ y2 \\ y3 \end{bmatrix} = \begin{bmatrix} F_x \\ F_z \\ M_y \end{bmatrix} \quad (4.7)$$

Since the trim objective is:

$$\vec{y}^{n+1} = 0 \quad (4.8)$$

the equation to be solved becomes:

$$0 = \vec{y}^n + \mathbf{J}|_{\vec{x}^n} \cdot \Delta \vec{x} \quad (4.9)$$

explicitly:

$$\vec{x}^{n+1} = -[\mathbf{J}|_{\vec{x}^n}]^{-1} \cdot \vec{y}^n + \vec{x}^n \quad (4.10)$$

Where \vec{x}^{n+1} is the control vector needed to balance the configuration.

It is important to note that if the trim objective is not 0 but a selected target value, the previous equations can be formulated as:

$$\vec{x}^{n+1} = [\mathbf{J}|_{\vec{x}^n}]^{-1} \cdot (\vec{y}_{target} - \vec{y}^n) + \vec{x}^n \quad (4.11)$$

maintaining the same meaning.

4.4 Criteria of Success

In steady-state conditions, the objective of a trim analysis is to identify the control inputs and states that result in quasi-zero residual accelerations, thereby ensuring that the aircraft maintains a constant velocity and orientation.

The residual accelerations can be calculated using Newton's second law, which can be applied to both translational and rotational motions of a rigid body.

According to Newton's second law, the total force acting on the center of mass \vec{F}_{tot} of a rigid body is related to the translational acceleration \vec{a}_{CM} of the center of mass by:

$$\vec{F}_{tot} = m \cdot \vec{a}_{CM} \quad (4.12)$$

where:

- m is the total mass of the rigid body.
- \vec{a}_{CM} is the translational acceleration of the center of mass.

In the context of the trim analysis, to achieve steady-state flight, the residual translational acceleration \vec{a}_{res} can be evaluated as:

$$\vec{a}_{res} = \frac{\vec{F}_{res}}{m} \quad (4.13)$$

where \vec{F}_{res} represents the residual forces acting on the body, due to trim imperfect convergence.

For rotational motion, Newton's second law states that the total moment \vec{M}_{tot} about the center of mass is given by:

$$\vec{M}_{tot} = \mathbf{I}_{CM} \cdot \dot{\vec{\omega}}, \quad (4.14)$$

where:

- \mathbf{I}_{CM} is the inertia matrix about the center of mass.
- $\dot{\vec{\omega}}$ is the angular acceleration vector.

In a steady-state trim condition, the goal is to annul the rotational accelerations. Thus, the residual angular acceleration $\dot{\vec{\omega}}_{\text{res}}$ can be expressed as:

$$\dot{\vec{\omega}}_{\text{res}} = \mathbf{I}_{\text{CM}}^{-1} \cdot \vec{M}_{\text{res}}, \quad (4.15)$$

where \vec{M}_{res} denotes the residual moments acting on the body, resulting from trim imperfect convergence.

In summary, the residual accelerations can be evaluated in matrix form as follows:

$$\begin{bmatrix} \vec{a}_{\text{res}} \\ \dot{\vec{\omega}}_{\text{res}} \end{bmatrix} = \begin{bmatrix} \frac{1}{m} & 0 \\ 0 & \mathbf{I}_{\text{CM}}^{-1} \end{bmatrix} \cdot \begin{bmatrix} \vec{F}_{\text{res}} \\ \vec{M}_{\text{res}} \end{bmatrix} \quad (4.16)$$

To achieve trim conditions, both \vec{a}_{res} and $\dot{\vec{\omega}}_{\text{res}}$ should approach zero. This implies that the applied forces and moments must counterbalance each other in order to maintain steady-state flight. In order to assess a realistic criterion of success for the trim procedure, it was necessary to consider the approach taken by Volocopter as outlined in [30]. In this case, two threshold values have been set for the residual accelerations reported in Table 4.1. These values have been used also in this research to assess for trim convergence.

Volocopter thresholds	
$ \vec{a}_{\text{res}} $	0.1 m/s^2
$ \dot{\vec{\omega}}_{\text{res}} $	0.025 rad/s^2

Table 4.1: Volocopter criteria of success [30].

Finally, it can be reasonably assumed that a trim procedure has been successfully converged if the residual accelerations are found to be below the aforementioned thresholds.

4.5 Trade-offs in Script Design and Methodology

4.5.1 Operative Pitch Range Definition

As a preliminary step, it was necessary to compile a thrust versus collective pitch (θ_0) polar plot of a rotor in order to gain insight into the operational pitch range that could be utilized for multirotor control Fig.4.2.

It is important to note that, as UPM is a potential flow code, there is no direct information available regarding the separation of the flow on the propeller. Nevertheless, an internal UPM option allows for an estimation of the separation condition through the examination of the shape factor with an approximate boundary layer analysis (see SubCh.2.2, [23]).

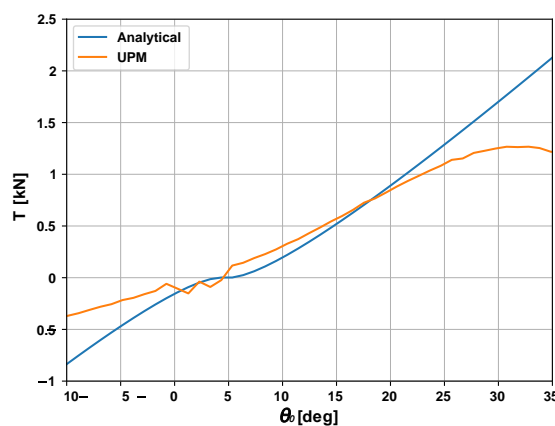


Figure 4.2: Thrust vs θ_0 plot for a single rotor.

The aforementioned option enabled a rough evaluation of an acceptable range of θ_0 , which was employed to verify the goodness of the propeller scaling design and to establish a reference range for the numerical trim procedure and for the analytical model proposed in Ch.7. The analytical curve in 4.2 employs the set of equations proposed by Talbot [34].

Given that the design pitch of the propellers is 15 degrees [28], a conservative upper limit of 20 degrees of pitch was assumed.

It is important to notice that the collective pitch θ_0 is measured from the root cut out distance, this choice has been made due to the fact that this kind of convention is the one adopted in the UPM motion file.

Finally, a few words about the θ_0 region between 0 and 5 degrees. This scattering behaviour of the UPM polar line can only be justified by looking at the simulated wake of the UPM computation. In fact, at low collective pitch angles, the rotor cannot push the wake far away from the rotor itself causing instabilities and the impossibility to reach a good convergence. Such instabilities are due to the presence of the wake itself inside the propellers trajectory during their rotational motion around the shaft.

4.5.2 Pseudo Steady State Condition

Given that UPM is an unsteady free-wake method, it is of the utmost importance to reach a pseudo steady state condition before taking any further action.

This can be achieved by waiting until the periodic convergence of the aerodynamic forces (Fig.4.4a), that is to say, until the wake produced by the starting vortex is sufficiently far away from the rotors (Fig.4.3).

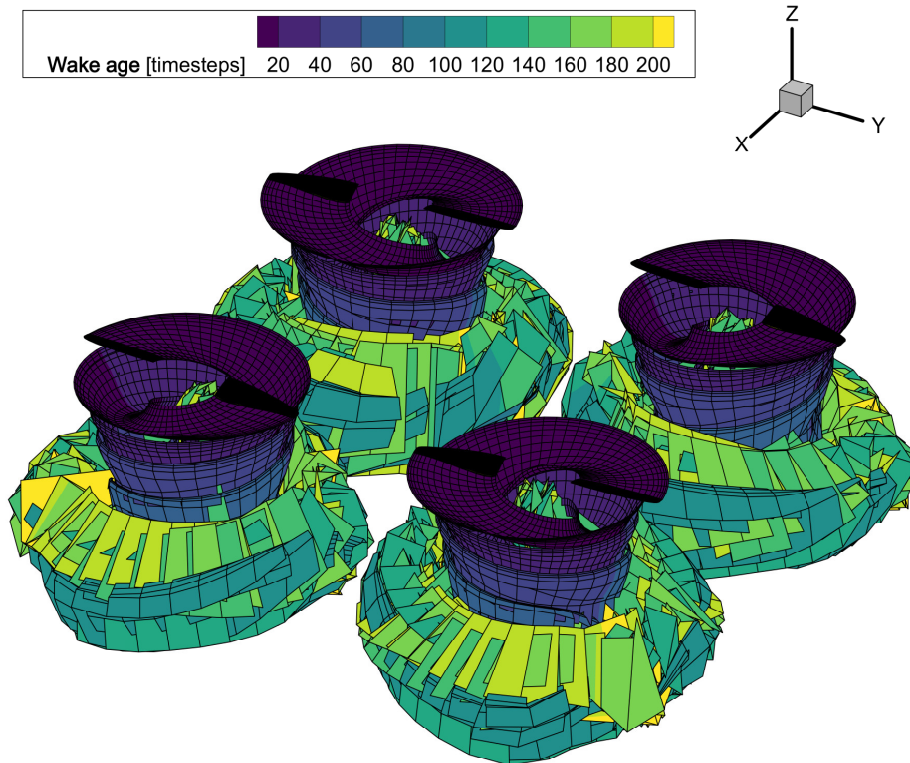


Figure 4.3: Wake development and aging in UPM time-steps.

However, as this has to be an automatic script, it is important to minimize the user interaction. To this end, an iterative algorithm has been implemented in order to check automatically for convergence and to stop the simulation once it is reached. Briefly, the algorithm starts computing UPM one revolution at time, and for every revolution it takes the output results from the "thrust.tec" (see. 2.2) file. In order to ascertain the convergence criteria, a straightforward error calculation is employed, whereas the tolerance is defined by the user as a percentage of the total thrust of the configuration.

In the following is reported a simplified description of the algorithm architecture (Alg.1)

Algorithm 1 Steady state algorithm

```

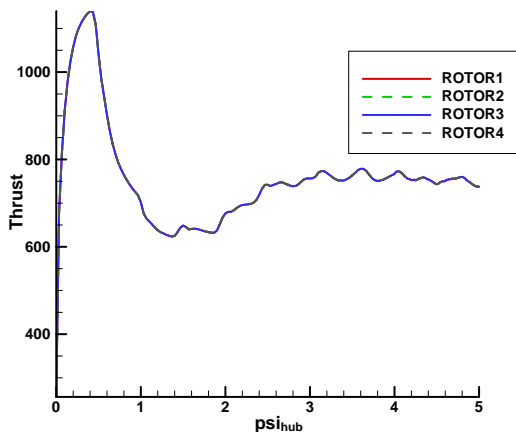
1: Input:
2:
3:   toll_perc                                ▷ Thrust percentage of tolerance
4:   max_rot                                  ▷ Maximum number of revolutions
5:   Stepsize                                ▷ stepsize length for the UPM computations
6:
7: Initialization:
8:
9: error → 1
10: tolerance → 0
11: i → 1
12:  $T^{i-1} \rightarrow 0$ 
13:
14: while error  $\geq$  tolerance and i  $\geq$  max_rot do
15:
16:   Run (or restart from the previous revolution) UPM for one revolution
17:    $T^i \rightarrow$  Read the output Thrust averaged over the revolution.
18:   tolerance =  $T^i \cdot toll\_perc$ 
19:   error =  $\|T^i - T^{i-1}\|$ 
20:
21: end while

```

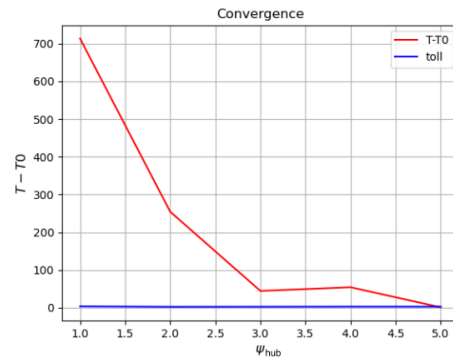
In conclusion, an example of the convergence plot (Fig. 4.4b) is presented as an output to the user, allowing for a visual assessment of the convergence of the computation.

It is of interest to note that the thrust steady oscillation is not perfectly smooth, contrary to what might be expected for a single rotor. This is due to the mutual aerodynamic interaction between the rotors in the configuration and a slightly non-periodic evolution of the wake.

Despite that, it is possible to see that the thrust behaviour is periodically stable for all the rotors of this kind of configuration (4 synchronized rotors with zero phase shift)



(a) Thrust [N] behaviour vs number of revolutions, output of the UPM computation.



(b) Example of algorithm convergence check: error vs ψ_{hub} (number of revolutions), output of the trim script.

Figure 4.4: Thrust and error behaviour as a function of the number of revolutions. For further details regarding the angles conventions, please refer to Nomenclature and Conventions.

4.5.3 First Preliminary Script Implementation

As an initial approach to the problem, the strategy was to be as precise as possible in both the steady state condition and the computation of the Jacobian matrix, and to complete the trim in a single step. In theory, if the Jacobian matrix is well defined and the problem at hand is linear, a good result should be achieved immediately, particularly in the hover condition where no attitude variation due to trim is expected, but only an increase in collective pitch for all rotors.

With regard to the procedure for reaching steady state, an highly restrictive tolerance percentage of 0.1% of the total system thrust was set, resulting in a convergence after 30 revolutions in accordance with the previously outlined scheme (Algorithm 1).

In order to achieve the highest possible accuracy in the computation of the Jacobian matrix, it was necessary to ensure that the system re-converged with a 0.1% thrust tolerance for each input variation. This process was repeated before computing each column, while the computation of the column itself is done following Eq. 4.17:

$$\mathbf{J}(:, \mathbf{i}) = \frac{\partial \vec{y}}{\partial x_i} = \begin{bmatrix} \frac{Fx_i - Fx_{reference}}{\delta} \\ \frac{Fz_i - Fz_{reference}}{\delta} \\ \frac{My_i - My_{reference}}{\delta} \end{bmatrix} \quad (4.17)$$

With:

- $()_{reference}$ are the output forces and moments from the steady UPM computation.
- $()_i$ are the output forces and moments computed after a variation of the i -input of magnitude δ .

The Jacobian was computed using the finite difference method by applying perturbations to each control variable and evaluating the difference between the perturbed and unperturbed outputs. The magnitude of the disturbance was assumed to be unitary. Although no specific study was conducted to determine the optimal disturbance magnitude, it was observed that small perturbations can lead to an ill-defined Jacobian matrix. This is because the resulting differences are more affected by the system's numerical instabilities rather than the applied perturbation itself.

4.5.4 Second Preliminary Script Implementation

As a second approach, the potential for a less rigorous precision of the steady state convergence and the Jacobian matrix was investigated. Instead, the process of trimming was iterated until the required forces matched the ones from the desired flight condition within a certain tolerance.

The jacobian matrix is then computed every cycle step. This is done by utilizing the outcomes of the preceding iteration's revolution computation as reference values and then conducting a single revolution simulation with the input variable modified, without waiting for convergence.

This choice was made to save computational time and to compare the results with the previous methodology in order to produce the best possible algorithm in terms of accuracy, customization, and speed of result production. A schematic visualization of the algorithm is presented in Fig.4.5

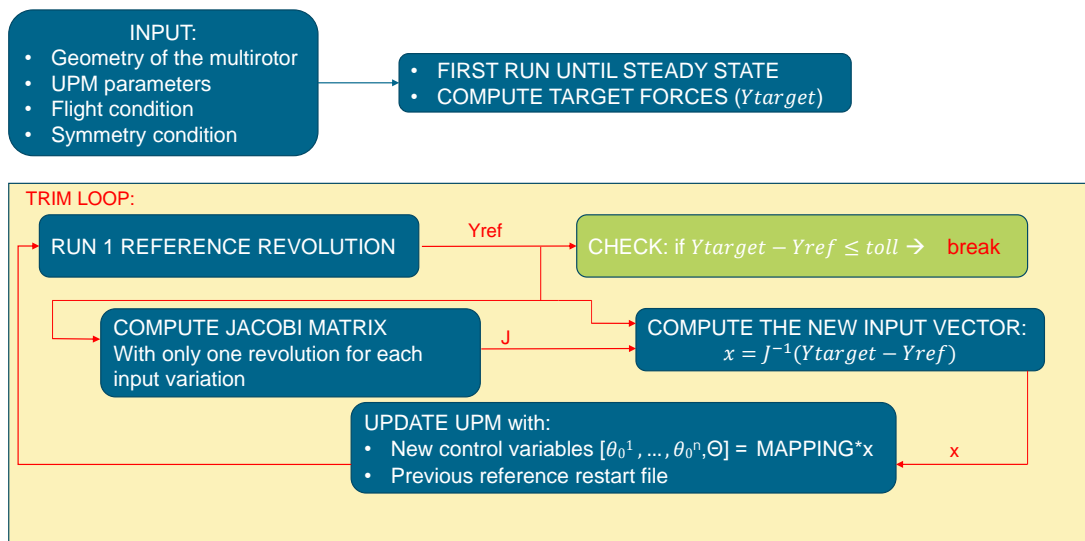


Figure 4.5: Second preliminary script simplified structure.

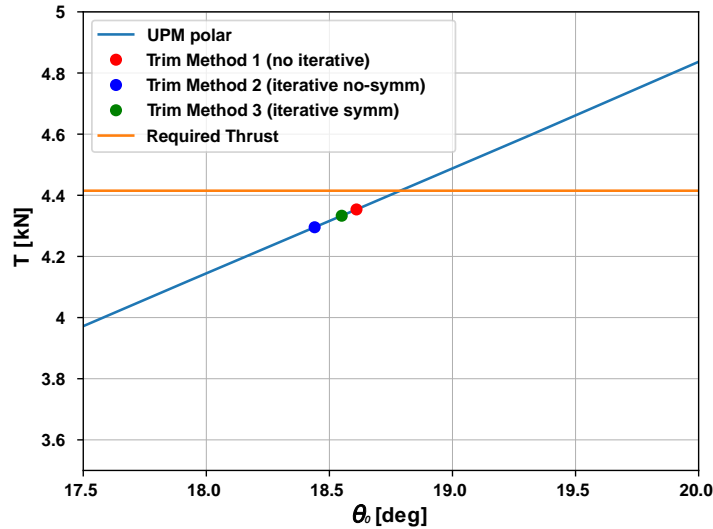
A further function incorporated into this second algorithm is the introduction of a symmetry condition that effectively halves the computational domain by incorporating a y-z symmetry plane.

The aforementioned symmetry plane is initially implemented within UPM, which consequently considers only those rotors that are geometrically positioned at $y > 0$, and projects the flow results for the rotors situated at $y < 0$. The same symmetry plane is then considered in the evaluation of the total forces and moments of the configurations. This function is available in UPM for modelling ground effect and was considered for inclusion in this algorithm due to the intrinsic symmetry of the problem. The results and considerations obtained from this option will be discussed in detail in Sub.4.5.5.

4.5.5 Comparison and Final Script Implementation

In order to identify the optimal compromise between the two philosophies of the preliminary scripts, an overview of results for a simple hover condition for the reference HALO configuration has been conducted.

Figure 4.6a presents the various trim results of the different trim procedures, while Table 4.6b outlines the principal performance parameters considered in the final trade-off.



(a) Trim results comparison with a reference polar Thrust vs collective pitch (θ_0) curve. Please note that the collective pitch is the same for all the 6 rotors in hover condition

	Trim method 1	Trim method 2	Trim method 3
Relative error	1.39 %	2.71 %	1.85 %
Computational time	30h	3h	1.5h

(b) Main performance parameters for each trim method.

Figure 4.6: Different Trim implementation results and comparison.

Description:

Trim Method 1: refers to the single Jacobi computation approach (Sub.4.5.3)

Trim Method 2: refers to the iterative trim cycle approach (Sub.4.5.4)

Trim Method 3: refers to the iterative trim cycle approach with the application of the symmetry plane (Sub.4.5.4)

Main UPM parameters (Section.2.2):

$Stepsize = 12$, $r0_core = 0.1$

As evidenced by the results, the initial algorithm demonstrates the anticipated performance characteristics: it exhibits greater precision in the context of the hover condition, yet it is also the most time-consuming, despite a single computation of the Jacobian matrix. As expected, the second algorithm is more time-efficient and produces an error of a similar order of magnitude to the first.

The considerable time consumption associated with Method 1 can be attributed to the

fact that the computational time for each step increases in proportion to the dimension of the wake (see [23]). Consequently, if convergence is allowed to occur too slowly, the overall wake length will be greater, necessitating a greater amount of time for the entire process to be completed.

With respect to the symmetry condition, the algorithm in evidence appears to demonstrate enhanced efficiency compared to the conventional algorithm 2. This is due to the fact that the application of a "mirror" in the computational domain permits a faster calculation and avoids the introduction of asymmetries that are not physical but purely numerical. It should be noted that these asymmetries are relevant in this study case due to the low dimension of the vortex core radius (ref. 2.2), which was not previously tuned. This resulted in a more chaotic domain which has been useful to evaluate the robustness of the algorithms.

However, later on the study it has been observed that the symmetry condition is much less robust in other flight conditions and with other geometries, such as the 8-rotor configuration where the distances between the rotors and the symmetry plane are smaller. For this reason, despite its inclusion in the final trim script, it will not be used further. Another reason why this option will not be considered in future is precisely the subject of this study: the use of this assumption would result in the loss of all information related to the mutual aerodynamic interference due to the phase shift of the specular rotors.

In consideration of the aforementioned comparative analysis, it was determined that an algorithm incorporating all of the principal features that have been discussed so far should be developed. The final algorithm must ensure convergence at each step, while its iterative nature allows relaxing tolerance across various steps, thus ensuring overall trim precision without excessive waiting

The final 3DoF trim algorithm is presented in detail in Algorithm 2.

The overall structure of this algorithm is analogous to the one in Fig.4.5, with the incorporation of a convergence assessment during the Jacobi calculation. This has been done in accordance with the methodology outlined in Algorithm 1. Firstly it is essential to monitor the convergence process initially due to the unsteadiness of the system. Furthermore, it is necessary to reassess the convergence status following any alterations to the system's physical parameters during the Jacobi matrix computation.

In particular, the convergence of each Jacobi column computation is verified by checking for the thrust mean value difference between two consecutive revolutions. If the absolute value of the difference between the two is less than a predefined threshold, the computation is assumed to have converged with the selected accuracy.

Algorithm 2 3DoF Trim Procedure

```
1: Input:
2:
3:   Trim_tolerance                                ▷ tolerance for the trim loop
4:   Jacobi_tolerance                              ▷ tolerance for the Jacobi convergence
5:   Max_step_Jacobi
6:   Max_step_trim
7:   Skip_step                                    ▷ number of steps in which the Jacobi matrix is kept constant
8:   Environment parameters
9:   Flight condition parameters
10:  Rotors_number
11:  UPM simulation parameters
12:
13: Initialization:
14:
15: Run Algorithm 1 to reach steady state condition
16: Compute target forces and moments:  $[-D_{fuselage}, -W, -My_D]'$     ▷ Drag model 3.5
17: Set step  $\rightarrow 0$ 
18: Set  $\vec{x}_0 \rightarrow [0, 0, 0]'$ 
19: Set  $\vec{Y}_{target} \rightarrow [Fx_{target}, Fz_{target}, My_{target}]'$ 
20:
21: Trim loop:
22:
23: while error  $\geq$  Trim_tolerance and step  $\leq$  Max_step_trim do
24:
25:   Compute  $Control\_variables = MAPPING_{matrix} \cdot \vec{x}_0$ 
26:   Run UPM with  $Control\_variables$  and read output forces  $\vec{Y} = [Fx_{ref}, Fz_{ref}, My_{ref}]'$ 
27:
28:   for each input column of  $\vec{x}_0$  do
29:
30:     Update UPM motion file with control variables for the input vector column
31:     Set  $i \rightarrow 0$ 
32:
33:     while Jacobi_error  $\geq$  Jacobi_tolerance and  $i \leq$  Max_step_Jacobi do
34:       ▷ while loop to check UPM convergence
35:       Restart UPM for one revolution    ▷ from the reference or the previous one
36:       Compute Jacobi_error  $\rightarrow \|T^i - T^{i-1}\|$ 
37:       Increment  $i$ 
38:
39:     end while
40:
41:     Collect last output  $[Fx, Fz, My]$ 
42:     Compute the J column                                ▷ see. 4.17
43:
44:   end for
45:
46:   Compute new trim vector  $\vec{x} = -[J]^{-1} \cdot (\vec{y} - \vec{r}_{ref}) + \vec{x}$ 
47:   Update  $\vec{x}_0 \rightarrow \vec{x}$ 
48:   Compute error  $\rightarrow |max(\vec{y} - \vec{y}_{target})|$ 
49:
50: end while
```

4.6 3DoF Trim Results

Following the implementation of the trim script, it was essential to start a testing procedure to evaluate its efficiency and accuracy. The first step in this process involved establishing simulation parameters in UPM, as outlined in Appendix A.

In particular, based on the findings of Sessini [8], the vortex core radius, the most important parameter, was selected to replicate the results obtained in the NASA experiments [6]. Note that to apply these findings to the scaled version of the rotors, it was crucial to perform all simulations using dimensionless parameters, ensuring that the experimental verified results could be effectively scaled to the actual rotor configurations.

The detailed results from this simulation campaign are presented in Appendix A.

Below (Tab. 4.2, 4.3), a schematic summary of the most significant results is provided to support a comprehensive analysis and to draw the necessary conclusions.

	4 ROTORS	6 ROTORS	8 ROTORS
Control Variables: $[\theta_0^1, \dots, \theta_0^n, \Theta]^\circ$	[18.37, 18.37, 18.37, 18.37, 0]	[18.49, 18.42, 18.34, 18.34, 18.42, 18.49, 0]	[18.55, 18.55, 18.55, 18.55, 18.55, 18.55, 18.55, 18.55, 0]
Y_target: $[F_x, F_z, M_y]$	[0, 2943, 0]	[0, 4414.5, 0]	[0, 5886, 0]
abs_error: $ \vec{Y} - Y_target $	[1.48e-10, 0.35, 8.28e-09]	[0.756, 2.435, 0.598]	[3.49e-09, 5.37, 7.60e-08]
residual translation acceleration	1.1693e-03	5.7709e-03	8.9484e-03
residual rotational acceleration	4.1605e-04	2.0812e-02	1.2515e-04

Table 4.2: Hover condition.

Regarding the Level Forward Flight condition, the speed for this preliminary investigation was based on the maximum cruise speed of the Volocopter 2X (reported in tab 3.2). The chosen speed is 28.33 *m/s* which is equivalent to 102 *km/h*.

The effects of steady climb and descent have been tested, but are not reported here for simplicity.

	4 ROTORS	6 ROTORS	8 ROTORS
Control Variables: $[\theta_0^1, \dots, \theta_0^n, \Theta]^\circ$	[16.01, 17.49, 17.49, 16.01, -9.29]	[17.02, 17.38, 17.73, 17.73, 17.38, 17.02, -12.13]	[18.81, 18.81, 18.99, 18.99, 18.99, 18.99, 18.81, 18.81, -16.352]
Y_target: $[F_x, F_z, M_y]$	[350.72, 2943, -175.36]	[735.40, 4414.5, -367.70]	[1384.1 5886.0, -692.07]
abs_error: $ \vec{Y} - Y_target $	[0.38, 2.52, 0.28]	[0.38, 1.93, 0.29]	[0.15, 0.20, 0.61]
residual translation acceleration	8.4864e-03	4.3720e-03	7.4266e-04
residual rotational acceleration	6.2303e-04	2.8250e-04	2.1955e-03

Table 4.3: Level Forward Flight condition, TAS = 28.33 *m/s*.

First of all, taking a look at the control variables, it is possible to see that for each flight condition and configuration (4,6,8 rotors), the collective pitch (θ_0) of each rotor never exceeds the predefined maximum value of 20° (discussed in SubCh. 4.5.1). This observation supports the assumption that the rotors' sizing procedure has been conducted correctly.

With regard to the attitude pitch angle Θ it can be observed that it is present obviously only in Forward Flight condition and for all the configurations, the magnitude of such angle is always reasonable. This confirms that the simple drag model adopted in SubCh.3.5 represents an appropriate starting point. The negative sign of the angle is also consistent with the physics of the system, in fact, in Forward Flight a pitch down attitude is necessary to counteract the total drag of the configuration.

Remaining focused on the Forward Flight condition, it can be observed that it is present a delta collective between the front rotors and the back ones. This effect it is also consistent with the physics and it is necessary to counteract the pitching moment taking into account also the differing flow condition between the rotors and the rotors drag itself.

It can be demonstrated that the rear rotors are affected by the downwash of the upstream rotors (see Fig.4.13), which results in a reduction in thrust with the same collective pitch input.

With regard to the trim procedure itself, it can be seen that the maximum errors are very small in comparison to the forces applied to the system, in particular, as requested by the script, they are always below 0.1% of the total thrust for each configuration.

As previously outlined in SubCh.4.4, in order to establish an additional criterion for the evaluation of the trim procedure's success, inspiration was drawn from the Volocopter numerical trim procedure (ref.[30]) in which a residual accelerations evaluation has been conducted.

Volocopter set the maximum residual translation and rotational acceleration respectively at 0.1 m/s^2 and 0.025 rad/s^2 . The results presented here, based on the inertia model outlined in SubCh. 3.8, consistently fall below the specified limits, thereby confirming the efficacy of the trim algorithm.

The following sections present a deeper examination of the results for both flight conditions.

4.6.1 Hover

Following the assessment of the trim results, a further investigation into the underlying physics of the problem is required to understand the lack of collective symmetry present in the hover case for all the rotors of the six rotors configuration.

Before doing so, it is needed to specify that all the rotors during the simulation are synchronized between each other, so conducting a set of simulation with zero phase shift, like the one proposed in this section, it does not lead to the neglect of mutual phase synchronization interaction.

A simple visualization of the blades motion during a single revolution is presented in Figures 4.7, 4.8 and 4.9.

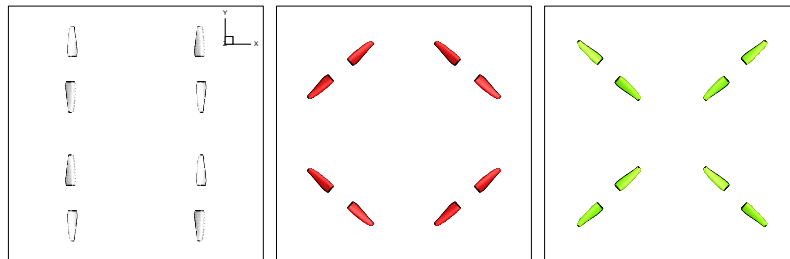


Figure 4.7: NR4 visualization, from the left: $\psi_{hub} = 0^\circ$, $\psi_{hub} = 45^\circ$, $\psi_{hub} = 135^\circ$.

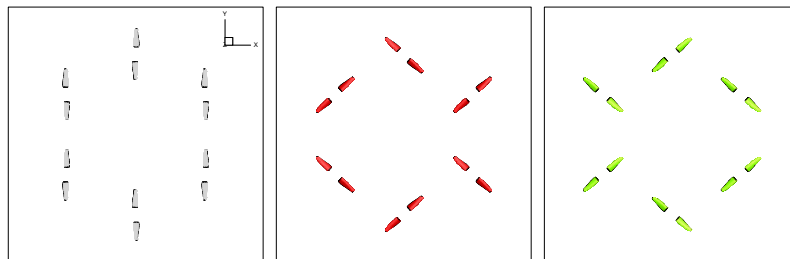


Figure 4.8: NR6 visualization, from the left: $\psi_{hub} = 0^\circ$, $\psi_{hub} = 45^\circ$, $\psi_{hub} = 135^\circ$.

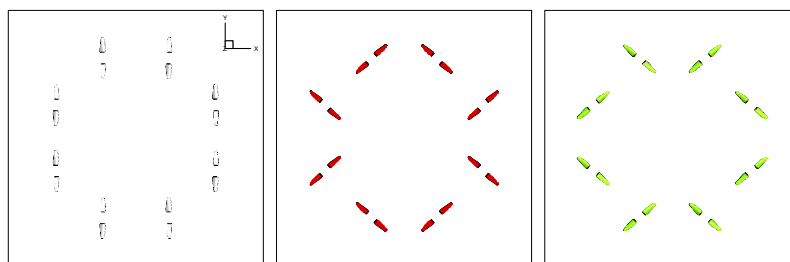


Figure 4.9: NR8 visualization, from the left: $\psi_{hub} = 0^\circ$, $\psi_{hub} = 45^\circ$, $\psi_{hub} = 135^\circ$.

In these, it can be observed that during the rotation of the propellers, NR4 and NR8 are always symmetrical, with respect to the x - z and y - z planes passing through the origin, for each value of the azimuthal coordinate.

This kind of symmetry lead to the fact that each propeller is "encountering" the adjacent one in a tip-to-tip configuration in the same time, and so the mutual interference between each rotor is always the same at every time.

This is not true for the 6 rotors case, in which it can be observed that the presence of two propellers along the y-axis results in a certain degree of asymmetry within the domain and in the fact that the propellers are "encountering" the others in different configurations.

In an ideal scenario of unsynchronized rotors, this asymmetry would not lead to any notable differences in the forces. This is because the mutual interaction effects should always be present, but the rotors are free to change their rotational speed, resulting in a less pronounced magnitude of this effect. Furthermore, if the rotors have a slight difference in RPM, the time-averaged effect will be very small.

Therefore, it is necessary to identify the underlying mechanisms that may be responsible for such outcomes:

The mutual aerodynamic interaction between synchronized rotors is dependent on the phase shift between them.

As will be explained in greater detail in Ch.5, the phase shift between rotors have a small effect on the Flight Mechanics of the system and it is this kind of effect that is responsible for the observed asymmetry in the collective pitch between the rotors.

The script in fact, is capturing that the thrust distribution in the domain is not symmetrical and so some rotors are pushing more than others and then it starts to compensate adjusting the collective of each rotor.

It is evident that this effect is of a substantially lower magnitude in comparison to the other forces that are present within the system. Consequently, the impact on the control variables is also small, estimated to be within the range of 0.1 degrees.

Finally, it is important to note that in a 3DoF trim procedure it is not possible to have full control of each rotor collective input individually, and so, the M_x, M_z, F_y small errors presents in Appendix A are impossible to counteract.

More details will follow in Ch. 5.

4.6.2 Level Forward Flight

In order to more accurately assess the trim results in forward flight, a series of simulations with varying velocities have been conducted using the four rotor configuration. This has been done for two reasons: firstly, to gain insight into the robustness of the algorithm, and secondly, to have a better visualization of the physics of the system in forward flight.

It was found that for low values of the advance ratio (μ), the convergence of the trim procedure is not assured. Indeed, if the forward speed is too low, the wake of the frontal rotor is completely injected by the back ones causing an unsteady and not periodical oscillation of the loads in the latter.

This phenomenon is reinforced by the fact that the attitude at low speed presents very small pitch angle and so the wake, that is convected away by the forward velocity, is moved towards the rear rotors.

Figure 4.10 provide a visual representation of the issue. In this figure, rotor 1 and 2 of the four rotor configuration are represented in forward flight at 10 m/s, with an estimation of the pitch angle derived from analytical reasoning.

In this initial analysis, only one front rotor (ROT 1) and one aft rotor (ROT 2) are presented for purposes of clearer visualisation, on the verified assumption that the behaviour exhibited by these rotors is exactly replicated by rotors 3 and 4.

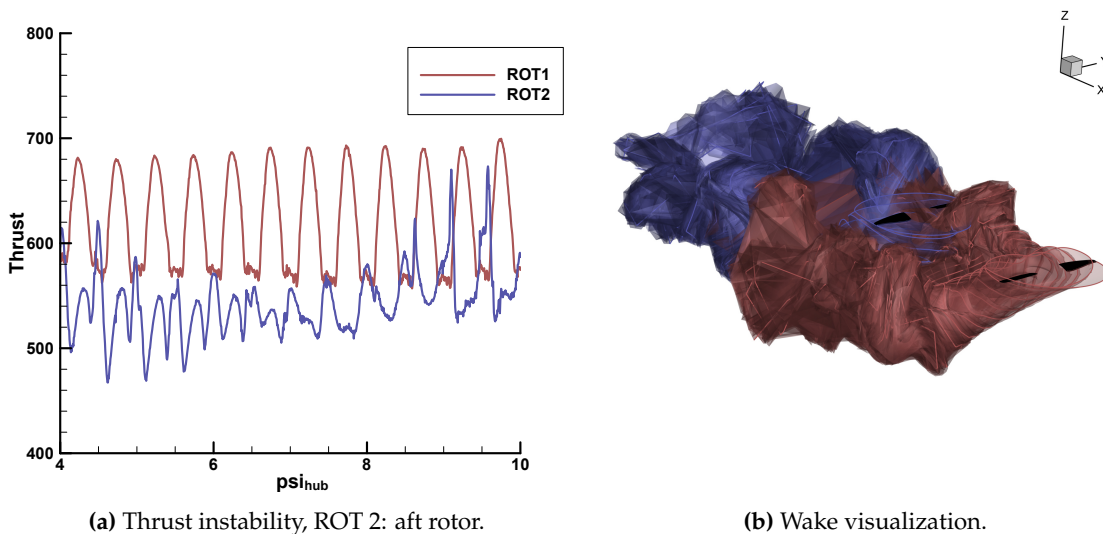


Figure 4.10: Simulation behaviour at low speed (10 m/s, $\Theta = -2$).

In Fig. 4.10a the aft rotor presents an unperiodical thrust behaviour with an oscillation delta of the order of 100 N, which is particularly sensitive to the pitch attitude, thereby creating an inherent difficulty for the trim script to converge with a certain precision.

Figure 4.11 illustrates an ordinary trimmed situation at 28 m/s, in which the thrust of the rear and front rotors remains unsteady but periodic, thereby facilitating convergence for the system.

In Figure 4.11b it is possible to appreciate how the wake develops without being injected

by the rear rotors. This is due to the configuration having a more pronounced pitch attitude angle, which allows for the wake to develop without interference from other rotors. Additionally, the higher trim speed plays a crucial role in facilitating the convection of the wake within the domain.

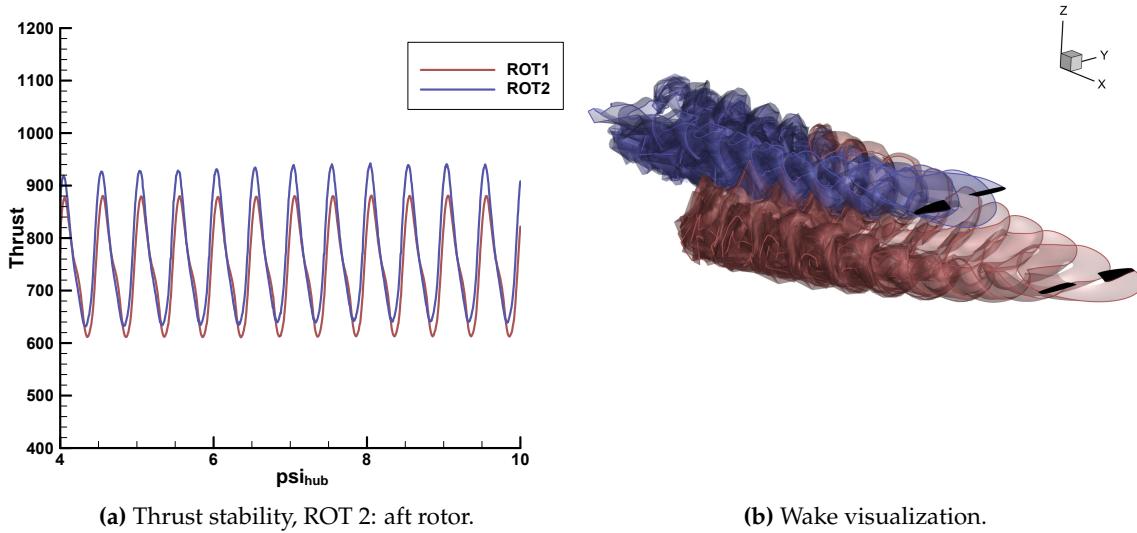


Figure 4.11: Simulation behaviour at high speed (28 m/s, trimmed).

Finally, a deeper analysis of the wake results from the UPM simulations has led to the conclusion that a reasonable lower boundary velocity for the trim procedure is 15 m/s or $\mu = 0.125$.

Going back to the trim results, Fig. 4.12, 4.12b report the control variables results of the aforementioned forward flight simulations with $TAS=[0, 15, 18, 20, 23, 25, 28, 30]$.

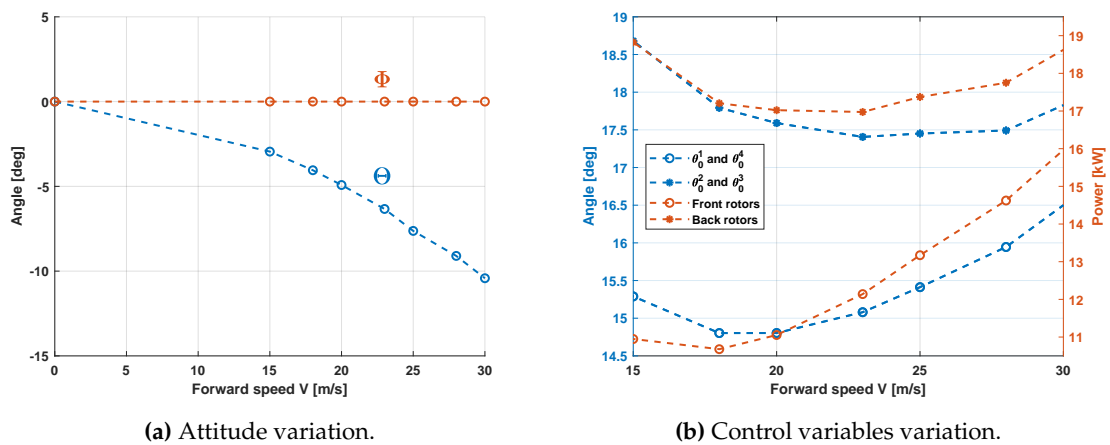


Figure 4.12: Trim results for different advancing speeds.

From the attitude diagram (Fig. 4.12a) it can be observed that, as expected, the pitch angle increases in magnitude in proportion to the forward speed, with the objective of counteracting the total drag of the configuration.

The control variable diagram on the right (Fig. 4.12b) shows the results only in the range between 15 and 30 m/s. This has been done in order to facilitate a clearer visualisation of the collective pitch and power behaviour in relation to the TAS. The control variables results for the hover condition (0 m/s) are those previously reported and thus not repeated here.

In the latter case, there is no variation between the two power and collective curves because the flow conditions of the front and aft rotors are identical.

With regard to the rotors' collective pitch (Fig. 4.12b) it can be seen that there is always a delta between the front and the rear ones, this is introduced by the system in order to counteract the inherent pitch up moment of the system ($M_y < 0$).

From a physics perspective, this kind of moment can be attributed to three primary factors. The first is the fact that the back rotors must operate within the inflow of the front rotors. Consequently, the local angle of attack experienced by the blades during their motion is reduced in comparison to the front rotors, resulting in reduced thrust and a pronounced pitch-up moment.

An evaluation of the inflow variation in forward flight has been done by Guan in [14] (reported as a reference in Fig. 4.13).

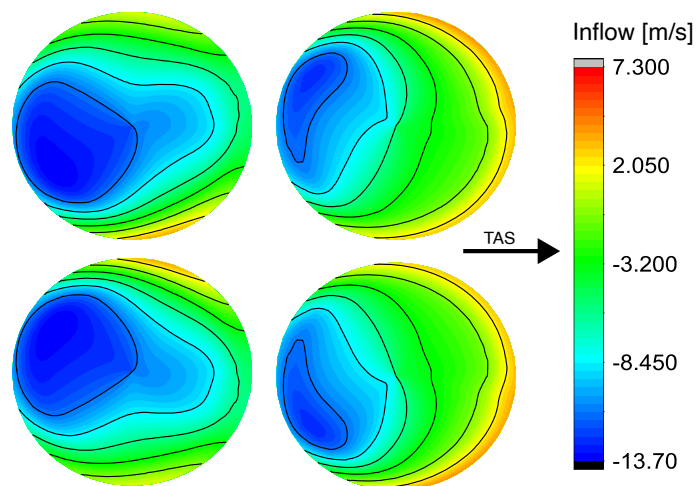


Figure 4.13: Inflow distribution, from [14], TAS = 10 m/s.

The second contribution is the pure rotor moment, which is transferred directly to the configuration as a result of the system being composed of rigid rotors. This negative y-moment is caused by the inflow difference inside the rotor disc during forward flight, and a visual representation of this can be found later in the study in Figure 5.4.

The final contribution to the pitch-up moment comes from the drag of the rotors themselves. It is important to note that the fuselage drag also contributes to the balance of the y-moments, creating a pitch-down effect due to the centre of pressure of the fuselage positioned below the center of gravity.

In the end it is possible to appreciate that the delta θ_0 between the rotors is decreasing with the increase of the forward speed, this is due to the fact that the fuselage drag is increasing and so the positive pitching moment created by the inclination of the total thrust and the fuselage drag, helps the configuration asking for less differential thrust.

In Figure 4.12b it is also possible to appreciate an estimation of the power required by the rotors. It is important to note that the presented estimation has been made without taking into account the viscous effects, and therefore the profile drag and torque have been neglected.

It should also be highlighted that the collective pitch of the rotors is following the trend of their own power, which in this graph has been divided into two contributions: one for the front rotors and one for the rear ones.

In particular it is possible to appreciate that the point of minimum of the two power curves are different, and the rear rotors exhibit a minimum ($V = 23$ m/s) shifted at higher speed with respect to the front ones ($V = 18$ m/s).

This effect can be only explained taking a look into the power curve of a generic helicopter rotor shaft, in Figure 4.14.

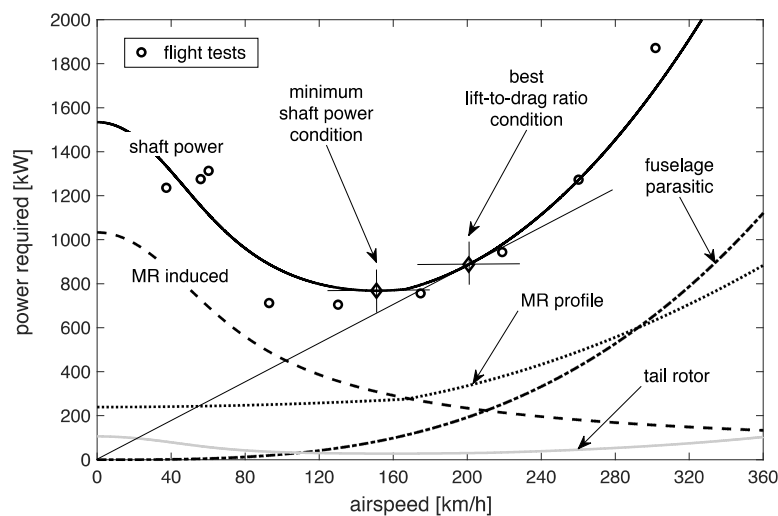


Figure 4.14: Helicopter power estimation and different contributions [35], [36], [37].

Neglecting the small contribution of the tail rotor and of the profile power due to the assumptions made before, being the parasitic fuselage power required equally divided to all the rotors in the configuration, it can be seen that the only contribution capable to shift the point of minimum power is the induced power of the rotor.

The induced power of the rotors is strongly dependent on the inflow distribution, and as previously discussed in Fig.4.13, the presence of a strong inflow into the rear rotors results in an increase in the induced power and a consequent shift to higher speeds for the minimum power point, as has been previously observed.

The discrepancy between the two power curves is ultimately attributable to the necessity for the aft rotors to produce a greater thrust in order to counteract the pitch-up moment. This results in an increase in torque and, consequently, the magnitude of the required power. However, this discrepancy is expected to diminish as the frontal speed decreases, allowing the two curves to converge and merge to a single value in hover condition.

Chapter 5

Phase Synchronization Effects on Flight Mechanics

This section examines the impact of phase synchronization on flight mechanics, including a preliminary investigation into the aerodynamic interaction between synchronized rotors.

5.1 Thrust Variation due to Phase Synchronization

5.1.1 Hover

In light of the aforementioned trim results, it is essential to provide a physical explanation of the reasoning behind the six rotor control variables asymmetries observed during the hovering flight in SubCh.4.6.

In order to achieve this, a UPM simulation in hover without a trimming procedure was conducted in parallel with a single rotor simulation. This was done in order to evaluate the underlying physics of the mutual interaction between rotors.

First of all, an examination of the single rotor computation in Fig. 5.1 reveals that the thrust distribution is perfectly azimuthal independent, with a peak zone around 75% of the total radius and a subsequent decrease due to tip losses, as would be expected.

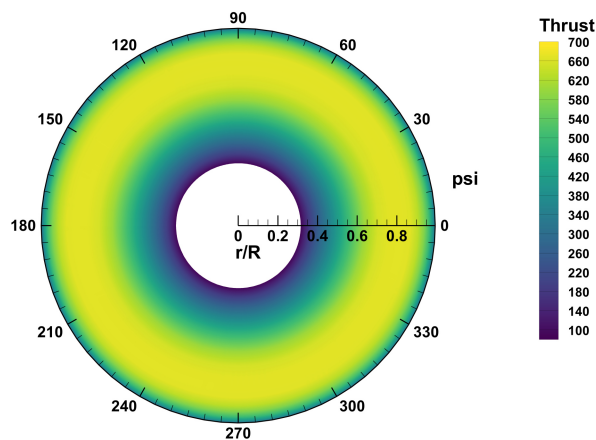


Figure 5.1: Single rotor thrust distribution in the rotor disc.

In this context, ψ represents the azimuthal coordinate of the rotor disc, which, in the present case, is defined to be rotating in a counterclockwise direction. The range of values for ψ is therefore from 0 to 360 in the aforementioned sense of rotation (for more details regarding the azimuthal conventions refer to Nomenclature and Conventions).

Fig. 5.2 instead provides a qualitative representation of the mutual interference between rotors. It can be observed that the thrust distribution is not identical for each rotor, but exhibits slight differences.

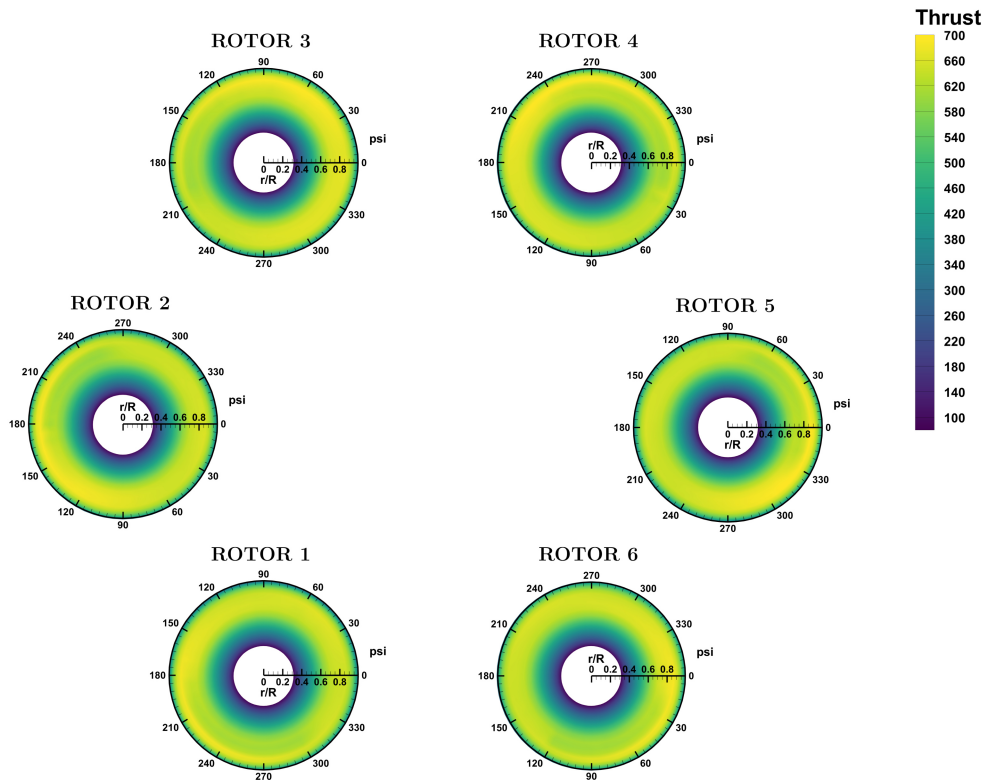


Figure 5.2: Spatial thrust distribution in the 6 rotor case.

In the end, a comparison of the two figures reveals that, due to the influence of mutual aerodynamic interaction, the thrust distribution is not perfectly rotational symmetric, exhibiting a number of peaks. The magnitude difference of these peaks can result in a discrepancy in the average integrated thrust for each rotor.

In order to better understand the physical phenomena, it is essential to shift the focus of analysis to the thrust time history. In Figs. 5.3 are reported the thrust behaviours of the four rotors and six rotors configurations without trim. In this context ψ is expressed as a decimal number of rotation but physically it keeps the same meaning (see Nomenclature and Conventions). So, each line (ROT1, ROT2, ...) represents the i -th rotor thrust integrated along the two blades versus ψ which is a time measurement expressed in decimals of the rotor revolution (in this case the 8th revolution).

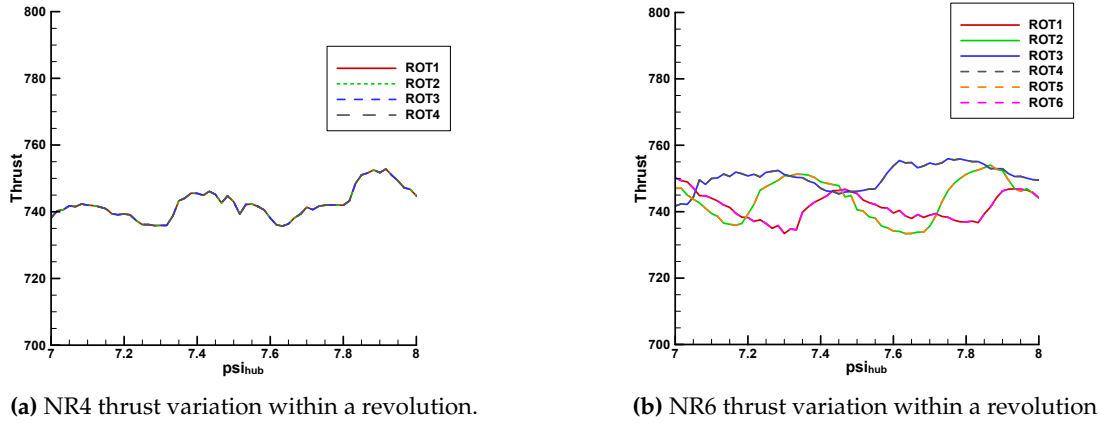


Figure 5.3: Thrust comparison for different configurations.

As indicated in Fig. 5.3 the aforementioned statements can be validated.

In the 4 rotors configuration (Fig. 5.3a), the symmetry of the configuration ensures that all rotors encounter each other in the same configuration (tip to tip), resulting in a uniform thrust history across all rotors.

However, in the six-rotor configuration (Fig. 5.3b), the thrust differs for each rotor.

The average thrust values for each rotor during the indicated revolution are presented in Table 5.1 for reference. This table clearly highlights the thrust differences between the rotors, showing that rotors positioned symmetrically with respect to the x-z plane exhibit nearly identical thrust values, whereas asymmetry relative to the y-z plane results in significant variations in average thrust. Finally, it is noteworthy that similar discrepancies were also observed experimentally by Shao et al. in [38] for a two-rotor configuration.

Average thrust [N]	
ROTOR 1	7.4143e+02
ROTOR 2	7.4405e+02
ROTOR 3	7.5064e+02
ROTOR 4	7.5078e+02
ROTOR 5	7.4410e+02
ROTOR 6	7.4129e+02

Table 5.1: Rotors thrust averaged in a single rotation.

It is now possible to gain an easy understanding of the asymmetry of the control variables presented in table 4.2. In fact, this kind of asymmetric response is introduced by the trim script in order to compensate for the average thrust difference between the rotors.

It is crucial to emphasise that such asymmetry is accounted for by the 3DoF procedure, given that it is an asymmetry with respect to the y-axis.

In this case, the thrusts are almost coupled between the front, back, and middle rotors, creating a small pitch-down moment that can be counteracted by the trim script. If this is not the case, the aforementioned interactions will not be taken into account.

Consequently, an increase in the order of the trim script has been investigated in Chapter 5.2 in order to stabilize in the best way possible each kind of phase shift during the study.

5.1.2 Forward Flight

The objective of this paragraph is to examine the impact of phase synchronization on forward flight conditions.

With regard to the trim results presented in Tab.4.3 it is not possible to discern any differences between the various configurations. This is due to the fact that the front-aft asymmetry in the control variable is a consequence of the system's need to counteract the pitching moment generated by the flight condition (see SubCh.4.6.2). Furthermore, left-right asymmetries are not present in all the configurations due to the fact that the script has only three degrees of freedom, which is insufficient to counteract them.

So, in order to gain some physical insights, two distinct simulations were conducted using the same four-rotor configuration (NR4). Both the simulations have been trimmed using the control variables present in Tab.4.3 but one simulation has been conducted with zero phase shift between the rotors while the other an orthogonal phase shift between the rotors (phase vector: $\chi = [0, 90, 0, 90]$) has been applied. The meaning and the convention adopted for the phase vector are explicated in Nomenclature and Conventions.

In Figure 5.4 are reported the results of the aforementioned simulations. It is first important to note that the direction of flight is down and the TAS is 28.33 m/s as the previously cited test cases.

With regard to the distribution of thrust, it can be observed that for each rotor disc, a peak is present. For counterclockwise rotors 1 and 3, this peak is located on the left side, corresponding to the advancing blade with respect to the direction of motion. In contrast, for clockwise rotors 2 and 4, this peak is located on the right side, also corresponding to the advancing blade.

The occurrence of these peaks is consistent with the underlying physics of the system. They are a consequence of the increasing relative velocity that the blade encounters during its motion within the advancing zone and are not related to phase synchronization.

It can be observed that the peaks are not perfectly at $psi = 180$ (CCW) or $psi = 0$ (CW). This phenomenon has been the subject of study by Krebs et al. [39] and is not related to phase synchronization. Rather, it is dependent on the preceding blade wake field of velocity interaction with the follower blade. In particular, in forward flight, the wake is convected by the forward velocity resulting in a change of the inflow distribution.

The inflow will be lower in the front side of the rotor disc resulting in an increase of the local angle of attack and a consequent increase of the thrust. Conversely, the inflow will be higher at the back side, resulting in a local decrement of the thrust.

The asymmetric force distribution on the rotor discs introduces a pure moment about the rotor hubs. It should be noted that this moment contribution is also taken into account in the trim computation as it was mentioned in SubCh.4.6.2.

Regarding the peaks, they exhibit a discrepancy in magnitude between the front and back rotors. This phenomenon can be attributed to the variation in collective pitch between the two pairs of rotors, as illustrated in Tab.4.3. As expected the back rotors are pushing more and so the magnitude of the peaks is greater with respect to the front ones.

The same behaviour has also been found by Guan in [14] confirming the physical reasoning that has been done so far.

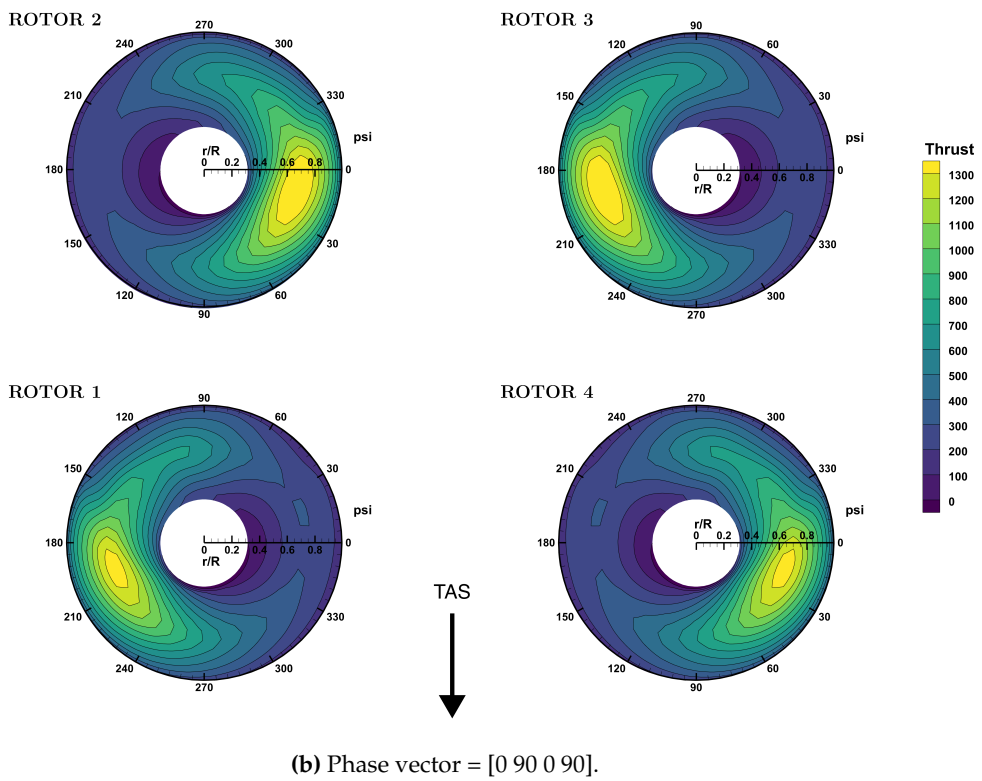
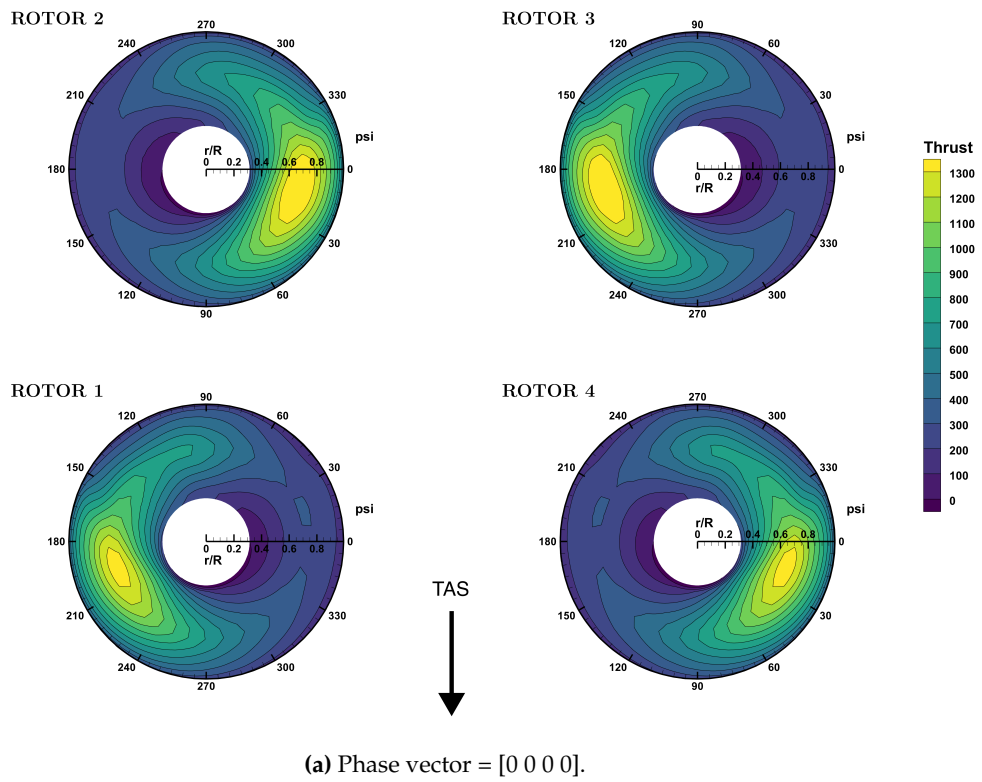


Figure 5.4: Thrust distribution comparison in forward flight condition.

Once the physics behind the results have been described in full, a comparison between Fig. 5.4a and Fig. 5.4b reveals no notable difference between the two, indicating that phase synchronization has a negligible impact on forward flight.

Further evidence that phase synchronization has no effect on forward flight can be found in Figure 5.5 below.

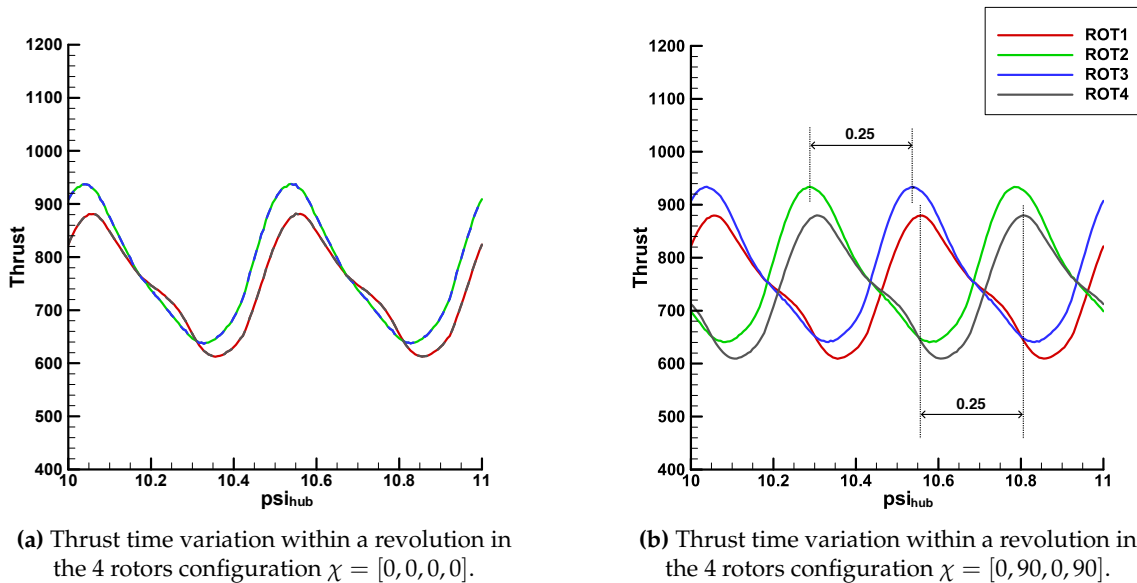


Figure 5.5: Thrust history comparison in forward flight.

In particular if it is assumed as a reference the plot Fig. 5.5a which depicts zero phase shift between the rotors, it can be observed that the introduction of a phase shift between the rotors results in a shift in the thrust behaviour of the same magnitude.

This effect can be observed in the right plot (Fig. 5.5b) in which a 90° phase shift between rotors 1 and 2, and 3 and 4, is commuted in a delay of magnitude $\psi = 0.25$, which corresponds to 1/4 of a revolution indeed 90°.

The reasons behind this shift are simply related to the "psi" definition. in the latter case, as reported in Nomenclature and Conventions this coordinate is fixed with the inertial frame and therefore begins with a value of zero in the y-direction. Consequently, the shifted rotors will exhibit the aforementioned peaks at a psi that is "delayed" by one quarter of a revolution (due to the fact that they are two-bladed rotors).

It is now important to note that, despite this delay or anticipation in the thrust history, which may be regarded as a periodical oscillation, integrating the two test cases along the entire revolution provides the same thrust as a confirmation of the results observed in Fig.5.4.

Finally, knowing that the trim script employs the forces integral along the surface within a single revolution it is possible to conclude that the presence of a phase shift in forward flight condition has no influence on the trim procedure.

In light of the aforementioned evidence, it can be assumed that the 3DoF trim procedure is an adequate and sufficient solution to ensure the stability of the system in forward flight condition.

5.2 6DoF UPM Trim Script

5.2.1 Introduction

Since aerodynamic interactions between the rotors have been found in hover condition, a new trim script with an increased number of degrees of freedom has been studied. This was done to take into account the thrust asymmetries of the left and right rotors that are present at some phase shift angles, although this type of effect is relatively very small.

In this section, the implementation of the 6DoF script and its results are presented to evaluate its performance

Theoretically, with more degrees of freedom the system can have more control over itself and therefore more control with respect to the thrust asymmetries that have been found. During the implementation of this script, the same philosophy and architecture of the 3DoF UPM one have been adopted (Ch.4).

The main differences are in the definition of the target forces and trim variables, with a consequent change in the mapping matrix, which is given below as a reference for the HALO configuration:

$$\text{MAPPING} = \begin{matrix} & x_1 & x_2 & x_3 & x_4 & x_5 & x_6 & & \\ \begin{bmatrix} 1 & -1 & -1 & -1 & 0 & 0 \\ 1 & 0 & -1 & 1 & 0 & 0 \\ 1 & 1 & -1 & -1 & 0 & 0 \\ 1 & 1 & 1 & 1 & 0 & 0 \\ 1 & 0 & 1 & -1 & 0 & 0 \\ 1 & -1 & 1 & 1 & 0 & 0 \\ 0 & 0 & 0 & 0 & -1 & 0 \\ 0 & 0 & 0 & 0 & 0 & 1 \end{bmatrix} & \theta_0^1 & \theta_0^2 & \theta_0^3 & \theta_0^4 & \theta_0^5 & \theta_0^6 & \Theta & \Phi \end{matrix} \quad (5.1)$$

$$\vec{y} = \begin{bmatrix} y1 \\ y2 \\ y3 \\ y4 \\ y5 \\ y6 \end{bmatrix} = \begin{bmatrix} F_x \\ F_y \\ F_z \\ M_x \\ M_y \\ M_z \end{bmatrix} \quad (5.2)$$

The only difference in the control variables is the presence of the roll angle Φ , but now, the trim variables vector \vec{x} and the trim forces vector \vec{x} are of dimension 6.

So, as expected, the increase in degrees of freedom is reported in the trim script as an increase in the dimension of the trim vectors.

This kind of modification is not cost free, in fact, increasing the order of the system will also increase the dimension of the Jacobi matrix \mathbf{J} from $[3 \times 3]$ to $[6 \times 6]$, leading to a corresponding increase in the time needed to compute it.

This factor is crucial because the calculation of the Jacobi matrix is the heaviest part of the script, and it has been found that the total calculation time of this type of script is almost double the previous one.

Nevertheless, complete control over the mechanics of the system has now been achieved.

In the end, it is important to note that, as before, the selection of the mapping matrix is not unique and so further studies can be carried out to evaluate the optimal one according to specific needs.

5.2.2 Test and Results Comparison with 3DoF

To evaluate the new trim script, two simulations were performed only for the hover case of the NR4 configuration, since, as reported in SubCh.5.1.2, negligible effects of phase synchronization are expected in the forward flight condition.

For the hover case 2 phase vector (χ) were adopted: [0 -45 0 -45] and [0 90 0 90]. The main results are reported below while all details are reported in Appendix B.

	[0 -45 0 -45]	[0 90 0 90]
Control Variables: $[\theta_0^1, \dots, \theta_0^n, \Theta]^\circ$	[18.527, 18.527, 18.527, 18.527, 0]	[18.490, 18.490, 18.490, 18.490, 0]
Abs_error: $[F_x, F_y, F_z, M_x, M_y, M_z]$	[6.502e-12, 3.310e-14 ,8.848, 2.273e-13, 1.591e-12, 7.356e-2]	[5.131e-13, 1.664e-13 ,8.929, 2.273e-13, 6.593e-12, 1.349]
Residual translation acceleration	2.9493e-03	2.976e-03
Residual rotational acceleration	1.2587e-04	2.0309e-02

Table 5.2: Hover Condition 3DoF.

	[0 -45 0 -45]	[0 90 0 90]
Control Variables: $[\theta_0^1, \dots, \theta_0^n, \Theta, \Phi]^\circ$	[18.468, 18.532, 18.468, 18.532, 0, 0]	[18.456, 18.563, 18.456, 18.563, 0, 0]
abs_error: $[F_x, F_y, F_z, M_x, M_y, M_z]$	[3.424e-13, 2.094e-13, 3.205, 2.273e-13, 1.1367e-12, 1.2877]	[8.978e-14, 7.570e-13, 1.070e+01, 3.362e-10, 0.000, 6.903e-01]
Residual translation acceleration	1.068e-02	3.568e-02
Residual rotational acceleration	2.203e-03	1.181e-03

Table 5.3: Hover Condition 6DoF.

The first thing to note is that in both cases the 6DoF has an asymmetry in the collective angles. As we have seen in the previous paragraphs, this is due to the interaction between the synchronised propellers.

The trim efficiency between the two algorithms is almost the same in all cases. In particular, all test cases meet the trim success criteria, confirming that both algorithms can be used in future studies.

To better evaluate the effects of the new trim scripts, 2 different UPM simulations were run with the control variables from the 3DoF and 6DoF trims inserted.

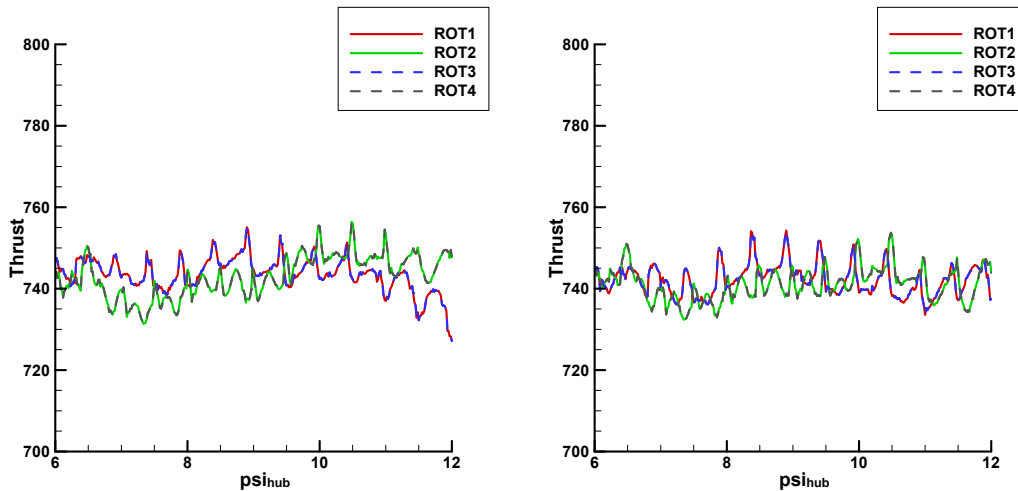


Figure 5.6: Hover trim comparison $\chi = [0 -45 0 -45]$, 3DoF to the left and 6DoF to the right.

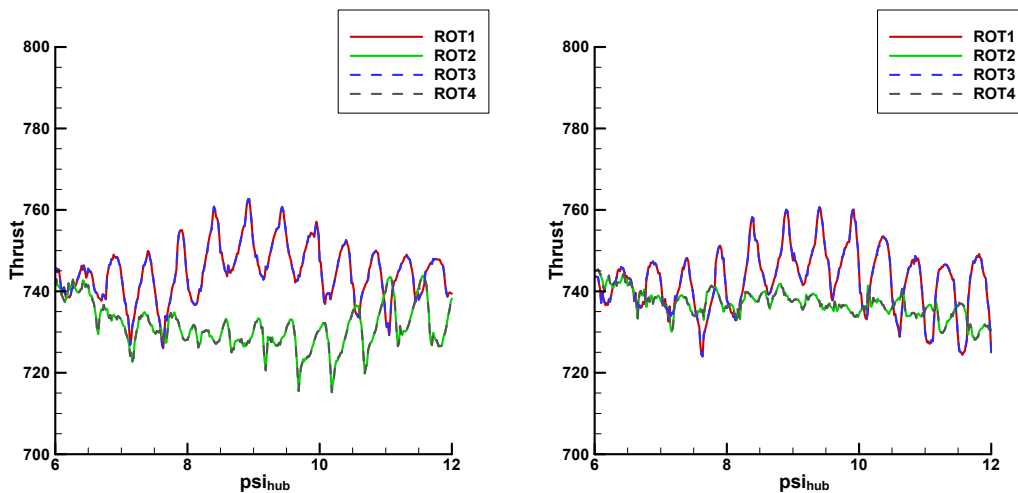


Figure 5.7: Hover trim comparison $\chi = [0 90 0 90]$, 3DoF to the left and 6DoF to the right.

From Figs. 5.7, 5.6 it is possible to have an estimation of the difference between the two approaches. In particular it is possible to see that the 6DoF (figures on the right side) tends to bring the thrusts to the same level demonstrating that increasing the order of the trim procedure is effective.

In fact, bringing the two oscillations closer together will result in a similar average thrust between the rotors.

The last analysis carried out in hover is the aeroacoustic one. In particular, from the last revolution of the simulations mentioned above, using APSIM (see.2.3), it was also possible to make the noise pattern in a hemisphere, of 14.5 meters of radius, around the configuration.

This type of analysis was carried out in order to assess if the trim procedure typology could affect the overall Sound Pressure Level (SPL[dB]).

Figures 5.8, 5.9 show the results of the APSIM simulation, all polar plots are slices of the hemisphere cut at different elevation angles, phi represents the azimuthal spatial coordinate of the hemisphere. More information about the azimuthal convention can be found in Nomenclature and Conventions.

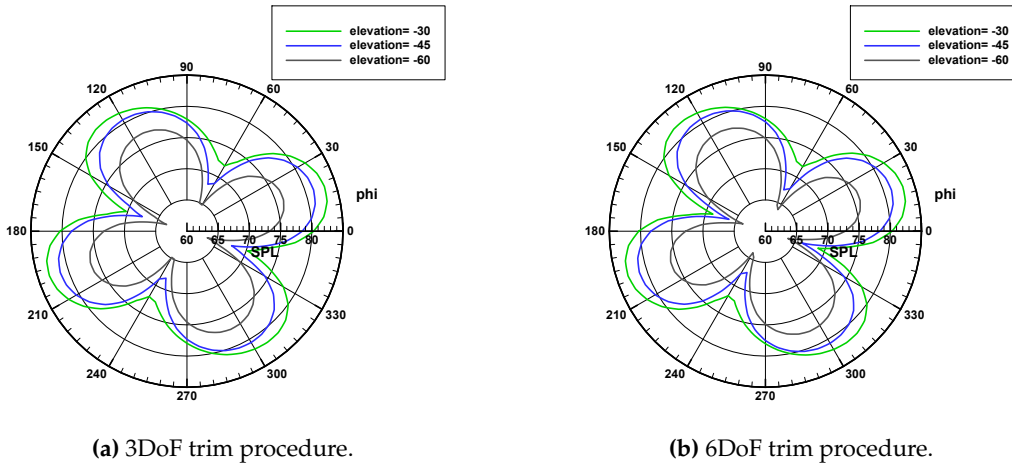


Figure 5.8: Acoustic comparison for different trim procedure, $\chi = [0 -45 0 -45]$.

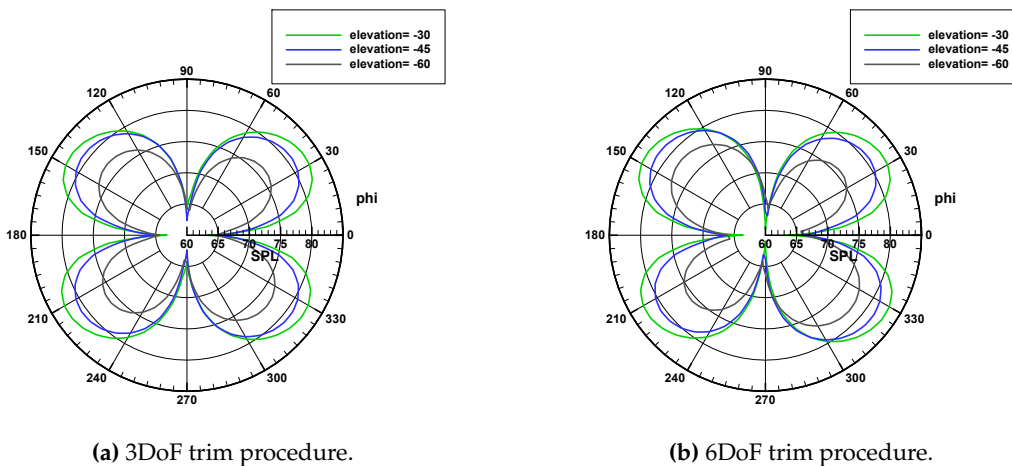


Figure 5.9: Acoustic comparison for different trim procedure, $\chi = [0 90 0 90]$.

From the images above, it is possible to note that no directivity pattern is affected by the trim procedure typology.

In the same way it is possible to verify that the magnitude of the lobes it is affected in a minimal way having generically that the 6DoF control variables leads to slightly lower minimum in both configurations (Figs. 5.9b, 5.8b).

This can be explained by the fact that if the rotors have almost the same thrust, then the acoustic sources of each rotor will be almost the same, and so the disruptive interference between all the sound waves coming from the rotors will be greater.

In any case this effect is really very small compared to the overall scale of the problem and a more comprehensive analysis of this phenomenon will be needed in order to have a better understanding.

This interpretation is left as a suggestion for future studies.

In conclusion the 6DoF trim script has produced overall good results, the differences with 3DoF are minimal but physically more coherent with the dynamics of the system. For this reason it has been included in the simulation chain presented in Chapter 6 to be sure that the system will be able to converge to a trim solution despite the phase shift vector.

Finally, the introduction of this new trim script opens up the possibility for future research to study a wider typology of manoeuvres.

Chapter 6

NOISE-Chain: Numerical Optimization of In-flight Sound Emissions tool-Chain

6.1 Introduction

This chapter presents the core of the project, which aims to assess the potential for noise reduction through phase shift variation of synchronized rotors. In this context, a significant number of cross-references will be included in order to facilitate the integration of the work and research conducted by all individuals involved in the research project [7, 8].

In order to investigate the potential viability of the concept, a numerical toolchain has been developed. The script's objective is to optimize and numerically simulate the noise pattern in a specified region of the domain.

Figure 6.1 depicts the schematic architecture of the toolchain (NOISE-Chain).

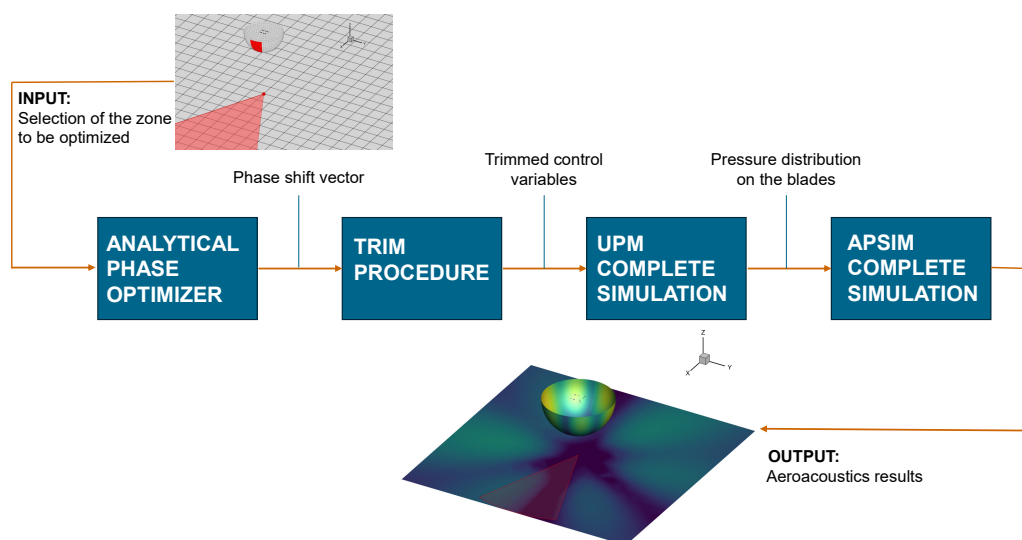


Figure 6.1: NOISE-Chain simplified structure.

The script takes in input the geometry of the multicopter, the simulation parameters, the domain definition, the environmental conditions and most importantly the region in which noise reduction is required.

The first step of the chain, namely the analytical phase optimizer, was developed by Chella in his thesis [7].

In summary, this block utilises an analytical replication of the rotor noise sources within a Genetic Algorithm to identify the optimal phase vector χ to be used for the numerical computations.

For further details regarding this initial block, please consult [7].

The second block of the chain consists of the aforementioned trim script, which has been the subject of previous chapters.

The objective of this block is to trim the selected configuration with the desired phase shift vector and desired flight conditions, and to output the control variables required to stabilize the system.

Once stability has been established, the third block inserts the control variables and performs a complete UPM simulation with a smaller step size of 6 and 12 revolutions.

It is crucial to note that the remaining UPM parameters are maintained consistent with those utilized in the trim computation, thereby ensuring the replication of the same physical scenario.

The UPM computation outputs the so-called "press_apsim-it-n-.tec" (see 2.2, [23]) for the last revolution. These outputs represent the pressure distribution along the blades, which is required by the APSIM code (see 2.3, [25]) for the aeroacoustic simulations in the final block.

In the latter as anticipated a complete aeroacoustic simulation is conducted within the specified input domain and under the selected environmental and flight conditions.

Finally at the end of the chain are reported all the aeroacoustic results that will be discussed in depth later on in this chapter.

This thesis presents the results of the chain only in hover condition, but it should be noted that such toolchain can also be used in forward flight by exchanging the first block.

This kind of analysis has been conducted by Sessini in [8] and is based on a numerical optimizer instead of the analytical one proposed here.

6.2 Hover Optimization

In the near future, one of the most challenging aspects of the Urban Air Mobility era will be the social acceptance of these multicopter aircraft in terms of their aeroacoustic impact. Given that these new VTOL configurations are designed to operate in hover or at low speeds in urban environments, it is crucial to optimize the acoustic footprint in the ground during such flight conditions.

For this reason an optimization in hover condition has been conducted with all the aforementioned configurations.

In order to create a realistic scenario, it has been decided to focus the hover optimization at an altitude of 25 m above the ground and within a range of 100 m^2 , in accordance with the EASA guidelines for the new VTOL generation on environmental protection [40]. The computational domain resulting from the aforementioned considerations is illustrated below in Figure 6.2.

Furthermore, in order to facilitate the analysis of sound propagation around the aforementioned configuration, it was decided to incorporate an hemisphere of radius 14.5 m into the domain.

This additional geometry will allow for a more comprehensive examination of the noise propagation characteristics around the selected configurations.

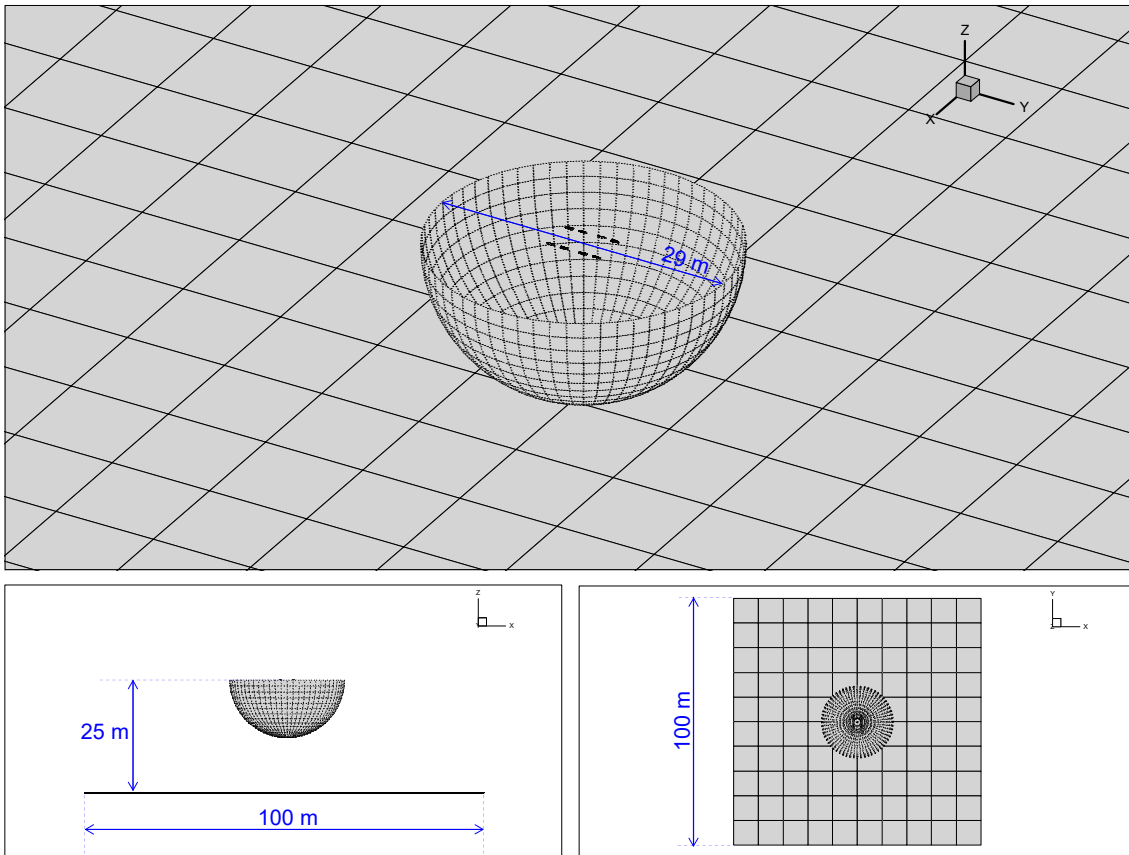


Figure 6.2: NOISE-Chain computational domain description.

In regard to the optimisation process, two strategies have been employed: a Hemisphere and a Ground optimization.

The former, illustrated in Figure 6.3a, is a quasi 1-D optimization. It consists of a pure azimuthal optimization within the hemisphere that surrounds the configuration. The elevation selected for this kind of optimization is -45 deg .

The second typology of optimization instead consists in the selection of a 2-D portion of ground to be optimized and it is reported as a reference in Figure 6.3b.

The computational aspects of these optimizations are documented in Chella's thesis [7] as the only block affected by this selection is the first in the chain.

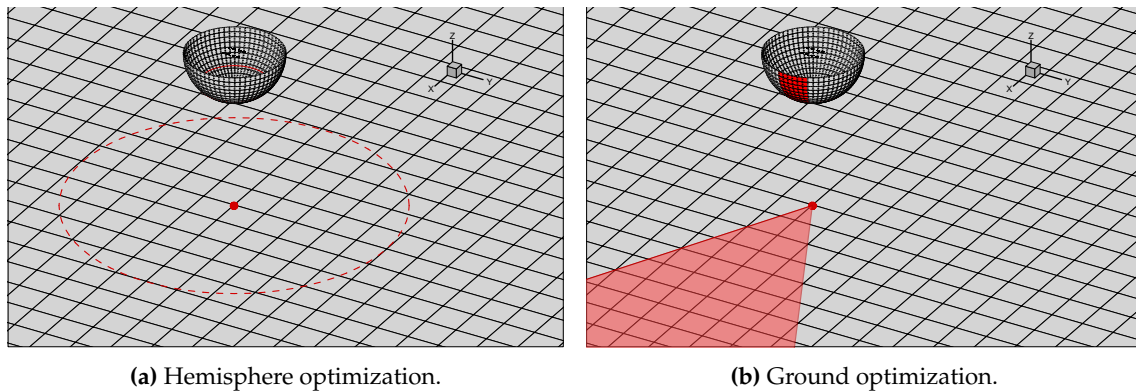


Figure 6.3: Optimization scenarios.

6.3 Results

All the complete results for all the configurations are presented in Appendix C. In this paragraph, only some cases from the HALO configuration (six rotors) results are discussed in order to avoid unnecessary repetitions.

First of all it is necessary to do a comparison between the two optimization methods. In particular, starting from the Hemisphere optimization, as illustrated in Figure 6.4a, it can be seen that the desired hemisphere region (black grid) has been optimized in accordance with the user's specifications. However, upon closer examination of the ground SPL footprint (Fig. 6.4b), it becomes evident that this particular optimization has a comparatively limited impact. In fact, the red section, which represents the projection of the hemisphere azimuthal range, does not correspond to a noise minimum region.

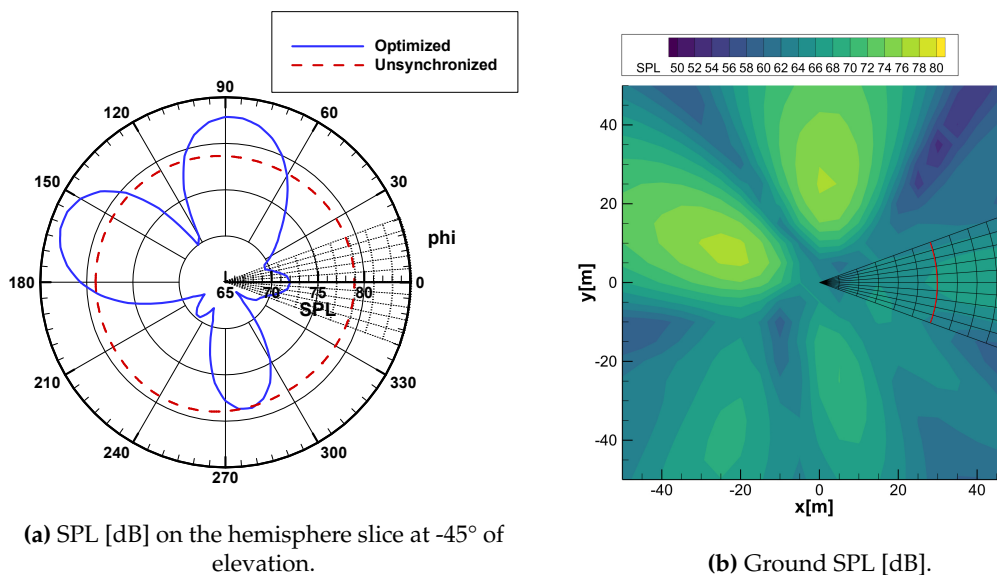


Figure 6.4: Hemisphere optimization results for the azimuthal range $[-20^\circ, 20^\circ]$, $\chi = [0, 37, -28, -25, -32, -5]$.

Now, looking at the Ground optimization in Figure 6.5b it is possible to appreciate that the reference ground region has been optimized as requested by the user.

Additionally, the SPL directionality on the hemisphere slice (Figure 6.5a) is optimized in the projection of the ground region into the hemisphere. This latter point is crucial, as it demonstrates that when a ground optimisation is selected, the hemisphere also yields beneficial results, contrary to what was observed previously in Figure 6.4.

This behaviour has been noticed in the majority of the simulations presented in Appendix C, and thus it can be concluded that the ground optimization is the most effective method for optimizing the directionality of multirotor noise emissions.

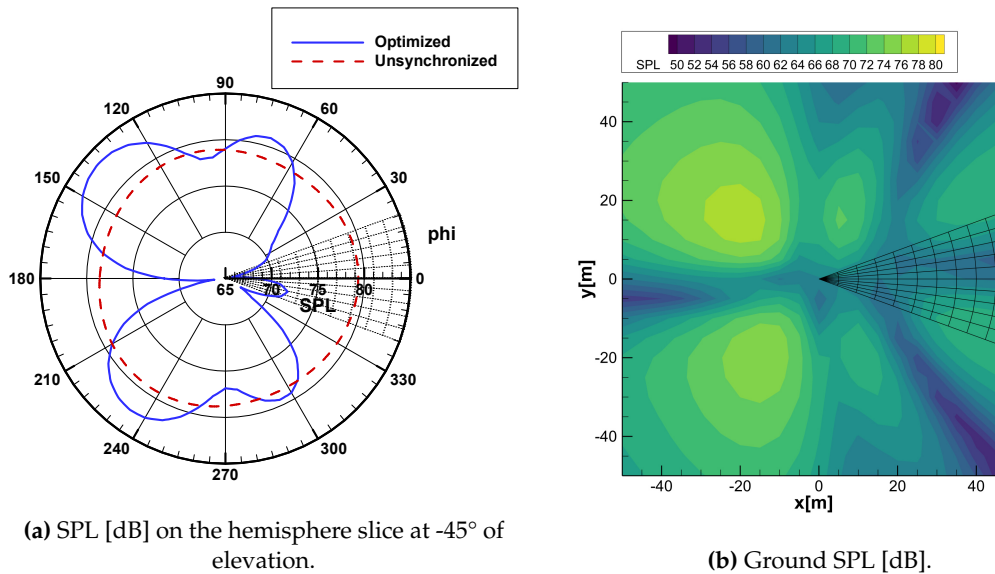


Figure 6.5: Ground optimization results for the azimuthal range $[-20^\circ, 20^\circ]$, $\chi = [0, 40, -41, 34, -42, 70]$.

Ultimately, it can be observed that the phase shift vectors (χ) are distinct between the two typologies of optimization, thereby demonstrating that the phase optimization process is inherently complex and lacks a unique solution.

Once the optimization methods have been outlined and compared, the results are presented in Figure 6.6, which depicts the entire domain, optimized region by region, for the HALO configuration.

The figures illustrate an upper visualisation of the entire domain (hemisphere and ground) with the optimized region (depicted in a black grid) varying for the nine simulations in order to cover all the ground.

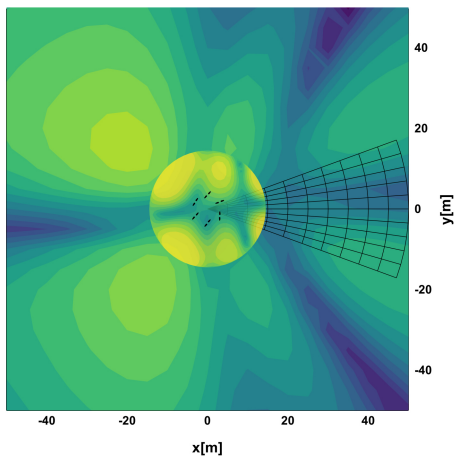
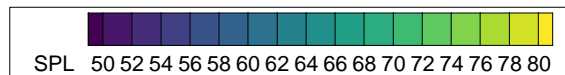
The initial position of the blades in the configuration is also reported in all the pictures, which allows for an immediate visualization of the phase shift to be appreciated.

The central circle present in all the figures represents the 2D top view of the hemisphere. Consequently, the SPL magnitude is higher simply because the hemisphere is located closer to the configuration with respect the ground plane. It can therefore be seen that the optimization process has an effect on both the ground and the hemisphere, as previously discussed.

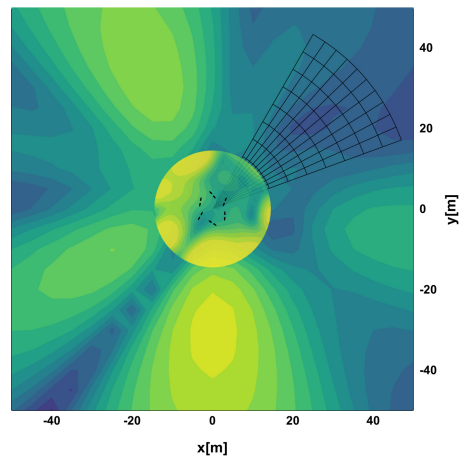
It is evident that noise directivity optimization is feasible for all domain subregions, although the resulting outcomes may vary. The discrepancy between the various optimized zones can be attributed to the intrinsic characteristics of the system, particularly the presence of geometric constraints. These constraints limit the potential for acoustic wave disruptive interference in certain points of the domain, thereby influencing the overall outcome.

The number of rotors also affects this factor. As can be seen in Appendix C, different configurations yield different patterns for the same directional optimization.

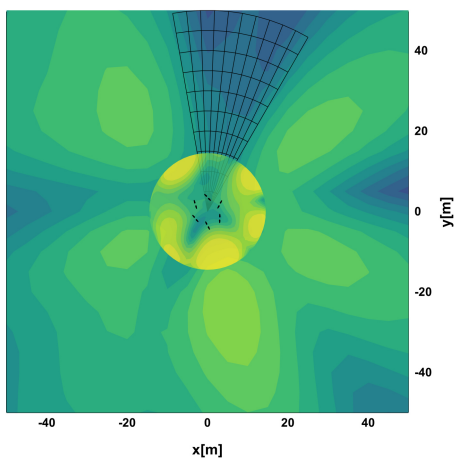
Nevertheless, it can be confirmed that optimal results were obtained for all configurations.



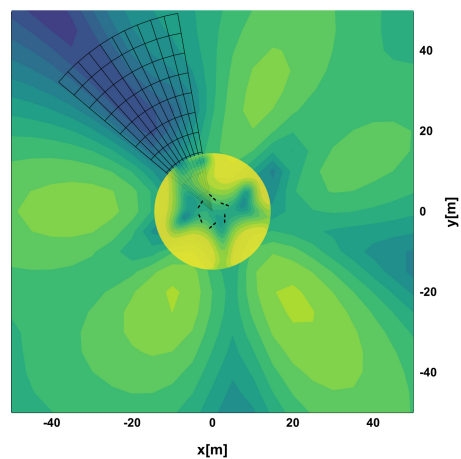
ZONE 1



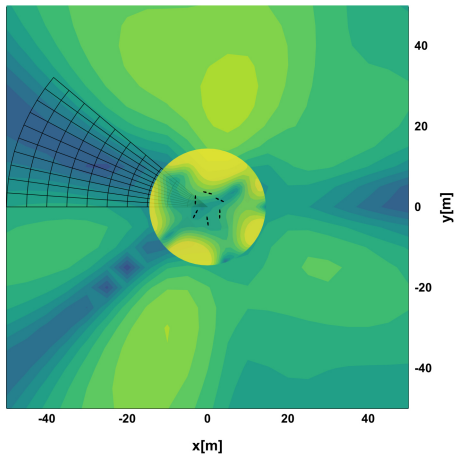
ZONE 2



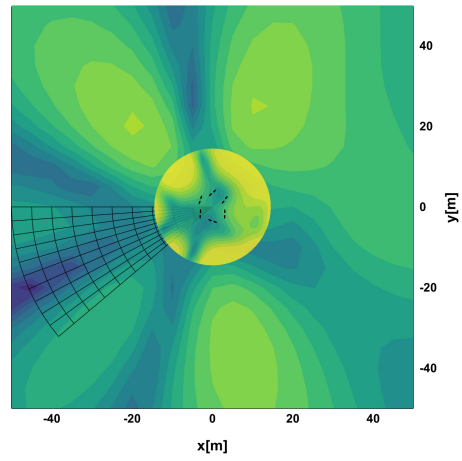
ZONE 3



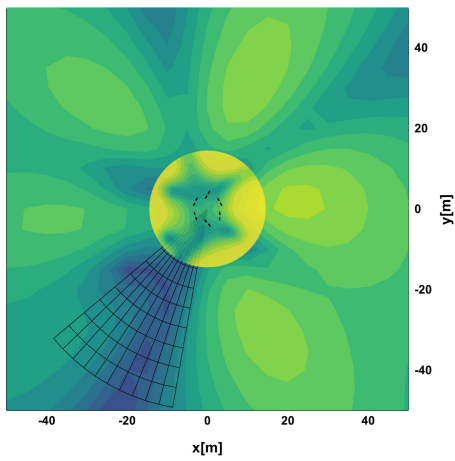
ZONE 4



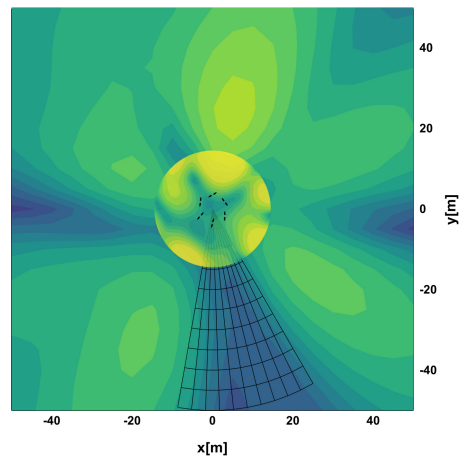
ZONE 5



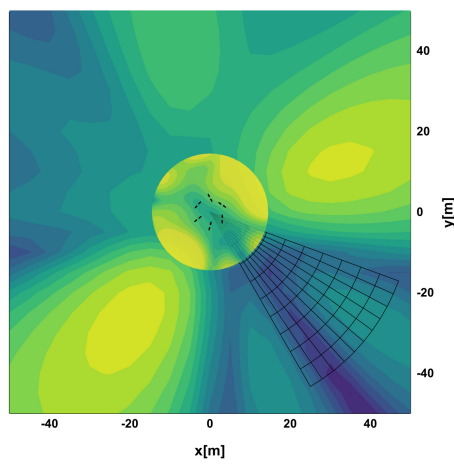
ZONE 6



ZONE 7



ZONE 8



ZONE 9

Figure 6.6: SPL [dB] distribution in the domain for the HALO configuration, Ground optimization.

Ultimately, it can be stated that the project's scope has been achieved. The objective of noise local reduction through phase synchronization can be directly visualized by comparing Figure 6.6 with the unsynchronized footprint that would be present in a normal situation (Figure 6.7).

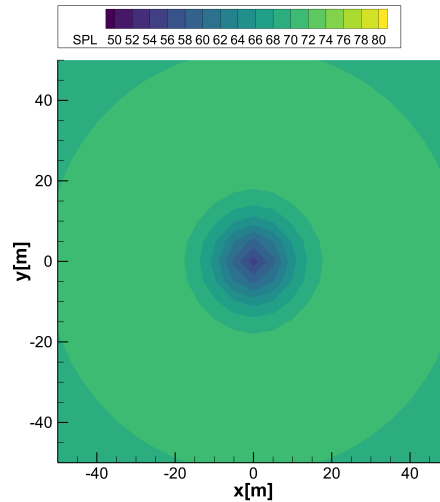


Figure 6.7: Unsynchronized ground SPL [dB].

Figure 6.7 has been obtained with a dedicated script that takes the pressure results of the rotors in the configurations and sums these pressure values in the frequency domain. This is done in order to lose all the time information. In this way, the acoustic interaction is neglected, and a similar unsynchronised pattern is found.

This proposed method is a simplified model, and therefore does not perfectly replicate the unsynchronised behaviour, due to the fact that the aerodynamic interactions are not neglected. Consequently, the patterns present in the hemisphere slices in Appendix C may not be perfectly azimuthal symmetrical. However, they represent an optimal reference for the unsynchronised case.

Region	Mean	Maximum	Minimum	Zone mean
ZONE 1	67.449	77.053	49.393	63.419
ZONE 2	66.655	79.013	53.705	59.748
ZONE 3	68.478	75.852	57.116	61.707
ZONE 4	69.679	76.354	54.595	60.358
ZONE 5	69.117	77.035	56.376	61.535
ZONE 6	68.865	76.324	52.428	62.878
ZONE 7	69.308	76.705	56.600	60.710
ZONE 8	68.073	76.970	55.150	60.055
ZONE 9	68.078	79.324	51.861	60.895
UNSYNCHRONIZED	70.315	71.945	54.981	70.315

Table 6.1: SPL [dB] ground results.

Table 6.1 provides a qualitative evaluation of the ground SPL optimization.

Firstly, in the second column it can be observed that the SPL mean value on the entire ground domain is always below that of the unsynchronized one.

This is significant because it demonstrates that the directional optimization maintains the overall mean value of sound emission at the same level as that of the classical unsynchronized rotors.

Further studies on the overall sound power effects of the phase shift optimization are recommended for future investigation.

With regard to the minimum value, it can be observed that a reduction in noise levels of approximately 15 dB is achievable. It is also noteworthy that, although the selected region is consistently minimized, there are cases where the minimum SPL of the domain is not within the optimized region.

This is due to the fact that, of course, the objective of the minimization is to reduce the integral SPL distribution in the selected area, rather than focusing on a single point within the domain.

The results suggest that a reduction in the size of the region to be minimized may result in a greater overall reduction in the same region. This is a recommendation for future studies, along with the dependence of the minimization region on the position of the rotors within the multirotor.

In the final column, an evaluation of the mean SPL value within the specified zone can be observed. This is the most significant outcome of the minimization process, as it demonstrates that a reduction of approximately 10 dB can be achieved with the aforementioned toolchain. This is a highly advantageous result, as it is a cost-effective solution that does not require additional devices or an increase in weight or power consumption.

Finally, it is also noteworthy that Figure 6.6 depicts the presence of noise augmentation in certain regions. These are of particular significance, indeed, as can be seen in Tab. 6.1 the SPL augmentation maximum is in the order of 10 dB.

Of course, it is essential to consider this fact when examining the practicality of phase shift optimization in real-world scenarios.

This aspect of the study represents one of the most significant challenges associated with such optimization technique.

One potential solution is the development of an in-flight phase controller that can adjust the phase shift during flight, modifying the noise reduction region in accordance with the target's movement to ensure it remains within the optimal noise region at all times.

This kind of controller is proposed as a potential direction for future studies. In summary, a controller of this nature could be operated using the free RPM control channels, modifying the phase shift vector χ with a slight instantaneous acceleration or deceleration of the rotor's rotational speed.

Chapter 7

Nonlinear Flight Dynamics Model

7.1 Introduction and Tuning

This chapter presents a nonlinear flight dynamics model for the HALO configuration (six rotors configuration).

The model has been developed in Matlab/Simulink following the lecture notes of the Unmanned Systems course held by professor de Angelis [36], [41].

This model has multiple applications. Initially, it was employed to facilitate a more straightforward comprehension of the underlying physical phenomena by comparing the flight mechanics results of the preceding chapters with an analytical reasoning. Secondly, it was adapted for a fast trim evaluation, and then utilised by Sessini [8] to develop a fast tool for noise prediction without aerodynamic interferences. Finally, it was employed to conduct a preliminary study into the performance evaluation of the collective pitch-controlled VTOL.

In the script, the aerodynamic loads are evaluated using the mathematical model proposed by Talbot in [34]. The dynamic model is then controlled with a closed loop control system inspired by the Pixhawk system reported in [42].

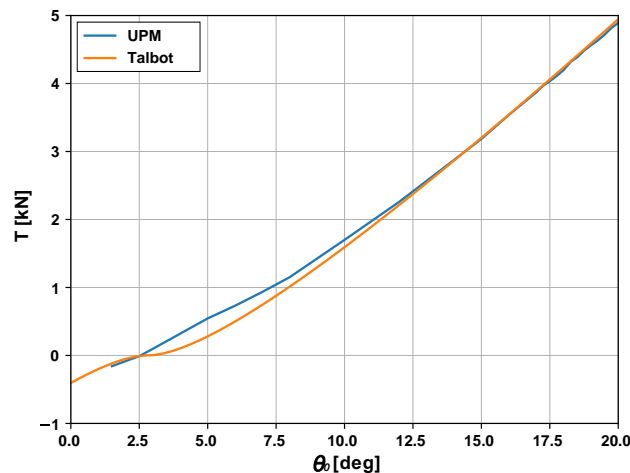


Figure 7.1: Thrust versus collective pitch (θ_0) comparison.

The geometric parameters, the fuselage drag model and the inertia model are the same as those of the aforementioned HALO, thus enabling a coherent comparison between the numerical and analytical models.

In particular, the aerodynamic coefficients inserted into the analytical tool have been calibrated to replicate the same polar thrust obtained with the UPM computation. This was achieved with sufficient precision, as demonstrated in Figure 7.1. It is noteworthy that in the operational range of the configuration ($\theta_0 = [15, 20]$), the two curves are nearly identical, while some discrepancies are evident at lower pitch angles. This discrepancy is not a result of an inadequate analytical modelling of the aerodynamic loads, but can be assumed as a consequence of the inherent limitations of the UPM computation at low collective angles. As observed in SubCh.4.5.1, the UPM computation is susceptible to uncertainties due to the significant influence of the wake near the rotors. Nevertheless, as previously noted, this region is of secondary importance, given that the collective pitch value of the rotors remains within the range of 10° to 20° across all flight conditions.

7.2 Power Analysis

In this section a preliminary study on the performance of the HALO configuration is reported.

After the tuning of the analytical model, a power estimation has been done comparing the results from UPM with the ones of the Simulink model. Figure 7.2 presents the estimated power of the models under consideration.

Recalling that UPM is a potential method, it is not possible to have an accurate estimation of the friction loads acting on the blade. Despite this, there exist some implemented methods for boundary layer and friction evaluation along the blade, but these are not considered in this study.

Instead, with regard to the analytical model, the equivalent profile drag coefficient estimation derived from the Talbot manual is based on the classical parabolic formulation with the angle of attack (see [31]):

$$\overline{Cd} = Cd_0 + k\overline{Cl}^2 \quad (7.1)$$

With:

- \overline{Cd} : equivalent profile drag coefficient (average over the blade and over the azimuth).
- \overline{Cl} : equivalent profile lift coefficient.
- Cd_0 : constant term accounting for profile parasite drag.

Or equivalently:

$$\overline{Cd} = 0.009 + \frac{0.3}{C_{l\alpha}^2} \left(\frac{6C_T}{\sigma} \right)^2 \quad (7.2)$$

Indeed, assuming the following:

- Uniform inflow.
- $\mu = 0$, hover condition.
- Constant aerodynamic properties over the blade.
- Linear twist of the blades.
- Constant coefficients with Reynolds number (Re).

The term $(6C_T/C_{l\alpha}\sigma)$ in Eq. 7.2 is approximately equal to an averaged equivalent rotor blade angle of attack.

This drag model represents a traditional approach to power estimation for a conventional helicopter configuration and it is illustrated in Fig.7.2 as "Talbot".

With regard to multirotor configurations, it is possible to make some refinements in how the profile drag is described, as outlined in reference [43]. In particular, the assumption of Cd_0 independence from Reynolds number can be relaxed.

In order to do so, a flat plate analogy is adopted and a semi-empirical solution for turbulent flow friction over a flat plate is adopted.

The parasite drag contribution is therefore given by:

$$Cd_0 = 2 \cdot Cf = 2 \cdot 0.059Re^{-0.2} \quad (7.3)$$

leading to:

$$\overline{Cd} = 2 \cdot 0.059Re_{75}^{-0.2} + \frac{0.3}{C_{l\alpha}^2} \left[\frac{6C_T}{\sigma \left(1 + \frac{3}{2}\mu^2\right)} \right]^2 \quad (7.4)$$

with:

$$Re_{75} = \frac{\rho \cdot CHORD_{75} V_{75}}{dyn_viscosity} \quad (7.5)$$

and

$$V_{75} = \sqrt{V_i^2 + (0.75 \cdot \Omega \cdot ROTOR)^2} \quad (7.6)$$

with:

- The subscript $_{75}$ indicates that the variable is evaluated in a position equivalent to 3/4 (75%) of the rotor radius.
- V_i is the induced velocity of the rotor.
- The contribution of the advance ratio μ is also considered.

As reference, the Reynolds number for this blade configuration is in the order of 10^6 .

In Figure 7.2 the latter model is indicated as "Talbot + correction".

For the remaining results of this chapter, the Reynolds dependent profile drag model is adopted for all power calculations.

In regard to the induced power, the analytical model estimates this as an ideal contribution multiplied by a correction factor ($k_{ind} = 1.35$), i.e. $k_{ind}TV_i$.

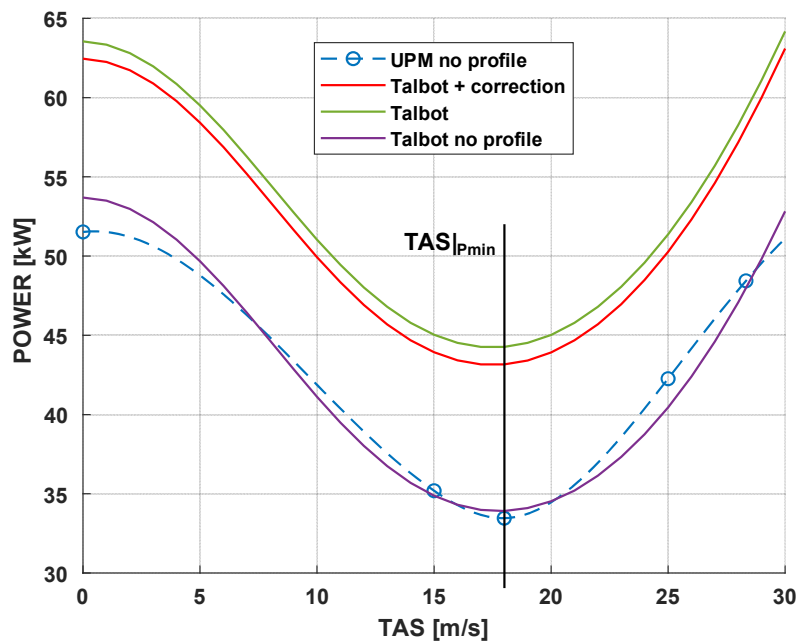


Figure 7.2: Required power versus forward speed for the HALO configuration.

Figure 7.2 illustrates the comparison between the UPM and the aforementioned models' power results.

The UPM results have been interpolated to facilitate a more comprehensive understanding of the power curve shape. Upon comparison, the curves exhibit a notable similarity in terms of shape and share the same minimum point.

In particular, it can be observed that the inviscid UPM and the Talbot model without friction are very similar in both magnitude and shape. This indicates that the analytical model, despite not accounting for mutual interactions between rotors, can effectively capture the underlying physics of the problem and serve as an optimal starting point for performance analysis.

The discrepancy between the UPM and the other analytical results is influenced by the profile drag modeling. In conclusion, in the absence of experimental data, it is not possible to determine a priori which drag model is more accurate in estimating the required power. Furthermore, the configuration under examination features a drone propeller geometry but with an unusual size, positioning itself between small drone applications and classical helicopter configurations.

7.3 Power Comparison

As previously stated, one of the primary distinctions between a variable pitch controlled drone and a classical RPM controlled one is the enhanced performance of the former. This is a topic that is currently attracting considerable interest, and it has been observed that variable collective-pitch rotors are more efficient in terms of energy consumption than comparable fixed-pitch rotors under similar operating conditions [17].

In this paragraph a preliminary analysis of this phenomenon is presented. Using the aforementioned Simulink model, a series of simulations have been conducted with a classical RPM actuation and a variable pitch one. Both controllers are architecturally similar and have been developed in accordance with [36, 41]. Finally, the controllers have been tuned using a trial-and-error procedure in order to obtain reliable results.

The results of the aforementioned simulations are presented in Figure 7.3.

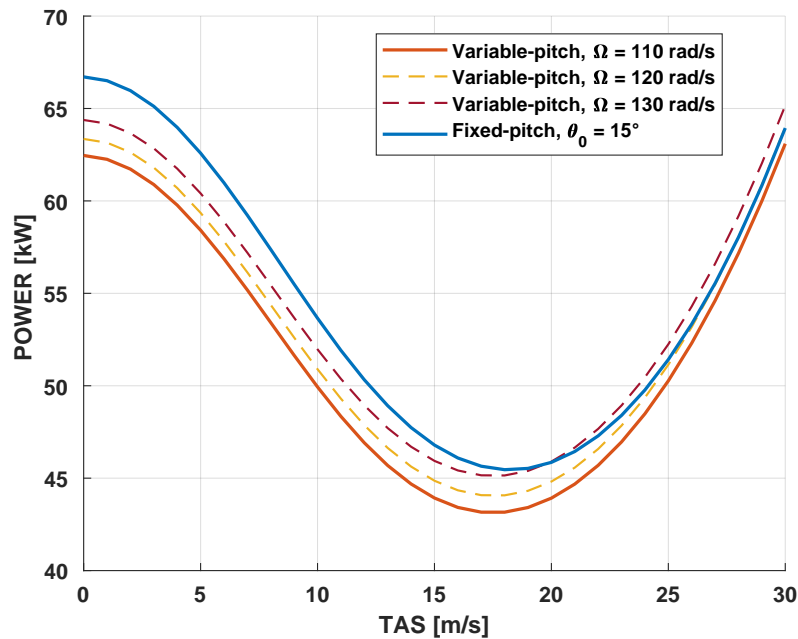


Figure 7.3: Required power for fixed and variable pitch actuators.

It is evident that the two types of actuation exhibit a discrepancy in their respective power curves. This discrepancy is not merely quantitative but also qualitative, manifesting in the shape of the curves themselves.

This fact is of great significance, as it demonstrates that the TAS of minimum power also varies between the two types of actuation.

The same behaviour has been observed in experimental studies conducted by McKay et al. [16], which confirms the reliability of the adopted model.

At last, a series of distinct constant rotor rotational speeds have been evaluated with the identical collective pitch controller. The objective of this analysis was to compare the effects of the former on the power behaviour of the system.

It can be observed that as the rotational speed Ω increase, the power curve translates, resulting in an overall increase in the required power of the configuration during all flight speeds.

This effect is of significant importance and must be considered during the design phase. Of course, It is not feasible to maintain a too low rotational speed, as this would prevent the multicopter from generating the necessary thrust to maintain flight.

This phenomenon is also significant from an aeroacoustic perspective, as a low rotational speed helps to maintain a contained tip Mach number.

Figure 7.3 demonstrates the assertion that an appropriate design procedure can result in a reduction in required power with a variable pitch controller in comparison to a fixed one.

A further suggestion for future research is the implementation of a hybrid optimal controller with the objective of achieving the minimum possible power for each flight condition. This would involve identifying the set of collective pitches and RPM for each rotor, with the dual aim of stabilizing the aircraft and minimising the required power.

Chapter 8

DUALO: DUAL rotor for Low-noise Operations

8.1 Introduction and Sizing

In the previous chapters, the focus was placed on the application of noise reduction through rotor phase shifting in configurations controlled by variable pitch propellers actuation.

Nevertheless, this is not the only method by which synchronization between rotors can be achieved. An alternative methodology employs the utilisation of only two rotors, equipped with cyclic and collective pitch control mechanisms. In this configuration, the controllability is maintained without the necessity for adjustments to the individual rotors rotational speeds (RPM). This allows for effective control of the aircraft while preserving rotor synchronization.

Historically, various rotorcraft configurations employing this type of actuation have been explored, demonstrating their applicability across a broad range of operational scenarios. Consequently, conducting a feasibility study on this type of configuration is of significant interest due to its potential versatility and operational benefits [21].

In this paragraph, the noise reduction via rotor phase shift is investigated within a side-by-side dual rotor configuration (NR2). The rotors in question are counter-rotating, with the left rotor in Fig. 8.1a rotating in a counterclockwise direction.

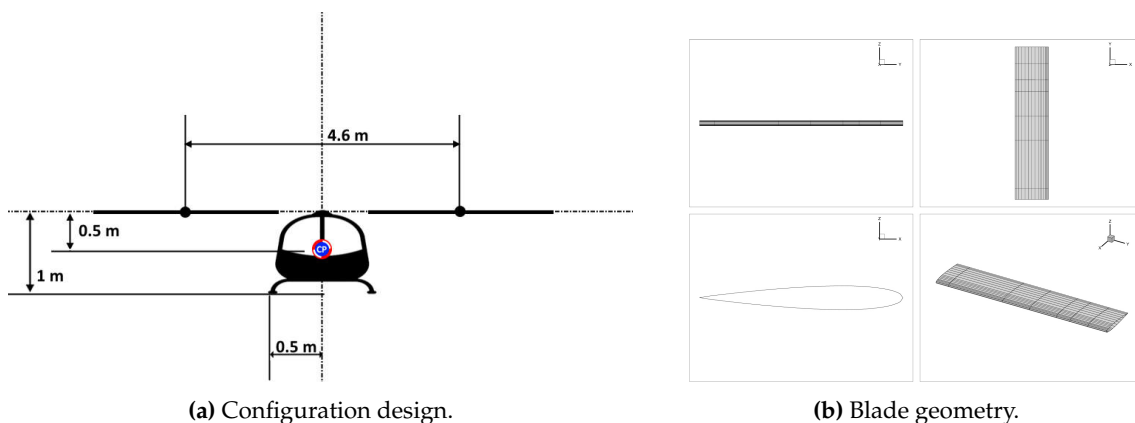


Figure 8.1: DUALO geometry and sizing.

The design process of the dual rotor configuration, illustrated in Figure 8.1, was based on a series of simplifying assumptions. These were made with the intention of reducing the complexity of the analysis and ensuring comparability with previous configurations. The goal was to establish a feasible aerodynamic and structural layout for a preliminary study.

The key assumptions made in this design are listed below:

- Two-bladed teetering (semi-rigid) rotors were selected, with no hinge offset, to simplify the simulation structure model and eliminate the transmission of pitch and roll moments to the shaft.
- The inertia and drag models of the configuration were scaled from those previously studied, thus facilitating a consistent comparative analysis.
- The center of gravity (CG) was assumed to coincide with the center of pressure of the fuselage (CP), neglecting fuselage moments and enabling an easier evaluation of the flight mechanics behaviour of the system.
- The maximum take-off weight (MTOW) was set to 150 kg, providing a baseline for structural and aerodynamic sizing. This was done in order to ensure that the rotor would have the same required thrust as the rotors of the previous configurations.

The blade profile used in this configuration was the NACA 0012 airfoil, a symmetrical geometry known for its predictable aerodynamic behaviour across a wide range of angles of attack. It should be noted that no twist was applied along the span of the blade. The absence of twist simplifies the analysis but may result in less efficient aerodynamic performance at the outboard sections of the blade, where the local angle of attack can differ significantly from the optimal value.

The constant chord length of the blades was set at 0.2 m. The rotor radius was specified as 1.3 m, resulting in a rotor disc area sufficient to generate the required lift for the specified MTOW. The sizing procedure was conducted in accordance with the methodology outlined in Chapter 3.

A critical parameter in the design was the tip velocity (V_{tip}), which was maintained at 120 m/s. This value was chosen to match the tip velocity used in previous configurations, allowing for direct comparisons of aerodynamic performance and noise characteristics. Maintaining a consistent tip velocity is essential when studying the effects of rotor aeroacoustics.

In conclusion, the design of this dual rotor configuration was based on a set of simplifying assumptions and carefully selected parameters with the objective of providing a simple yet effective platform for the stability assessment and the aeroacoustic evaluation.

8.2 Trim Script

In order to ensure the stability of the configuration, a numerical trim script has been developed using UPM.

This script is based on the algorithm architecture outlined in Chapter 4.

The main difference of using semi-rigid rotors instead of the rigid ones, which were previously used for the variable-pitch configurations, is the necessity of a modelling of the blades flapping motion.

It is well known that when a helicopter is flying, a variation of cyclic pitch will result in a variation of the flapping motion that is coherent with the former. Therefore, for this kind of actuation, a semi-rigid configuration is necessary, and the flapping motion must be modelled during all flight phases and for all control actuation. It is thus necessary to model both the inherent flapping and the controlled flapping.

Given that the objective of the trim procedure is to identify the control variables that will stabilize the system in a steady state regime, without accounting for the dynamic transient response, a simplified model proposed by Leishman [31] has been used and is presented in the following.

Assuming that the solution for the blade flapping motion is given by only the first harmonic function of the azimuthal angle ψ :

$$\beta(\psi) = \beta_0 + \beta_{1c}\cos(\psi) + \beta_{1s}\sin(\psi) \quad (8.1)$$

and assuming that the feathering motion can be described in the same way:

$$\theta(\psi) = \theta_0 + \theta_{1c}\cos(\psi) + \theta_{1s}\sin(\psi) \quad (8.2)$$

The flapping coefficients in the rotor hub frame are given by:

$$\beta_0 = \gamma \left[\frac{\theta_0}{8} (1 + \mu^2) + \frac{\theta_{tw}}{10} \left(1 + \frac{5}{6}\mu^2 \right) + \frac{\mu}{6}\theta_{1s} - \frac{\lambda}{6} \right], \quad (8.3)$$

$$\beta_{1s} - \theta_{1c} = \frac{(-\frac{4}{3}\mu\beta_0)}{(1 + \frac{1}{2}\mu^2)}, \quad (8.4)$$

$$\beta_{1c} + \theta_{1s} = \frac{\frac{8}{3}\mu [\theta_0 - \frac{3}{4}\lambda + \frac{3}{4}\mu\theta_{1s} + \frac{3}{4}\theta_{tw}]}{(1 - \frac{1}{2}\mu^2)}. \quad (8.5)$$

with:

- β_0 : The coning angle of the rotor blade, representing the mean flapping angle.
- β_{1s} : The lateral flapping angle represents the sine component of the first harmonic of the flapping motion.
- β_{1c} : The longitudinal flapping angle represents the cosine component of the first harmonic of the flapping motion.
- γ : The Lock number, a non-dimensional parameter that represents the ratio of aerodynamic force to inertial force in rotor dynamics.

- θ_0 : The collective pitch angle, which is the uniform pitch angle applied to all rotor blades.
- θ_{1s} : The longitudinal cyclic pitch angle, which varies sinusoidally with the rotor azimuth angle to control the flapping in the longitudinal direction. A positive value indicates a front tilt.
- θ_{1c} : The lateral cyclic pitch angle, which varies cosinusoidally with the rotor azimuth angle to control the flapping in the lateral direction. It is positive when the right tilt is observed from the front.
- θ_{tw} : The blade twist angle, representing the change in pitch angle along the blade span. In this configuration it is equal to zero as previously assumed.

It should be noted that a series of geometric transformations have been applied to map the Leishman angles convention to the UPM one, and are not reported here for simplicity. All results presented in this paragraph are shown following the aforementioned convention for the control angles in order to avoid unnecessary complexity.

In particular, for the avoidance of any doubt, a positive value of longitudinal cyclic ($\theta_{1s} > 0$) means "stick forward" and so tilting motion towards the front.

Once a flapping model has been developed, it has been incorporated into every UPM computation required by the trim procedure.

Another distinction between the current trim script and the previous one is the methodology of actuation.

In order to stabilize the system, it was necessary to modify the actuation variables (trim variables $[x_1 \ x_2 \ x_3]'$). Previously, the configurations were controlled by a collective pitch input for each rotor, now this configuration is controlled by collective and cyclic actuation for each of the two rotors.

To achieve this, a new mapping matrix has been implemented, taking into account some common control mixing from the literature.

In particular, drawing inspiration from [44], but with the assumption of a 3-Degree-of-Freedom system, the following MAPPING matrix has been implemented:

$$\text{MAPPING} = \begin{matrix} & \begin{matrix} x_1 & x_2 & x_3 \end{matrix} \\ \begin{bmatrix} 1 & 0 & 0 \\ 1 & 0 & 0 \\ 0 & 1 & 0 \\ 0 & 1 & 0 \\ 0 & 0 & -1 \end{bmatrix} & \begin{matrix} \theta_0^1 \\ \theta_0^2 \\ \theta_{1s}^1 \\ \theta_{1s}^2 \\ \Theta \end{matrix} \end{matrix} \quad (8.6)$$

In summary, the vertical channel is actuated by the two collective pitch angles simultaneously, the x-horizontal channel by the attitude pitch angle Θ , and the third DoF, the moment in the y-direction (pitch moment), by the two longitudinal cyclic angles simultaneously.

8.3 Flight Mechanics Analysis

The complete results and the simulations parameters of the UPM trim procedure are reported in Appendix D.

For the sake of clarity in the following are reported the main results for a qualitative evaluation that is useful for a model validation from a physical perspective.

It is important to note that, in contrast with the findings for the variable pitch trim, the coupling between the numerical computation and the analytical steady-state flapping computation increases the complexity of the overall procedure, resulting in a more challenging convergence of the calculations.

However, the maximum error threshold adopted for all test cases, that is in the order of 1% of the total thrust required by the system, was always matched.

In Figure 8.2 are reported the trim results for a series of simulations ranging from hover condition to TAS = 28 m/s.

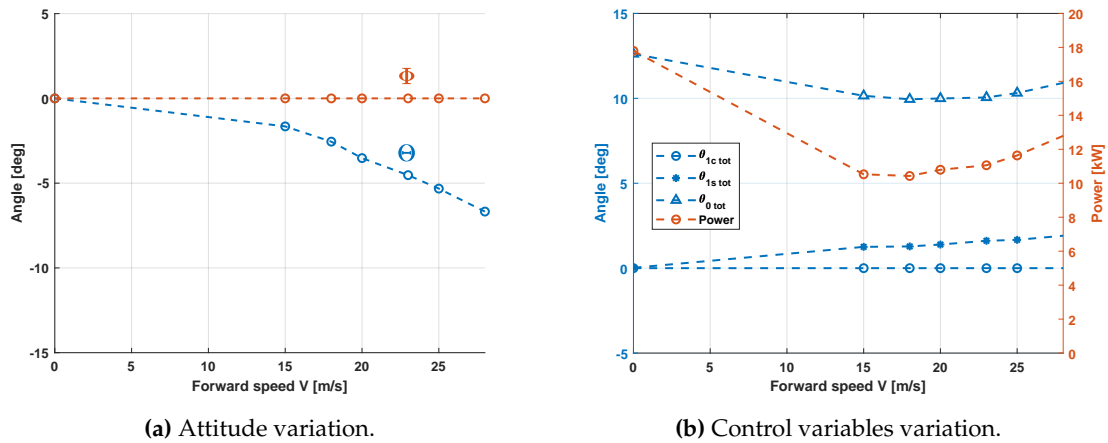


Figure 8.2: Trim results for different advancing speeds.

The lack of solutions for low speeds is attributed to the low convergence of the UPM computation due to the presence of the wake near the rotors, as previously outlined in SubCh.4.6.2. In this case, a detailed assessment of the trim procedure's robustness has not been conducted and is proposed as a potential area for further investigations.

Despite the absence of rear rotors in the present configuration, it has been determined that maintaining the aforementioned computational boundaries would provide a robust starting point. Consequently, no simulations in the region between 0 and 15 m/s have been conducted.

With regard to the attitude diagram (Fig. 8.2a), it can be observed that as the forward speed of the aircraft increases, the pitch angle also increases in magnitude. This behaviour is consistent with the underlying physics and is indicative of a trim response to an increase in the overall drag of the fuselage and rotors.

Focusing on the behaviour of the control variables in Figure 8.2b, it can be observed that the collective angles of the two rotors follow the required power of the system.

As expected, the latter exhibits a minimum point in the TAS region between 15 and 18 m/s, which is also consistent with the findings of the front rotors of the quadcopter in

SubCh.4.6.2.

It is noteworthy that for any flight condition, the rotors' collective pitch angles $\theta_{0 \text{ tot}}$ are maintained at a reasonable value, thereby validating in a certain way the preliminary sizing procedure.

With regard to the cyclic inputs, it can be observed that an increase in the longitudinal cyclic coefficient of both rotors ($\theta_{1s \text{ tot}}$) occurs in accordance with an increase in the TAS. This is also consistent with the physics of the system. Indeed, increasing the forward speed will result in the application of a pitch-up moment to the entire configuration, due to the so-called "speed stability" of the rotors. This effect is incorporated into the system through the inherent flapping contribution in Eq. 8.2, which tends to tilt the rotor backward with an increase in the advance ratio. This creates a disalignment between the rotor thrust vector and the centre of gravity, resulting in a pitch-up moment.

In order to counteract this latter contribution, the trim procedure inserts a positive longitudinal cyclic input (forward stick), which grows in proportion to the forward speed.

Mazzeo et al. in [44] also observed this behaviour, but with a notable distinction: in the DUALO configuration, where the fuselage centre of pressure (CP) is coincident with the centre of gravity (CG), the fuselage's stabilizing pitch moment influence is absent. This results in an increase in the cyclic response in proportion to the TAS, which continues without reaching a plateau.

The presented model has thus been validated, thereby allowing to start with the next stage of the research: the aeroacoustic parametric study.

8.4 Aeroacoustic Parametric Study

Once the stability of the system has been guaranteed, a parametric study has been conducted to evaluate the sound emissions of the DUALO configuration.

This study has been inspired by the research conducted by NASA [6], which evaluates the effect of phase shift on the noise emission of synchronized rigid propellers.

In this paragraph the same parametric study will be in part replicated doing some hover simulations with phase shift vectors: $\chi = [0, 0], [0, 45], [0, 90]$.

However, the primary focus of this concluding chapter is to extend this investigation to forward flight conditions for the first time, utilising the trim procedure previously outlined.

8.4.1 Hover

The results of the aforementioned hover simulations are presented below. The simulation domain is identical to that described in Ch.6 that is at an altitude of 25 meters above sea level without ground effect.

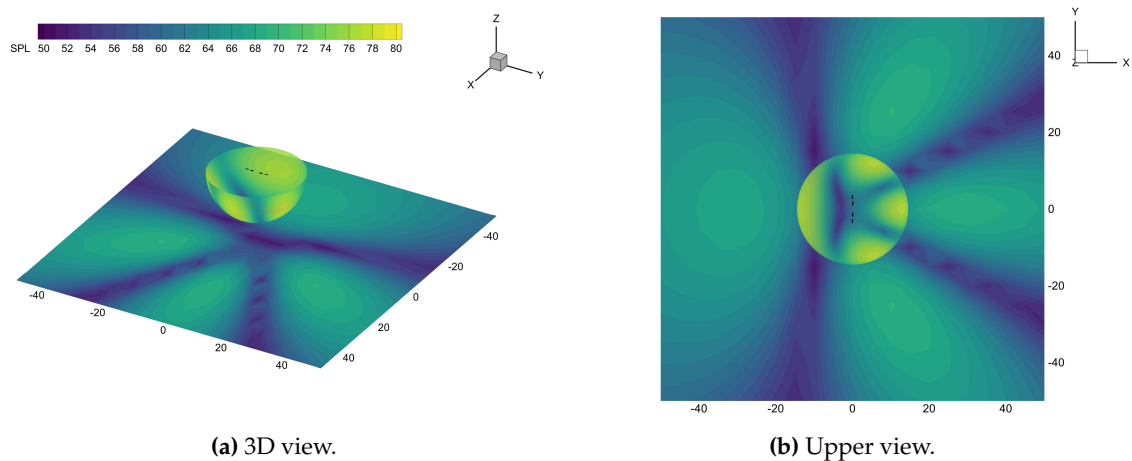


Figure 8.3: Acoustic footprint within the hemisphere and the ground, $\chi = [0, 0]$.

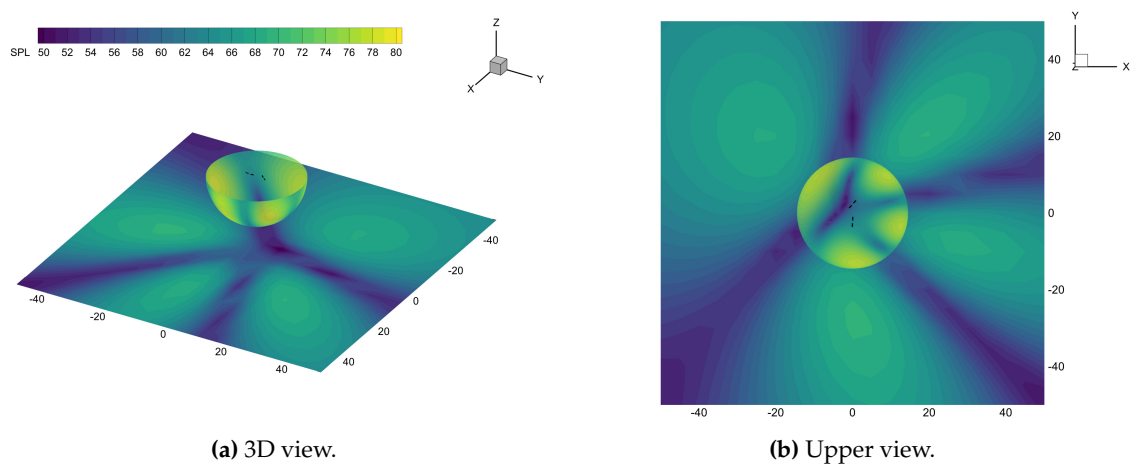


Figure 8.4: Acoustic footprint within the hemisphere and the ground, $\chi = [0, 45]$.

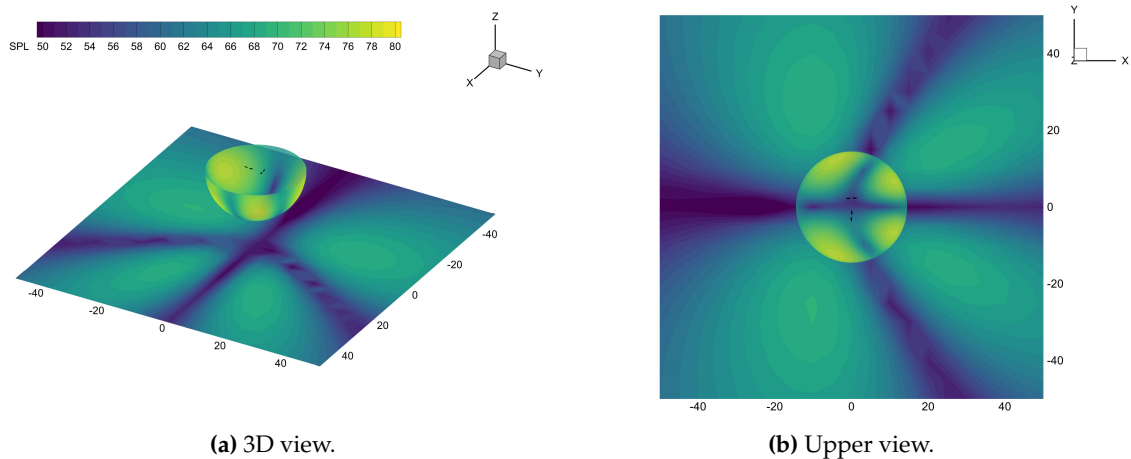


Figure 8.5: Acoustic footprint within the hemisphere and the ground, $\chi = [0,90]$.

It is notable that the noise distribution pattern observed in all test cases is identical to that documented in the NASA case study [6], with the exception of the reference system, which is specular in the latter with respect to the one used in this research. The hemisphere polar plots are not included in this chapter, but they can be found in Appendix D.

It is evident that the magnitude of the sound pressure level (SPL) differs due to the different geometry and sizing of the blades. Nevertheless, it can be confirmed that the phase synchronization effect on sound directivity is present in this configuration, demonstrating that it is not strongly dependent on the blade geometry adopted.

The most significant observation to be made from Figures 8.5, 8.3 and 8.4 is that, in the simplest configuration (consisting of only two rotors), the sound directivity seems to be simply rotated within the domain, with a variation in the phase shift between the rotors.

The most critical advantage of this configuration with respect to the preceding ones is that the noise optimization is dependent on only two parameters: one phase shift angle and the mutual distance between the rotors.

This fact permits an easier visualisation of the problem and an easier optimization process. In this case, if we hypothesise a realistic scenario in which the configuration is steady over a target, and the latter is moving, it is possible to shift the reduction zone in order to minimize the target region with only the needs of changing one parameter (χ_2).

It is also noteworthy that the minimum number of maximized/minimized regions is four, as demonstrated in this case. Furthermore, as the number of rotors increases, this number will also increase.

8.4.2 Level Forward Flight

Regarding the level forward flight analysis, the same set of phase shift vectors was employed to examine two distinct forward speeds: 18 and 28 m/s.

The findings are presented in Appendix D. For this analysis, the configuration was set at an altitude of 150 meters above the ground.

In the following, only the simulation case with $\chi = [0, 90]$ is presented for the purpose of conducting a preliminary analysis of the phenomena.

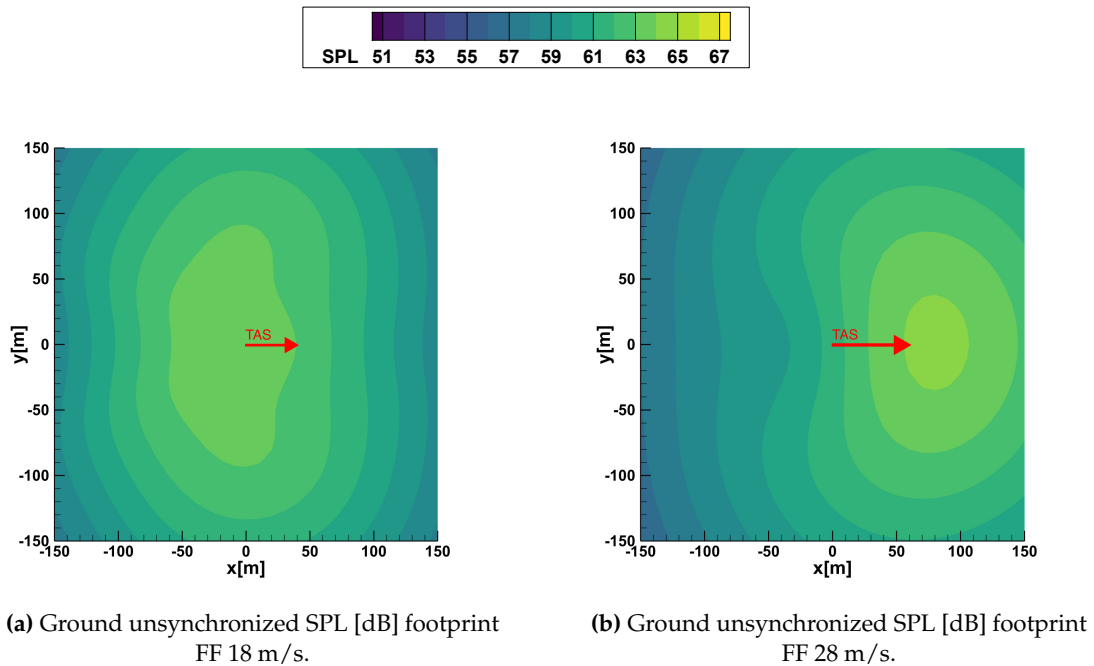


Figure 8.6: Level forward flight 150m above sea level, unsynchronized rotors.

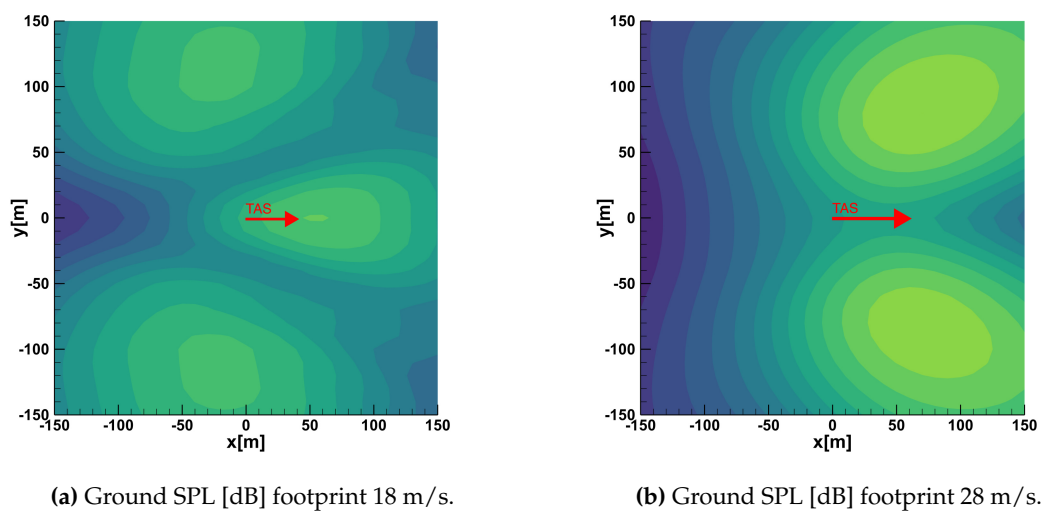


Figure 8.7: Forward flight 150m above sea level, synchronized rotors, $\chi = [0, 90]$.

As can be observed in Figures 8.6 and 8.7, the phase synchronization exerts a considerable influence on noise directionality also during forward flight.

With regard to the impact of forward velocity on the noise carpet, it can be stated that in the absence of phase synchronization, an increase in velocity results in a forward shift of the region of maximum noise, in other words, in the direction of flight.

This phenomenon is also evident in the case of synchronized rotors. As illustrated in 8.7a and 8.7b the two maximum lobes in the graph are shifted in front at higher speeds.

In terms of a more quantitative comparison, it is evident that an increase in forward velocity is correlated with an increase in the maximum value of the SPL.

The findings of this preliminary feasibility study establish a foundation for subsequent parametric investigations into phase optimization during forward flight for a dual-rotor configuration.

Chapter 9

Conclusions

This thesis addressed several key aspects of noise reduction through rotor phase synchronization. A significant achievement was the effective implementation of a trim script capable of stabilizing various parametric configurations, including multirotor systems with variable pitch propellers and double semi-rigid rotors.

Following its development, the trim script was used to conduct a performance analysis, providing valuable insights into the physical behaviour and optimization potential of the examined configurations. Furthermore, the trim script was integrated into the NOISE-Chain framework, which represents the focal point of the entire project. This integration allowed for detailed aeroacoustic evaluations and noise optimization studies, conducted collaboratively with the works of Sessini [8] and Chella [7].

The activities carried out in this research demonstrated a systematic and effective approach to address the challenges of noise reduction in VTOL systems, resulting in a significant advancement in the design methodologies of such vehicles in order to meet with the urban and regulatory requirements.

Main Results

This research demonstrated significant progress in various aspects. Numerical simulations showed that phase synchronization of rotors could achieve an SPL reduction of approximately 10 dB across all domain subregions compared to the 70 dB noise level baseline of the unsynchronized case for a hexarotor configuration. Moreover, phase optimization was shown to effectively minimize the noise in user-defined regions of interest. This capability is particularly significant as it introduces the possibility of active phase shift control during flight for dynamic noise minimization in specific target areas. Such technology holds considerable potential for military applications, where silent operations are critical for reconnaissance and surveillance missions to avoid detection. In urban contexts, the technology could be easily adapted to cover broader target zones, meeting community noise management requirements.

The trim procedure was found to be both robust and reliable for the two versions of the scripts (designed for variable pitch propellers and semi-rigid rotors). It was demonstrated that all results successfully met the convergence criteria that had been set according to Volocopter technical specifications. In addition, this study showed that synchronized rotors exhibit mutual interferences that simpler analytical trim methodologies could not capture. Nevertheless, it has been demonstrated that aircraft stability can be

maintained while keeping synchronized rotors for directional noise control. Additionally, this research represents the first implementation of such a trim methodology using UPM for multiple synchronized rotors.

With regard to the DUALO configuration, the present study obtained promising results, demonstrating the potential for conducting further, more detailed investigations using the tools developed herein. It is important to note that the application of phase synchronization to two semi-rigid rotors in forward flight was numerically tested for the first time in this research. The results confirm the effectiveness of this technology across various flight conditions.

Future Work

It is suggested that future research efforts concentrate on the development of a phase controller using the RPM channels of individual rotors. The integration of such a controller into the dynamic model presented in this thesis would allow for the evaluation of its impact on the system's dynamics during flight operations. Further enhancements to the Simulink model, such as incorporating flapping and lead-lag motions, could refine the simulation capabilities in the context of dual rotor configurations. Additionally, the implementation of an analytical inflow model could offer a deeper understanding of the dynamic effects of the front rotors' downwash on the aft ones during forward flight.

Experimental validations, such as wind tunnel tests of scaled prototypes, are also recommended to improve the reliability of the numerical results, enabling the transition of these methodologies into real-world applications.

Final Remarks

In conclusion, this research represents a significant step forward in the development of quieter VTOL systems. The study highlights the potential of phase synchronization as a key technology for achieving the acoustic, operational, and regulatory goals of next-generation VTOL vehicles, paving the way for a more sustainable Urban Air Mobility.

These achievements underscore the potential of phase synchronization technology to become an innovative element for future VTOL systems, making a significant contribution to the evolution of air mobility design solutions.

Bibliography

- [1] A. Filippone and G.N. Barakos. Rotorcraft systems for urban air mobility: A reality check. *The Aeronautical Journal*, 125(1283):3–21, 2021. doi: 10.1017/aer.2020.52.
- [2] Urban air mobility market study, 2018. Presented to NASA - Aeronautics Research Mission Directorate, <https://www.nasa.gov/>.
- [3] W. Nathan Alexander, Jeremiah Whelchel, Nanyaporn Intaratep, and Antonio Trani. Predicting community noise of suavs. In *25th AIAA/CEAS Aeroacoustics Conference*. American Institute of Aeronautics and Astronautics (AIAA), May 2019. doi: 10.2514/6.2019-2686. <https://doi.org/10.2514/6.2019-2686>.
- [4] Sakshi Tiwari. Military 'mighty impressed' by ukraine's acoustic sensor network that helps to detect, identify & hunt russian uavs. *EurAsian Times*, 2024. <https://www.eurasiantimes.com/us-military-might-impressed-by-ukraines-acousti/>.
- [5] Uzhlagas Seidaliyeva, Lyazzat Illybayeva, Kymyz Taisariyeva, Nurzhigit Smailov, and Eric T. Matson. Advances and challenges in drone detection and classification techniques: A state-of-the-art review. *Sensors*, 24(2):125, 2024. doi: 10.3390/s24020125.
- [6] Noah H. Schiller, Kyle A. Pascioni, and Nikolas S. Zawodny. Tonal noise control using rotor phase synchronization. *NASA Technical Reports*, 2019.
- [7] Aldo Chella. Analytical tool development for sound directivity simulation and control in a multicopter configuration. Master's thesis, University of Bologna, 2025.
- [8] Francesco Sessini. Numerical aeroacoustic investigation of the phase shift method for multirotor directional noise reduction. Master's thesis, University of Bologna, 2025.
- [9] D. W. Kurtz and J. E. Marte. A review of aerodynamic noise from propellers, rotors, and lift fans. Contractor Report (CR) NASA-CR-107568, JPL-TR-32-1462, Jet Propulsion Laboratory, California Institute of Technology, 1970.
- [10] J. Delfs. Lecture notes of grundlagen der aeroakustik (basics of aeroacoustics), 2023. Academic Year 2022/23.
- [11] Vitor T. Valente, Eric Greenwood, and Eric N. Johnson. An experimental evaluation of an electronic rotor phase synchronization system for multirotor aircraft noise control. In *Vertical Flight Society 80th Annual Forum & Technology Display*, Montréal, Québec, Canada, May 2024. Vertical Flight Society. doi: 10.4050/F-0080-2024-1194.

- [12] Andrew Patterson, Kasey Ackerman, Aditya Gahlawat, Naira Hovakimyan, Noah H. Schiller, and Irene Gregory. Controller design for propeller phase synchronization with aeroacoustic performance metrics. In *NASA Langley Structural Acoustic Loads and Transmission (SALT) anechoic chamber experiments.*, 2024.
- [13] Kukhwan Yu, Jeongwoo Ko, Jaeheon Jeong, and Soogab Lee. Comparative analysis of fixed-pitch and variable-pitch control systems for multirotor drones: Acoustic characteristics and rotor phase control. *Journal of Sound and Vibration*, 2023. doi: 10.1016/j.jsv.2023.118187. <https://doi.org/10.1016/j.jsv.2023.118187>.
- [14] Shujun Guan, Yang Lu, Taoyong Su, and Xice Xu. Noise attenuation of quadrotor using phase synchronization method. *Aerospace Science and Technology*, 118:107018, 2021.
- [15] Malpica Carlos and Withrow-Maser Shannah. Handling qualities analysis of blade pitch and rotor speed controlled evtol quadrotor concepts for urban air mobility. *Presented at the VFS International Powered Lift Conference 2020, San Jose, CA, January 21-23, 2020.*, jan 2020.
- [16] Michael McKay, Robert Niemiec, and Farhan Gandhi. Performance comparison of quadcopters with variable-rpm and variable-pitch rotors. In *Presented at the AHS Specialists' Conference on Aeromechanics Design for Transformative Vertical Flight, San Francisco, California, Troy, NY, USA, 2018*. Rotorcraft Adaptive and Morphing Structures Laboratory, Rensselaer Polytechnic Institute.
- [17] Robert Porter, Bijan Shirinzadeh, and Man Ho Choi. Experimental analysis of variable collective-pitch rotor systems for multirotor helicopter applications. *Journal of Intelligent and Robotic Systems*, 2016. doi: 10.1007/s10846-015-0311-2.
- [18] Shouzhao Sheng and Chenwu Sun. Control and optimization of a variable-pitch quadrotor with minimum power consumption. *Energies*, 16(4):232, 2023. doi: 10.3390/en16040232.
- [19] Mark Cutler, Nazim-Kemal Ure, Bernard Michini, and Jonathan P. How. Comparison of fixed and variable pitch actuators for agile quadrotors. In *AIAA Guidance, Navigation, and Control Conference*. American Institute of Aeronautics and Astronautics, 2011. doi: 10.2514/6.2011-6406. MIT Open Access.
- [20] Kota Shibata, Yosuke Maeda, Kohei Yamaguchi, Shun Watanabe, Shigeru Sunada, Yasutada Tanabe, Hideaki Sugawara, Hiroshi Tokutake, and Koichi Yonezawa. Vertical autorotation strategies for a quadrotor with a collective pitch control mechanism. *Technical Journal of Advanced Mobility*, 3(7):91, 2022.
- [21] W. Johnson, C. Silva, and E. Solis. Concept vehicles for vtol air taxi operations. Technical report, NTRS Research Center: Ames Research Center (ARC), 2018.
- [22] Philipp Kunze. A panel free-wake code with boundary layer method for helicopter simulations. In *45th European Rotorcraft Forum*. German Aerospace Center (DLR), sep 2019. Presented at the 45th European Rotorcraft Forum, Warsaw, Poland, 17-20 September 2019.
- [23] Jianping Yin, Thorsten Schwarz, Frederic Le Chuiton, and Matthias Schmid. *DLR Free Wake Unsteady Panel Method (UPM) User Guide*. Institute of Aerodynamics and Flow Technology (DLR), 2007. Software documentation.

- [24] Jianping Yin, Karl-Stephane Rossignol, Lukas Rottmann, and Thorsten Schwarz. Numerical studies on small rotor configurations with validation using acoustic wind tunnel data. *CEAS Aeronautical Journal*, 2023.
- [25] Jianping Yin, G. Wilke, H. Ludeke, and J. Delfs. *Prediction of Acoustic Far Field with DLR's Acoustic Code APSIM+*. Institute of Aerodynamics and Flow Technology (DLR), April 22, 2021. Software documentation.
- [26] CARA: *Computer for Advanced Research in Aerospace*. German Aerospace Center (DLR), 2024. <https://www.dlr.de/en/sp/research-transfer/research-infrastructure>.
- [27] Anna A. Kostek, Felix Lößel, Robin Wickersheim, Manuel Keßler, Ronan Boisard, Gabriel Reboul, Antonio Visingardi, Mattia Barbarino, and Anthony D. Gardner. Experimental investigation of uav rotor aeroacoustics and aerodynamics with computational cross-validation. *CEAS Aeronautical Journal*, 2023. doi: 10.1007/s13272-023-00680-z.
- [28] Kde direct propellers catalogue, 2024. Available at: <https://www.kdedirect.com/collections/multi-rotor-propeller-blades>.
- [29] Volocopter 2x, 2024. Electric VTOL News by the Vertical Flight Society <https://evtol.news/volocopter-2x/>.
- [30] Ewald Kramer Sebastian Miesner, Manuel Keßler and Ulrich Schaferlein. High-fidelity simulation of the volocopter-2x in cruise flight. In *Presented at the Vertical Flight Society's 77th Annual Forum and Technology Display*, May 2021.
- [31] J. Gordon Leishman. *Principles of Helicopter Aerodynamics*. Cambridge University Press, 2nd edition, 2006.
- [32] A. Batrakov. Helicopter fuselage drag - combined cfd and experimental studies. In *5th European Conference for Aeronautics and Space Sciences (EUCASS)*. EUCASS, 2013.
- [33] Dr.-Ing. S.F. Hoerner. *Fluid-Dynamic Drag: Theoretical, Experimental and Statistical Information*. Hoerner Fluid Dynamics, 1965.
- [34] N.C. Talbot. A mathematical model of a single main rotor helicopter for piloted simulation. *NASA Technical Memorandum 84281*, 1982.
- [35] Giulio Avanzini, Emanuele L. de Angelis, and Fabrizio Giulietti. Optimal cruise performance of a conventional helicopter. *Proceedings of the Institution of Mechanical Engineers, Part G: Journal of Aerospace Engineering*, 0(0):1–14, 2021. doi: 10.1177/09544100211024091.
- [36] Prof. Emanuele Luigi de Angelis. Unmanned system lecture notes, 2023/2024. Lecture notes for the course Master Degree in Aerospace Engineering (code 5723), Department of Industrial Engineering, Università di Bologna.
- [37] Mark G. Ballin. Validation of a real-time engineering simulation of the uh-60a helicopter. *NASA Technical Memorandum 88360*, 1987.
- [38] Mengxue Shao, Yang Lu, Xice Xu, Shujun Guan, and Jiaxin Lu. Experimental study on noise reduction of multi-rotor by phase synchronization. *Journal of Sound and Vibration*, 2022. doi: 10.1016/j.jsv.2022.117199.

- [39] Travis Krebs, Goetz Bramesfeld, and Julia Cole. Transient thrust analysis of rigid rotors in forward flight. *Aerospace*, 9(1):28, 2022. doi: 10.3390/aerospace9010028.
- [40] European Union Aviation Safety Agency. Environmental protection technical specifications applicable to vtol-capable aircraft powered by non-tilting rotors. Technical report, EASA, dec 2023. Regulation (EU) 2018/139, Article 9(2), Annex III.
- [41] Dario Brescianini, Markus Hehn, and Raffaello D’Andrea. Nonlinear quadrocopter attitude control. Technical Report ETH Zurich Technical Report, ETH Zurich, 2013. <https://doi.org/10.3929/ethz-a-009970340>.
- [42] PX4 Development Team. Px4 systems architecture, 2023. https://docs.px4.io/main/en/concept/px4_systems_architecture.html.
- [43] Emanuele L. de Angelis, Fabrizio Giulietti, Gianluca Rossetti, and Gabriele Bellani. Performance analysis and optimal sizing of electric multirotors. *Aerospace Science and Technology*, 118:107057, 2021. doi: 10.1016/j.ast.2021.107057.
- [44] Francesco Mazzeo, Marilena D. Pavel, Daniele Fattizzo, Giulia Bertolani, Emanuele L. de Angelis, and Fabrizio Giulietti. Flight dynamic modeling and stability of a small-scale side-by-side helicopter for urban air mobility. *Aerospace Science and Technology*, 148:109117, 2024. doi: 10.1016/j.ast.2024.109117.